Effects of Inorganic Additives on Properties of Polybenzimidazole Electrolyte Membranes for Medium Temperature Fuel Cells

(無機添加物が中温型燃料電池用ポリベンゾイミダゾール電解質膜の性質に及ぼす影響)

July, 2019

Doctor of Philosophy (Engineering)

KYAW ZAY YA
ジョ　ゼィ　ヤ

Toyohashi University of Technology

Effects of inorganic additives on properties of polybenzimidazole electrolyte membranes for medium temperature fuel cells

Abstract

Fuel cells are electrochemical cells that directly convert the chemical energy of a fuel (eg. hydrogen) and an oxidizing agent (eg. oxygen) into electrical energy with high efficiency and low pollutants through the redox reaction (oxidation and reduction). The working principle or the performance of fuel cells are quite different from most of the batteries, which need a continuous source of fuel and oxygen (usually from air) to prolong the chemical reaction, whereas in a battery the chemical energy usually comes from metals and their ions or oxides that are commonly already present in the battery, except in flow batteries. Fuel cells can yield electricity continuously for as long as fuel and oxygen are supplied. In the proton-exchange membrane fuel cell (PEMFC) systems, the electrolyte works as a proton conductor during fuel cell operation, which prevents the electron flowing through it from direct fuel gas mixing. In this research, the fabrication of inorganic solid composite materials was performed using mechanochemical dry milling, wet milling, and liquid-phase shaking to achieve excellent proton conductors with high proton conductivities. Especially, in the fabrication of inorganic solid acid composite materials, the effect of *N*,*N*-dimethylacetamide (DMAc) solvent was clearly seen in these composite materials fabricated using mechanochemical wet milling and liquid-phase shaking because the dispersing solvent DMAc will perform to weaken/break the precursor materials bonds by partial or complete dissolution without using high impact energy; and by extension the formation of the new bonds. In addition, with a highly mobile liquid dispersing medium it was expected that reacting species will easily locate one another and could easily attain the right orientations for effective reactions and also possibly cause a reduction in activation energies needed for effective reactions.

Inorganic solid acid composite materials were synthesized using inorganic solid acid salts $CsHSO_4$ (CHS), and heteropoly acid (HPAs). These high proton conductive composite materials were applied as inorganic additive fillers in the fabrication of inorganic-organic composite electrolytes, to improve the physicochemical and electrochemical performances of organic polymer electrolytes. Phosphoric acid-doped polybenzimidazole (PA-PBI) was selected as a polymer membrane to obtain high proton conducting state, since proton conduction mechanism and chemical interaction in this polymer matrix under anhydrous condition at medium temperatures were well understood.

In the fabrication of cesium substituted-silicotungstic acid composite materials, high proton conductive $x CsHSO_4$-$(1-x)H_4SiW_{12}O_{40}$ (CHS-WSiA) composite materials with molar ratio x = 0.5, 0.7, and 0.9 were successfully prepared via mechanochemical dry milling, wet milling, and liquid-phase shaking method. Ion-exchange reactions and strong chemical interactions occurred between precursor CHS and WSiA during the mechanochemical milling treatments and liquid-phase shaking. X-ray diffraction characterization confirmed that mechanochemical treatments and liquid-phase shaking induced an ion-exchange reaction between Cs^+ ions in CHS and H^+ ions in WSiA to produce a new class of high proton conductive composite materials. The proton conductivities of composite materials were significantly improved over their precursor materials, especially at low temperatures, below the superprotonic phase-transition temperature (141 ^oC) of CHS. Among these composite materials, the 0.9CHS-0.1WSiA (in mole ratio) composites fabricated via dry milling, wet milling, and liquid-phase shaking showed the highest conductivities of around 10^{-3} S cm^{-1} at 170 °C under dry nitrogen atmosphere. The enhanced anhydrous proton conductivities of the Cs-substituted WSiA composite materials were also corroborated with shortening of the hydrogen bonding distance in these composites for fast proton hopping transport mechanism via ^{1}H-MAS-NMR evaluation. The proton conductivities of

composite materials obtained by wet milling and liquid-phase shaking were remarkably higher than those of the composites fabricated via dry milling, especially for the composites with a lower CHS content (0.5CHS-0.5WSiA and 0.7CHS-0.3WSiA). Thus, wet milling and liquid-phase shaking methods cooperated with DMAc effectively promoted the high chemical interaction between CHS and WSiA, which increased the proton conductivities of the obtained inorganic composites. In addition, inorganic solid $CsHSO_4$-$H_3PW_{12}O_{40}$ composites (CHS-WPA) were also fabricated via mechanochemical dry milling and wet milling, and CHS-WPA doped-PBI electrolyte membranes were studied for the improvement of acid and water retention properties for the medium temperature fuel cells.

For the fabrication of mixed alkaline-substituted phosphotungstic acid composites, $MHSO_4$ (M = K, Cs) and phosphotungstic (WPA) solid acids were applied to produce anhydrous proton conductive composite materials via mechanical planetary dry ball milling. Very fast proton conducting irreversible new phase composites were obtained, with 90(50KHS-50CHS)-10WPA (mol %) mixed metal ions composite exhibiting the highest performance with conductivity from 4.9×10^{-2} to 1.4×10^{-3} S cm^{-1} at 160 to 40 °C, respectively; compared to those of the precursor materials (CHS and KHS) on the order of 10^{-3} to 10^{-8} under the same temperature regime. The XRD, FT-Raman, ^{1}H-MAS-NMR and HR-TEM results of the composites revealed the formation of an amorphous nano-interface proton-conducting pathway shell around an M-substituted WPA crystalline core, resulting in a nanoionics effect leading to the high conductivities observed; in addition to preferred sites of alkali metal ions substitution into the WPA with different stabilities and conductivities with respect to type of ion.

Inorganic-organic composite membranes were fabricated using partially cesium-substituted silicotungstic acid (CHS-WSiA) and polybenzimidazole (PBI, MRS0810H) for medium temperature polymer electrolyte fuel cells (MT-PEFCs). 0.5CHS-0.5WSiA composites fabricated via dry milling/wet milling were selected to apply inorganic composite fillers in the electrolyte membrane preparation. The flexible and homogeneous composite membranes with several phosphoric acid doping levels (PADLs) were prepared. A high maximum power density of 378 mW cm^{-2} and a good constant current stability test (200 $mAcm^{-2}$) with stable voltage of 0.61 V were obtained from a single cell test using the PBI composite membrane containing 20 wt% of CHS-WSiA from wet milling and phosphoric acid doping level (PADL) of 8 mol, at 150 ^oC under an anhydrous condition. Wet milling CHS-WSiA crystallites were highly dispersed in PBI matrix to give homogenized membranes and played a significant role in the enhancemance of acidity by increasing the number of proton sites in the electrolyte membrane. After adding CHS-WSiA into PBI membrane, the acid and water retention properties were significantly improved and incorporated as new proton conduction path by adsorbing phosphoric acid in these composite electrolyte membranes. These observations suggest that composite membranes with 8 mol of PADL are good promising PA doped-membranes with effective electrochemical properties for the medium temperature fuel cells.

In addition, metal oxide particles (TiO_2) possessing high affinity for phosphoric acid are added into the electrolyte membrane so that the PBI composite electrolyte membrane could retain phosphoric acid and water retention for a longer period measurement. The proton conductivity of the electrolyte membranes by these added particles and the influence on the fuel cell power generation characteristics in the medium temperature range were investigated. Chemically and thermally stable TiO_2 nano-powders were added to the PBI electrolyte membrane at various concentrations (2, 10, 20 wt%) to increase the retention of phosphoric acid and water. The TiO_2/PBI electrolyte membrane achieved output characteristics more than twice that of the pure PBI electrolyte membrane. It was observed that the addition of TiO_2 improved the phosphate holding power of the electrolyte membrane. TiO_2/PBI membrane retained high conductivity values at the higher temperatures as a result of its high doping level and high water retention capacity. TiO_2 (2 wt%)/PBI composite membrane showed the best performance with a power density of 434 mW cm^{-2}. These results suggest that TiO_2/PBI-based composite membranes are promising electrolytes for MT-PEFCs.

Contents

CHAPTER 1

GENERAL INTRODUCTION

Presently, environmental safety is one of most significant importance for human beings as well as the lives of future generations. One of the negative impacts of the environment is the large usage of electrical energy which increases day by day. In our daily lives, people need energy, and the primary sources of energy are provided via the combustion of fossil fuels, which leads to high levels of air pollution and the emission of greenhouse gasses [1]. To solve these challenges, new energy production technologies have to be developed for future energy production. So, fuel cells are the great promise for new energy production. The fuel cell can make direct conversion from chemical energy to electrical energy as an electrochemical cell between supplied fuels. Fuel cells for electrical power generation are a research area of high interest because they display high power conversion efficiency with low pollution levels. In the fuel cell operation, the electrolyte membrane is a principal component to progress efficiency in fuel cell routine [2]. Although fuel technology has proven to be one of the main techniques for producing new energy sources, fuel cell technology still has some problems that hinder fuel cell commercialization. Previously, many researchers devoted the development of polymer electrolyte membrane fuel cells (PEMFCs) which own gas diffusion layer, bipolar plates, microporous layer, catalyst, and membranes. Their research activities have been approached to the development of PEMFCs with the high efficiency. The commonly used PEMFC is fluorine-based polymer membranes such as Nafion® with high physical and electrochemical characteristics for low temperature PEMFC. However, Nafion® contains hazardous components such as fluorine which is detrimental to the environment. They still have numerous weaknesses, such as poor CO tolerance, high methanol diffusion, and low proton conductivity at high operation temperature. Moreover,

H_2O serves as the proton conducting carrier in Nafion® for the fuel cell evaluation. Thus, the performance of the PEFC using Nafion® would reduce at ≥100 ^oC, the boiling point of water. So, for the enhancement of the fuel cell performance and power efficiency for PEMFCs, a high operating temperature and kinematic reaction are required for high fuel cell efficiency [3-10].

One of the solutions to these shortages is the use of phosphoric acid (PA)-doped polybenzimidazole (PBI) electrolyte membrane instead of the conventional Nafion® electrolyte which needs humidification to accomplish proton conduction [11, 12]. PA plays the role of enhancing proton conductivity with a high boiling point, 158 ^oC, and thus, can be employed in generating electric power in fuel cells in the medium temperature range (100-200 ^oC). On the one hand, the operation of proton-exchange membrane fuel cells (PEM-FCs) at high-temperature and low-relative humidity provides several advantages over traditional lower temperature cells: (i) minimizing anode catalyst poising caused by CO, (ii) fuel cell flooding is almost avoided, (iii) the efficiency of fuel cell can be significantly enhanced due to the usable thermal energy produced, (iv) the amount of noble metal catalyst can potentially be reduced due to fast reaction kinetics at high-temperature, and (v) reactant gas humidification is not necessary.

Among different types of non-fluorinated ionomer (non-PFI) materials under active development, PBI is the best and commonly used. It is the engineering plastic and water insoluble polymer material. Pure PBI is not only a good electronic insulator but also an ionic insulator for PEMFC. However, high proton conductivity of PBI can be achieved in the acid-doped form of electrolyte membranes. Generating electricity in the medium temperature range under anhydrous condition has merits, such as application in co-generation systems that effectively utilizes waste heat; and for compacting device since it eradicates the need for a humidifier [13-14]. When pristine PBI membranes are doped with PA, their

mechanochemical strength reduces intensely; and the higher the acid content, the lower the mechanochemical strength, finally reducing the stability of the membrane/fuel cell.

Inorganic solid acid materials with high proton-conducting efficiencies are attracting growing high interest because of their potential applications in various electrochemical devices such as fuel cells, batteries, sensors, supercapacitors, etc [15–19]. Although many researchers have studied various solid electrolytes in the huge electrochemical research field, the development of chemically and thermally stable superprotonic conductors still remains one of the vital goals of research in solid-state electrochemistry and materials science [20–25]. Cesium hydrogen sulfate (CHS) is a superprotonic conductor with a superprotonic phase transition from a monoclinic (phase II) to a tetragonal (phase I) structure at around 141 °C. CHS is expected to be useful as inorganic additive filler in fuel cells that operate at the medium temperature range (100–200 °C). However, CHS shows low proton conductivity approximately of about 10^{-6} S cm^{-1} below its superprotonic phase transition [26–30]. It may be possible to sustain the high proton conductivity of CHS at temperatures under that of its superprotonic phase transition through the formation of CHS-based nanocomposites. Thus, composites fabricated by mixing CHS with an inorganic solid acid may display more promising proton conductivity performance at low temperature than that of CHS itself.

Heteropolyacids (HPAs) are good applicants as proton-conducting materials because of their strong acidity and catalytic properties under ambient conditions. HPAs with Keggin structure are well-known to be outstanding catalytic property based on their strong acidity. The Keggin structure is comprised of a central tetrahedron (XO_4, X = Si, Ge, P, etc) bounded by $12MO_6$ octahedral (M = W, Mo, V, etc) arranged in four groups of three-edge-sharing M_3O_{13}. HPAs are attractive as inorganic modifiers because of their high crystallinity, proton conductivity, and thermal stability. HPAs retain different hydrated structures varying from 30 to 6 molecules of water (waters of hydration) per HPA molecules depending on the

environment and temperature. The proton conductivities of these molecules decrease respectively from approximately 0.06 to 2×10^{-5} S cm^{-1}. The accurate number of waters of hydration depends on the temperature and relative humidity of the environment. HPAs have been widely used as inorganic additives in electrolyte membranes to develop fuel cell performance. However, HPAs agonize from poor chemical stability and water durability because they are hygroscopic materials. Pure HPAs are not suitable for straight usage as inorganic fillers in electrolyte membranes because they have high solubility in water and are strongly influenced by the humidity of proton conduction conditions [31–35]. To overcome these problems, alkali-substituted HPA composites contrived from alkali acids and HPAs have been developed for use in medium-temperature fuel cells. In particular, cesium-substituted HPA composites have been appealing attention because of their high catalytic activity and proton conductivity.

Anhydrous inorganic composites have been mainly fabricated for usage as inorganic solid-state superprotonic conductors with high conductivities. The inorganic solid composites synthesized using mechanochemical treatment via high-energy ball milling shows a promising way to improve the proton conductivity of acid-based composite materials [36, 37]. Thus, mechanochemical ball milling is an attractive technique to enhance the proton conductivity of solid acids and fabricate a new class of solid acid-based composites. For example, mechanochemical milling of cesium hydrogen sulfate ($CsHSO_4$, CHS) and silicotungstic acid ($H_4SiW_{12}O_{40}$, WSiA) produced new proton conductive composites that displayed proton conductivities about two to four orders of magnitude higher than that of the precursor materials under dry conditions [38–41].

In addition, metal oxides (eg. TiO_2) are added to increase the acid uptake structure and yet maintain or improve the stability of the membrane/fuel cell. Introducing metal oxide (e.g. TiO_2) into the PBI membrane can develop its PA concentration because adsorption

capability of the inorganic phase helps in retaining the acid in the membrane at high temperatures and also manages the by-product water produced. Recently, J. Lobato *et al.* reported that TiO_2 doped-PBI membranes exhibited high doping level of PA per repeat unit of PBI and also displayed a higher water uptake compared to pristine PBI, under the same condition [42]. F. Javier Pinar *et al.* also reported metal oxide doped-PBI membranes absorbed large amount of PA within a short period compared with pure PBI [43-50].

The background of this main research work focused on the production of highly proton conductive electrolytes using the mechanochemical treatments (dry and wet) and liquid-phase shaking. Exclusively, mechanochemical wet milling and liquid-phase shaking using DMAc solvent highly reinforced to attain high proton conductive composite electrolytes because DMAc solvent can partially break/weaken the precursor materials bonds to form new formation of chemical bonds. Thus, they endorse the development of structural defects, random structure, and new chemical reaction between precursor materials during fabrication of composites. These inorganic solid composites hold quite stable performance and improve the electrochemical properties as well as the chemical stabilities. Moreover, these composite fabrication methods using DMAc solvent are more effective on the fabrication of inorganic-composites with enhanced proton conductivities.

The main objective of this thesis is to apply anhydrous high proton conductive inorganic composites as additive materials into polybenzimidazole membranes for the medium temperature fuel cells. With this background theory, the topics of this thesis are summarized as follows:

1. The fabrication of inorganic composite materials using cesium hydrogen sulfate ($CsHSO_4$, CHS) and heteropoly acids (HPAs, for instance, $H_4SiW_{12}O_{40}$ (WSiA) and $H_3PW_{12}O_{40}$,(WPA)) was completed via mechanochemical dry milling, wet milling, and liquid-phase shaking. Physical and chemical properties of the composite materials were

changed with fabrication conditions, and the composites with high proton conductivities were successfully obtained.

2. For the fabrication of mixed alkaline-substituted phosphotungstic acid composite materials, $MHSO_4$ (M = K, Cs) and phosphotungstic (WPA) solid acids were consumed to produce anhydrous proton conductive composite materials via mechanochemical planetary dry ball milling.
3. The fabricated CHS-WSiA/WPA composite materials as inorganic fillers were applied in the inorganic-organic composite electrolytes to improve the electrochemical and physicochemical properties of hydrocarbon polymer electrolyte (for instance, polybenzimidazole, PBI).
4. Metal oxide (eg. TiO_2) doped PBI membranes showed highly water and acid retention properties in the dry FC operation in the medium temperature evaluation.

The first topic is to elucidate the synthesis and characterization of inorganic solid acid composite materials using CHS and WSiA/WPA via mechanochemical dry milling, wet milling, and liquid-phase shaking. The chemical/structural properties of these composites and their proton conductivities were also investigated, and new proton conduction pathway via ^{1}H-MAS-NMR results was examined based on characterization results. Especially, mechanochemical wet milling and liquid-phase shaking using DMAc solvent promoted inorganic composite materials with high proton conductivities compared with planetary ball milling without very high impact.

The second topic is the investigation of the effect of mixed alkaline metals inorganic solid acids of KHS and CHS on the anhydrous proton conductivity in the form of a composite materials with WPA; prepared by mechanochemical milling. The high proton conductive inorganic composite materials acquired will serve as good material in the anhydrous proton

conductor material application fields; with our attention in the application in organic-inorganic electrolyte fuel cell membranes for the medium temperature fuel cells.

The third topic is the utilization of fabricated CHS-WSiA and CHS-WPA composites into PBI matrix to achieve highly proton conductive composite electrolytes and improve FC performance and potential stability. These composite materials were used as inorganic additive fillers in the composite electrolyte membrane fabrication consisting of CHS-WSiA/WPA and hydrocarbon polymer (PBI). CHS-WSiA/PBI and CHS-WPA/PBI composite electrolytes were fabricated by solvent casting, and electrolyte membranes with thickness around 50-60 μm were successfully prepared.

The last topic is to prolong the FC evaluation for metal oxide doped-PBI electrolyte membrane. From this topic, metal oxide doped-PBI matrix shows high acid and water retention properties during long term durability measurement of FC. Possible chemical interaction and proton conduction mechanism were also discussed.

This doctoral thesis consists of seven chapters pointed out as following:

Chapter 1

This chapter clarifies the background, the objectives, and the contents of this thesis.

Chapter 2

This chapter describes the inorganic solid composite materials synthesized using cesium hydrogen sulfate and silicotungstic acid via mechanochemical dry milling, wet milling, and liquid-phase shaking. For the achievement of high proton conductive materials, these works have been done using DMAc solvent as dispersing medium to fabricate new composite materials with high conductivities via mechanochemical wet milling and liquid-phase shaking. These new composite materials obtained using DMAc solvent are described in section 2.1 and 2.2. Section 2.3 describes the characterization and morphological properties

of the composite materials according to their proton pathways in CHS-WSiA composite systems.

Chapter 3

In this chapter, preparation of mixed alkaline metals-doped PBI electrolyte membranes is described. This chapter is focus on the effect of mixed alkali metal ions in highly proton conductive K/Cs-hydrogen sulfate-phosphotungstic acid composite materials prepared by planetary mechanochemical milling. The outcomes showed the improved conductivities in the composite materials resulted from the formation of a superprotonic nano-interface of a complex hydrogen bonding network between MHS and WPA, induced by the substitution reaction of the metal cations into the kegging structure ion. Section 3.3 describes the characterization and morphological properties of the mixed alkaline metal-doped WPA composite materials according to their proton pathways in their composite systems.

Chapter 4

In this chapter, preparation of inorganic composite materials doped PBI electrolyte membranes is described. CHS-WSiA composite materials, as studied in chapter 2, are used as inorganic fillers into polybenzimidazole (PBI) matrix. PBI is used as a non-PFIs hydrocarbon organic polymer matrix for the composites electrolyte membranes. Section 4.2 and 4.3 describes the structural studies, physicochemical and electrochemical properties of PBI and CHS-WSiA/PBI composite membranes. Electrochemical characteristics, such as proton conductivity and fuel cell performances, of composite electrolyte membranes under hydrous conditions are discussed in details in section 4.3.

Chapter 5

In this chapter, anhydrous proton conductive inorganic-organic composite electrolyte membranes are also described. Firstly, CHS-WPA composite materials were prepared via

using mechanochemical dry and mechanochemical wet milling. Then, CHS-WPA doped PBI is synthesized by casting method, and their composite electrolytes containing CHS-WPA composites are fabricated. Section 5.3 describes the structural studies, physicochemical and electrochemical properties of PA-doped PBI and composite membranes. Likewise, anhydrous electrochemical characteristics such as proton conductivity and fuel cell performances of composite electrolyte membranes in dry atmosphere are discussed in section 5.3.6.

Chapter 6

To increase the performance enhancement and long term measurement of medium temperature fuel cell evaluation, metal oxide (TiO_2) doped-PBI based composite membrane was prepared in this chapter. TiO_2 doped-PBI membrane exhibited excellent acid and water retention properties for the medium temperature fuel cell evaluation. Firstly, structural studies of TiO_2 doped PBI membranes are described, and changes in the proton conductivity of these electrolytes are also compared with pristine PBI in section 6.3.1 and 6.3.2. Thermal stability and PA retention of TiO_2 doped PBI electrolyte is studied in section 6.3.3. Changes in the structures and electrochemical properties of TiO_2 doped PBI are also investigated in section 6.3.4.

Chapter 7

The general conclusions of this thesis are described in this chapter.

REFERENCES

[1] N. Abdullah, S.K. Kamarudin, J. Power Sources **278** (2015) 109-118.

[2] M. Mizuno, S.Hayashi, Solid State Ionics **167** (2004) 317-323.

[3] F. Mack, S. Heissler, R. Laukenmann, R. Zeis, J. Power Sources **270** (2014) 627-633.

[4] Y. Oono, A. Sounai, M. Hori, J. Power Sources **189** (2009) 943-949.

[5] J. S. Wainright, J-T. Wang, D. Weng, R. F. Savinell, M. Litt, J. Electrochem. Soc. **142** (1995) L121-L123.

[6] B. Xing, O. Savadogo, Electrochem. Commun. **2** (1999) 697-702.

[7] Y. –L. Ma, J. S. Wainright, M. H. Litt, R. F. Savinell, J. Electrochem. Soc. **151** (2004) A8-A16.

[8] L. Xiao, H. Zhang, E. Scanlon, L. S. Ramananthan, E.-W. Choe, D. Rogers, T. Apple, B.C Benicewicz, Chem. Mater. **17** (2005) 5238-5333.

[9] T. J. Schmidt, J. Baurmeister, J. Power Sources **176** (2008) 428-434.

[10] Z. Chang, H. Pu, D. Wan, L. Liu, J. Yuan, Z. Yang, Polym. Degrad. Stab. **94** (2009) 1206-1212.

[11] R. Wycisk, J. Chisholm, J. Lee, J. Lin, P. N. Pintauro, J. Power Sources **163** (2006) 9-17.

[12] S.-Y. Oh, T. Yoshida, G. Kawamura, H. Muto, A. Matsuda, Electrochim. Acta **56** (2011) 2364-2371.

[13] P. Staiti, Mater. Lett. **47** (2001) 241-246.

[14] M. Tatsumisago, T. Tezuka, A. Hayashi, K. Tadanaga, Solid State Ionics **176** (2005) 2909-2912.

[15] Y. Daiko, S. Hayashi, A. Matsuda, Chem. Mater. **22** (2010) 3418-3425.

[16] T. Okuhara, N. Mizuno, M. Misono, Appl. Catal. A **222** (2001) 63-77.

[17] H.-J. Eom, D.-W. Lee, S. Kim, S.-H. Chung, Y. G. Hur, K.-Y. Lee, Fuel **126** (2014) 263-270.

[18] S.-Y. Oh, T. Yoshida, G. Kawamura, H. Muto, M. Sakai, A. Matsuda, Mater. Sci. Eng. B **173** (2010) 260-266.

[19] D. Aili, Y. Gao, J. Han, Q. Li, Solid State Ionics **306** (2017) 13-19.

[20] S.-Y. Oh, G. Kawamura, H. Muto, A. Matsuda, Electrochim. Acta **75** (2012) 11-19.

[21] S.-Y. Oh, K. Kawai, G. Kawamura, A. Matsuda, Mater. Res. Bull. **47** (2012) 2931-2935.

[22] S. Hayashi, M. Mizuno, Solid State Ionics **171** (2004) 289-293.

[23] J. Baran, M. K. Marchewka, J. Mol. Struct. **614** (2002) 133-149.

[24] F. J. Berry, G. R. Derrick, M. Mortimer, Polyhedron **68** (2014) 17-22.

[25] S. Sampurnam, T. Dhanasekaran, A. Padmanaban, S. Muthamizh, D. Latha, G. Gnanamoorthy, S. Munusamy, V. Narayanan, Mater. Today: Proc. **5** (2018) 8808-8811.

[26] U. B. Mioč, M. R. Todorović, M. Davidović, P. Colomban, I. H. Antunović, Solid State Ionics **176** (2005) 3005-3017.

[27] L. Pesaresi, D. R. Brown, A. F. Lee, J. M. Montero, H. Williams, K. Wilson, Appl. Catal. A **360** (2009) 50-58.

[28] J. Mbah, B. Krakow, E. Stefanakos, J. Wolan, Electrochem. Solid St. **12** (2009) E12-E16.

[29] A. Matsuda, S.-Y. Oh, V. H. Nguyen, Y. Daiko, G. Kawamura, H. Muto, Electrochim. Acta **56** (2011) 9364-9369.

[30] A. Matsuda, T. Kikuchi, K. Katagiri, Y. Daiko, H. Muto, M. Sakai, Solid State Ionics **178** (2007) 723-727.

[31] A. Matsuda, V. H. Nguyen, Y. Daiko, H. Muto, M. Sakai, Solid State Ionics **181** (2010) 180-182.

[32] A. Srikanth, B. Viswanadham, V. P. Kumar, N. R. Anipindi, K. V. R. Chary, Appl. Petrochem. Res. **6** (2016) 145-153.

[33] V. V. D. Khastgir, Energy **142** (2018) 313-330.

[34] H. Wu, X. Wu, Q. Wu, W. Yan, Compos. Sci. Technol. **162** (2018) 1-6.

[35] Y.-C. Chiang, D.-S. Tsai, Y.-H. Liu, C.-W. Chiang, Mater. Chem. Phys. **216** (2018) 485-490.

[36] K. Z. Ya, P. Nbelayim, G. Kawamura, H. Muto, A. Matsuda, Solid State Ionics **337** (2019) 1-6.

[37] Y. Daiko, H. Takagi, K. Katagiri, H. Muto, M. Sakai, A. Matsuda, Solid State Ionics **179** (2008) 1174–1177.

[38] C. Xu, X. Xu, X. Wang, M. Mamlouk, K. Scott, J. Mater. Chem. **21** (2011) 6014-6019.

[39] O. Barron, H. Su, V. Linkov, B. G. Pollet, S. Pasupathi, J. Appl. Electrochem. **44** (2014) 1037-1045.

[40] Q. Li, R. He, J. O. Jensen, N. J. Bjerrum, Fuel cells **4** (2004) 147-159.

[41] J. Loboto, P. Cañizares. M.A. Rodrigo, J.J. Linares, J. A. Aguilar, J. Membr. Sci. **306** (2007) 47-55.

[42] A. Matsuda, T. Kanzaki, K. Tadanaga, M. Tatsumisago, T. Minami, Electrochim. Acta **47** (2001) 939-944.

[43] A. Matsuda, T. Kanzaki, K. Tadanaga, M. Tatsumisago, T. Minami, Solid State Ionics **139** (2001) 113-119.

[44] N. Nakamoto, A. Matsuda, K. Tadanaga, T. Minami, M. Tatsumisago, J. Power Sources **138** (2004) 51-55.

[45] K. Tadanaga, H. Yoshida, A. Matsuda, T. Minami, M. Tatsumisago, Electrochim. Acta **50** (2004) 705-708.

[46] Y. Oono, T. Fukuda, A. Sounai, M. Hori, J. Power Sources **195** (2010) 1007-1014.

[47] J. Lablo, P. Cañizares, M. A. Rodrigo, D. Úbeda, F. Javier Pinar, J. Membr. Sci. **369** (2011) 105-111.

[48] F. J. Pinar, P. Cañizares, M. A. Rodrigo, D. Ubeda and J. Lobato, RSC Adv. **2** (2012) 1547-1556.

[49] S. Yuk, D-H. Lee, S. Choi, G. Doo, D. W. Lee, H-Tak. Kim, Electrochim. Acta **270** (2018) 402-408.

[50] J. Halter, S. Thomas, S. K. Kær, T. J. Schmidt, F. N. Büchi, J. Power Sources **399** (2018) 151-156.

CHAPTER 2

INORGANIC SOLID COMPOSITES SYNTHESIZED USING CESIUM HYDROGEN SULFATE AND SILICOTUNGSTIC ACID SYNTHESIZED BY MECHANOCHEMICAL DRY MILLING, MECHANOCHEMICAL WET MILLING, AND LIQUID-PHASE SHAKING

2.1 INTRODUCTION

Inorganic solid materials with high proton-conducting efficiencies are attracting growing high interest because of their prospective applications in numerous electrochemical devices such as fuel cells, batteries, sensors, and supercapacitors, etc [1-4]. Although many researchers have already studied various solid electrolytes in the vast electrochemical research field, the development of chemically and thermally stable superprotonic conductors still remains one of the vital objectives of investigation in solid-state electrochemistry and materials science [5, 6]. They have the general formula $MHSO_4$ (MHS), where M is a monovalent cation (M = Cs, K, Na, Li, NH_4, Rb, etc). Their main property of interest is that they revealed very high proton conductivities with some showing very high proton conductivities via a phase transition to a superprotonic state at high temperatures under ambient condition. In these inorganic compounds, tetrahedral SO_4 anions generate hydrogen bond networks that support good proton conduction. It has been revealed that high proton transport in these solid acids takes place through the formation of hydrogen bonds by the reorientation of the SO_4 tetrahedron [7-9]. Among them, cesium hydrogen sulfate (CHS) is a superprotonic conductor with a superprotonic phase transition at around 141 °C. CHS is expected to be useful as one of inorganic fillers in fuel cells that operate at the medium

temperature range (100–200 °C). However, CHS shows low proton conductivity approximately of about 10^{-6} S cm^{-1} below its superprotonic phase transition [10–16]. It may be conceivable to retain the high proton conductivity of CHS at high temperatures under that of its superprotonic phase transition through the formation of CHS-based nanocomposites materials. Composite materials fabricated by co-operating CHS with an inorganic solid acid may exhibit more favorable proton conductivity behavior at low temperatures than that of CHS itself. Heteropolyacids (HPAs) are worthy candidates as proton-conducting materials because of their strong acidity and catalytic properties under ambient conditions. HPAs are attractive to the medium temperature fuel cells as inorganic modifiers which were used in these membranes' fabrication processes because of their high crystallinity, proton conductivity and thermally stability, etc. HPAs have different hydrated structure forms depending on the environment and temperature. HPAs have been extensively used as inorganic additives in electrolyte membranes to increase conductivity and fuel cell performance. Nevertheless, HPAs suffer from poor chemical stability and water durability because they are hygroscopic materials. Pristine HPAs are inconvenient for the straight usage as inorganic fillers in electrolyte membranes because they belong to high solubility in water and intensely influence the humidity of proton conduction conditions [17–25]. To overcome these problems, alkali metal-substituted HPA composite materials fabricated from alkali solid acids and HPAs have been developed for the straight use in medium-temperature fuel cells. In particular, cesium-substituted HPA (Cs-HPAs) composite materials have been fascinating attention because of their high catalytic activity and proton conductivity.

Anhydrous inorganic solid composite materials have been largely fabricated for usage as inorganic solid-state superprotonic conductors with high conductivity. The solid-state chemical reaction of these composites induced by mechanochemical milling treatment via high-energy ball milling represents a promising way to improve the proton conductivity of

acid-based composite materials [18, 19]. Hence, mechanochemical ball milling is an attractive method to increase the proton conductivity of solid acids and produce a new class of solid acid-based composite materials. For instance, mechanochemical milling of cesium hydrogen sulfate ($CsHSO_4$, CHS) and silicotungstic acid ($H_4SiW_{12}O_{40}$, WSiA) produced new composite materials that exhibited very high proton conductivity about two to four orders of magnitude higher than that of the pristine materials under dry condition [20–30]. Cesium substituted silicotungstic acid composites (CHS-WSiA) fabricated via mechanochemical milling and liquid-phase shaking have revealed very high proton conductivities with the high proton conductive regions from our recent publications [31-35].

In this work, inorganic solid composite materials with high proton conductivities were successfully fabricated from CHS and WSiA by mechanochemical dry milling, wet milling, and liquid-phase shaking. The effects of high-energy mechanochemical milling on the chemical stability, thermal stability, mechanochemical properties, and proton conductivity of inorganic solid composite materials were examined as functions of the composition and fabrication procedure. In the mechanochemical wet milling and liquid-phase shaking, *N*,*N*-dimethylacetamide (DMAc) was used as a dispersion medium between precursor CHS and WSiA materials. Opportunely, mechanochemical wet milling and liquid-phase shaking are providing not only the required strong impact to break precursor materials and form new bonds in their new products, but also DMAc dispersing solvent to weaken/break precursor materials by partial dissolution in their composites. The influence of DMAc on the properties of the inorganic solid composite materials fabricated via mechanochemical wet milling and liquid-phase shaking was determined using X-ray diffraction (XRD), Fourier transform infrared (FT-IR) spectroscopy, FT-Raman, and ^{1}H nuclear magnetic resonance (NMR) spectroscopy measurements. Our focus is on the correlations between proton conductivity and hydrogen bonding in the CHS-WSiA composite materials with the aim of identifying

proton conduction paths in these composites. Fig. 2.1 and Fig. 2.2 showed schematic illustration of mechanochemical ball milling system and mechanochemical reaction for the fabrication of composite materials.

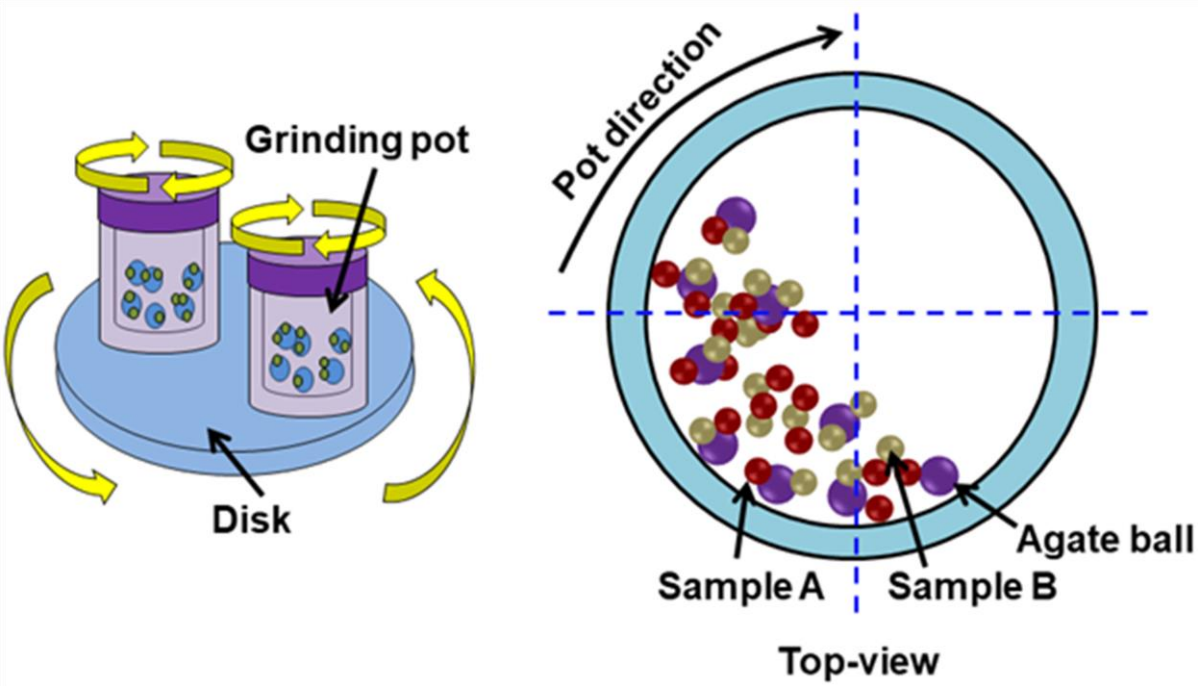

Fig. 2.1. Schematic illustration of mechanochemical ball milling system.

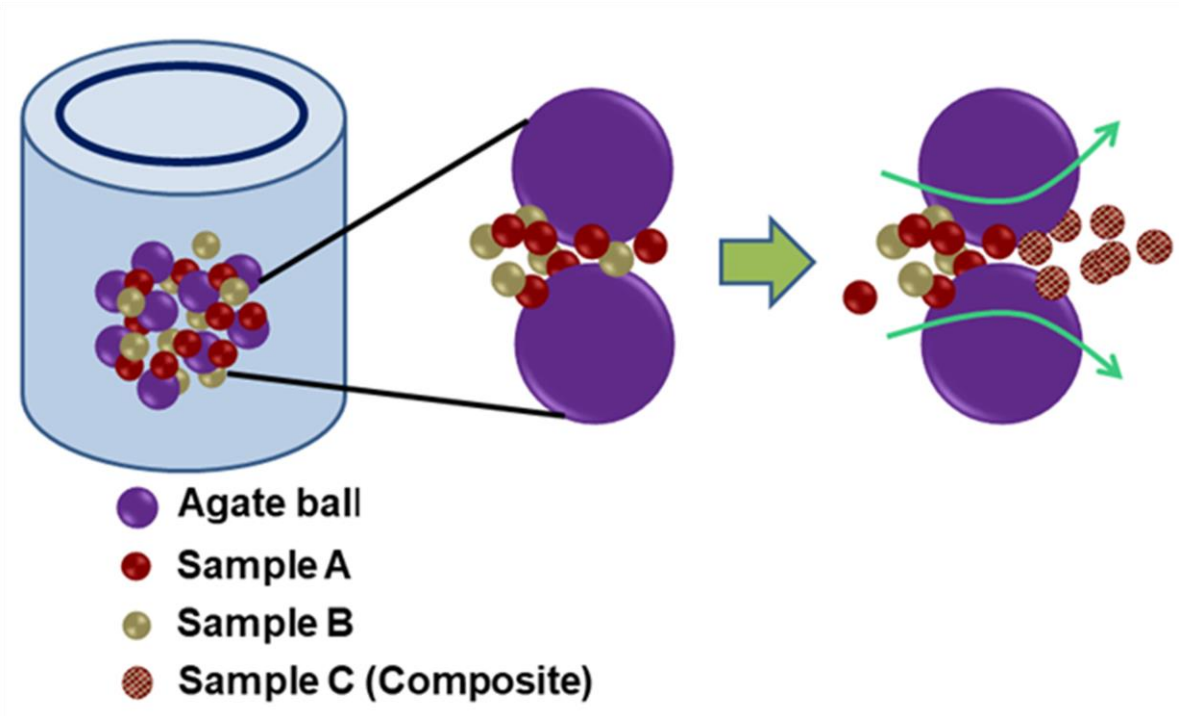

Fig. 2.2. Schematic illustration of mechanochemical reaction for the fabrication of composite materials.

2.2 EXPERIMENTAL PROCEDURE

2.2.1 Starting materials

Reagent-grade cesium hydrogen sulfate ($CsHSO_4$, CHS) and silicotungstic acid ($H_4SiW_{12}O_{40}.26H_2O$, WSiA.$26H_2O$) were purchased from Soekawa Chemical Co. Ltd., Japan and Wako Pure Chemical Industries, Japan, respectively. Especially, commercially available *N*,*N*-dimethylacetamide (DMAc, 99.0 vol%, WAKO Pure Chemical Industries, Japan) was also obtained to use as break up solvent with precursor materials for the fabrication of composites via wet milling and liquid-phase shaking. Agate material was selected for the 45 mL of milling pot and 10 mm diameter of 10 milling balls. Prior to fabrication of composites, 26-hydrate WSiA was heated at 60 °C in a vacuum oven overnight to remove physisorbed water and decrease to hexahydrate WSiA (WSiA.$6H_2O$).

2.2.2 Mechanochemical dry and wet millings of inorganic solid acid composites

Mechanochemical dry and wet milling procedures were completed as following conditions. To fabricate composite materials, appropriate quantities of CHS and hexahydrate WSiA were put in a ball-milling pot. Initially, planetary dry milling was carried out to fabricate dry composite materials in a dry nitrogen atmosphere using a planetary ball mill (Purverisette 7, Fritsch) with an agate pot (volume of 45 mL) and agate balls (ten balls of 10-mm diameter). Dry milling was conducted at a rotation speed of 720 rpm with a constant rotation ratio of 1:1 for 1 h. Then, xCHS-(1−x)WSiA composite materials with molar ratios (x) of 0.5, 0.7, and 0.9 were fabricated via mechanochemical dry ball milling. After that, composite samples were collected from the pot and heated at 80 °C in a vacuum oven overnight to get dry composite powders [36, 37]. For the wet milling composites, DMAc was used as a solvent/dispersing medium for mechanochemical wet milling treatment. Mechanochemical wet milling of appropriate amounts of CHS and hexahydrate WSiA with

DMAc (5 mL) was conducted at a rotation speed of 300 rpm with same constant rotation ratio of 1:1 for 1 h. After milling, the composite precursor was also collected from the milling pot and then dried overnight at 60 °C in an oven overnight to remove hydrated water and solvent from the composite samples. Each sample obtained by wet milling was then heated at 80 °C for 6 h in a vacuum oven overnight to obtain dry composite powders.

2.2.3 Liquid-phase shaking

For liquid-phase shaking, zirconium balls (ϕ = 4 mm, total weight = 30 g) were used as collision media in the composite solution with DMAc using a 45 mL polypropylene centrifuge tube (Labcon) and shaken at 1500 rpm with an amplitude of about 1 cm, for 1 h under ambient condition. After liquid-phase shaking, the heating and drying conditions are processed as the same conditions from the composite samples produced via mechanochemical wet milling method [34, 35].

2.2.4 X-ray diffraction analysis

Powder XRD (Ultima IV, Rigaku) patterns of the mechanochemically synthesized CHS-WSiA composite materials were measured to characterize crystalline sizes, and structural properties at room temperature (RT) using Cu K_α radiation source (tube voltage of 40 kV and current of 30 mA).

2.2.5 Thermal investigation of inorganic composite materials

Thermal properties, phase transition, and dehydration temperatures of the CHS-WSiA composite materials with precursor materials were determined by thermogravimetric analysis (TGA) and differential thermal analysis (DTA) using a Thermo Plus TG 8121 analyzer (Rigaku).

2.2.6 FTIR and FT-Raman analysis

Changes in the chemical structures of composite materials were examined by Fourier Transform Infrared (FT-IR) spectroscopy (3100 FT-IR, Varian) between 400 and 4000 cm^{-1} in transmission mode using KBr (99% grade) disks. Raman (FT-Raman; NRS-3100, Jasco) spectra were measured using a concave glass substrate, ranged between 4000 cm^{-1} and 400 cm^{-1} with a laser wavelength of 532 nm.

2.2.7 Surface observation of field emission scanning electron microscopy (FE-SEM)

The morphologies and elemental compositions of the *x*CHS-(1−*x*)WSiA composite materials were observed using field-emission scanning electron microscopy (FE-SEM; S-4800, Hitachi) and energy-dispersive spectroscopy (EDS; Emax Energy EX-250, Horiba).

2.2.8 Anhydrous proton conductivity

The anhydrous proton conductivity of the CHS-WSiA composite materials was evaluated by alternating-current impedance spectroscopy (SI 1260, Solartron) over the frequency range of 1–10^7 Hz under a dry nitrogen atmosphere. Before evaluating proton conductivity, pellet samples (diameter of 13 mm, thickness of about 1-1.3 mm) were prepared from the composite powders by pressing at a loading pressure of 60 MPa for 10 min. The measured temperature range for the composite materials was set between 170 and 50 °C; that is, measurements were conducted during cooling according to previous literature [1].

2.2.9 Solid-state ^{1}H-MAS-NMR

Chemical peak shifts and hydrogen-bonding distances of the composites and precursor materials were examined by solid-state ^{1}H magic-angle-spinning nuclear magnetic resonance (^{1}H-MAS-NMR) spectroscopy (Advance III 400, Bruker) at RT using the typical single pulse sequence. The spinning rate of the sample was fixed at 5 kHz for ^{1}H-MAS-NMR measurement and the frequency scale of the proton spectrum was determined using

tetramethylsilane (TMS) as a reference. Before ^{1}H-MAS-NMR measurement, samples were dried at 110 °C under vacuum condition for 5 h to remove hydrated water from samples, and then packed into a MAS rotor in a dry nitrogen atmosphere.

2.3 RESULTS AND DISCUSSION

2.3.1 Structural characterization of CHS-WSiA composite materials

X-ray diffraction (XRD) patterns of WSiA, CHS, and *x*CHS-(1−*x*)WSiA composite materials fabricated via mechanochemical dry milling, wet milling, and liquid-phase shaking are shown in Fig. 2.3(a), Fig. 2.3(b), and Fig. 2.4 respectively. Prior to mechanochemical dry milling, wet milling, and liquid-phase shaking, the diffraction peaks of precursor WSiA and CHS were well matched with the Joint Committee Powder Diffraction Standards (JCPDS) library files. From these XRD measurements, the main diffraction peaks of the *x*CHS-(1−*x*)WSiA composite materials with x = 0.5, 0.7, and 0.9 shifted to higher angles, which designates that some protons (H^+) of WSiA were replaced with cesium ions (Cs^+) from CHS. For the composite materials fabricated via mechanochemical dry milling, their XRD patterns displayed broad diffraction peaks, which indicate that their crystallinities were decreased after dry milling for 1 h under ambient condition. These results are comparable to those observed for mechanochemically synthesized composite materials of alkali hydrogen sulfides and HPA [4, 9, 10]. On the other hand, the diffraction peaks of *x*CHS-(1−*x*)WSiA composite materials synthesized by mechanochemical wet milling and liquid-phase shaking were more sharp, indicating that these composites were highly crystalline. This suggests that DMAc facilitated the chemical interaction between CHS and WSiA during mechanochemical wet milling and liquid-phase shaking. For the comparison of the composite materials produced via dry milling, wet milling, and liquid-phase shaking, the diffraction peaks of composites formed via wet milling and liquid-phase shaking showed large peak shifts to higher angles

with decreased interplanar spacing (*d*) compared with those of the composites fabricated by dry ball milling. This is because the composites fabricated via mechanochemical wet milling and liquid-phase shaking showed large ion-substitution and high crystallinity as a outcome of the improved chemical interaction between the precursor materials with DMAc. Some diffraction peaks of remnant pristine CHS were also detected in the XRD patterns for 0.9CHS-0.1WSiA composite materials fabricated via dry milling, wet milling, and liquid-phase shaking. This is because the *d*-spacings of the Keggin unit of WSiA decreased in these composites owing to the electrostatic compaction induced by the introduction of a large amount of Cs^+ ion into WSiA to substitute the large amount of protons (H_3O^+ and/or H^+) group cluster. Thus, structural changes of the CHS-WSiA composite materials throughout mechanochemical dry milling, wet milling, and liquid-phase shaking were clearly detected, representing that a proton-concentrated region formed in these composites through the ion-exchange reaction between CHS and WSiA. The particle size values of these composite materials are approximately 25 nm, 30 nm and 31 nm with corresponding d-spacings of approximated values 0.34192 nm, 0.34164 nm and 0.34116 nm for molar ratio of x = 0.5, x = 0.7, and x = 0.9, respectively. These results show that increasing the mole amount of CHS results in increasing particle size and reducing d-spacings. This suggests that decreased d-spacings in the WSiA Keggin structure which results reaction with more CHS units that ultimately results in the larger particle size. The decreased particle size suggests that enhanced nano-interface region for fast proton conduction. New developing hydrogen bonds between CHS and WSiA were predicted via ion-exchange reaction, which will lead to fast proton conductivity in the composite materials.

Fig. 2.5 shows the linear relationship between nominal x of the xCHS-(1−x)WSiA and Cs/(Cs+Si) determined by EDS analysis for the composites synthesized by mechanochemical dry and wet milling. With increasing the amount of CHS, Cs/(Cs+Si)

increased linearly according to the analytical results of EDS measurements. These observations are consistent with the formation of new hydrogen bonds in the composites detected in ^{1}H-MAS-NMR and FT-IR spectroscopic measurements. Overall, the composite materials with the same *x* produced via dry and wet milling possessed approximately the same compositions.

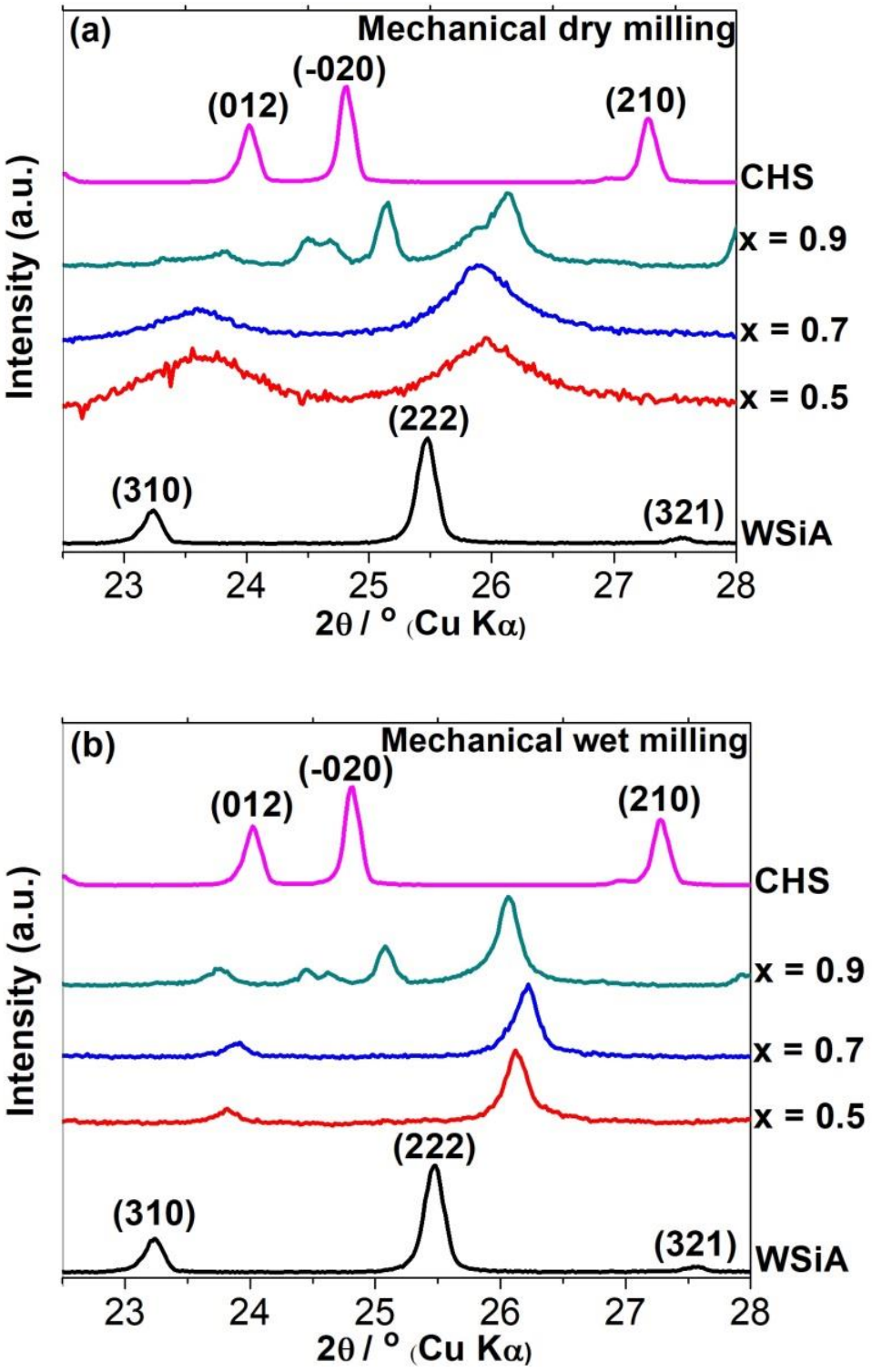

Fig. 2.3. Powder XRD diffraction patterns of WSiA, CHS, and *x*CHS-(1−*x*)WSiA composite materials with x = 0.5, 0.7, and 0.9 produced by (a) mechanochemical dry milling and (b) mechanochemical wet milling.

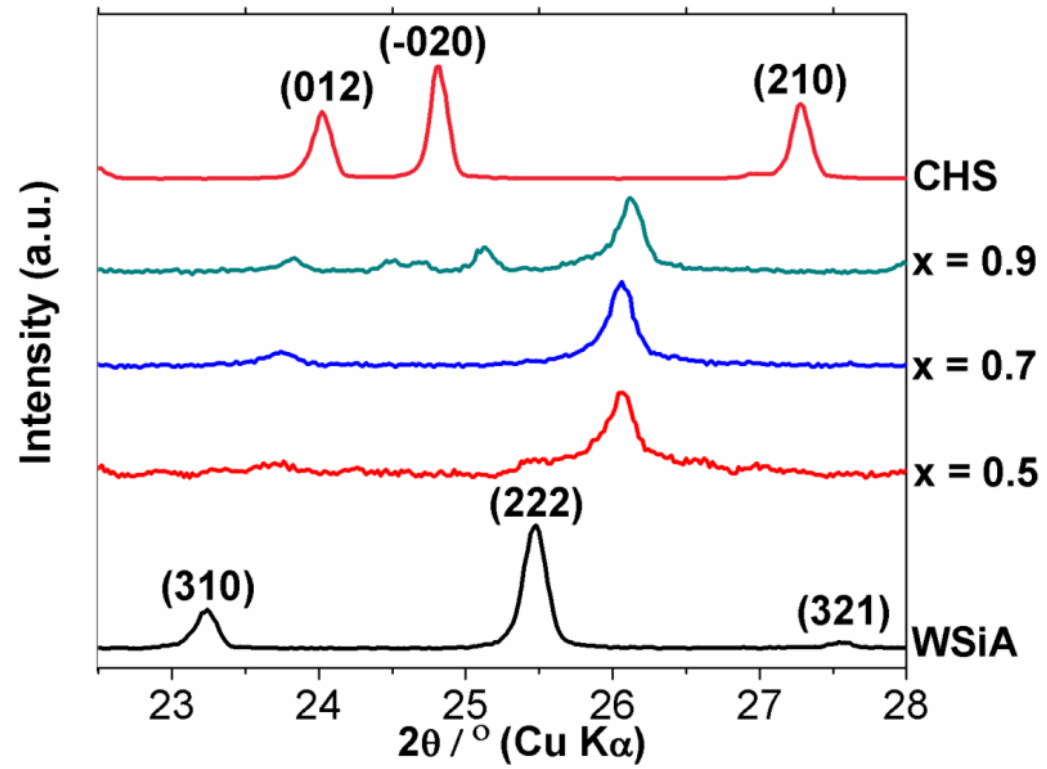

Fig. 2.4. Powder XRD diffraction patterns of WSiA, CHS and the prepared *x*CHS-(1-*x*)WSiA composite materials by liquid-phase shaking.

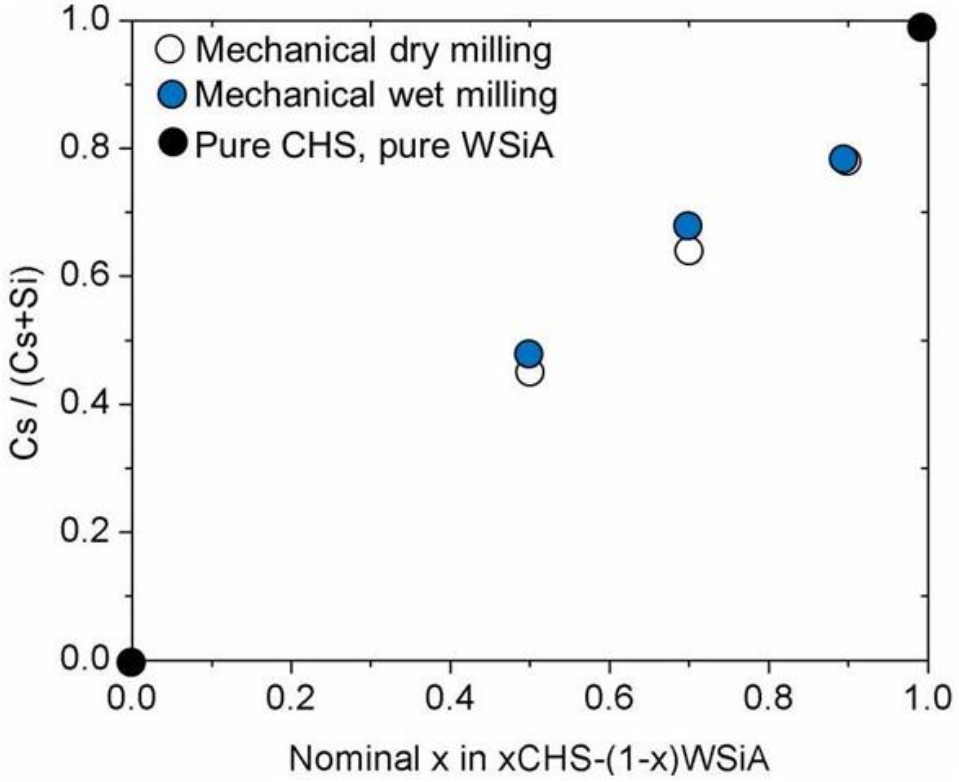

Fig. 2.5. Relationship between nominal x in xCHS-(1−x)WSiA composition and Cs/(Cs+Si) determined by EDS analysis for composite materials fabricated by mechanochemical dry and wet milling.

Thermal properties of WSiA, CHS, and *x*CHS-(1−*x*)WSiA composite materials with x = 0.5, 0.7, and 0.9 using dry milling, wet milling, liquid-phase shaking were evaluated by TGA (Fig. 2.6(a), Fig. 2.6(b), and Fig. 2.7) and DTA (Fig. 2.9(a), Fig. 2.9(b), and Fig. 2.10). The TGA curve of precursor CHS without milling indicated that it exhibited one weight loss that started at around 205 °C, which was ascribed to the dehydration and thermal decomposition of sulfate in CHS. The weight loss of precursor WSiA started at around 160 °C and was attributed to the loss of water of crystallization. The *x*CHS-(1−*x*)WSiA composite materials via dry milling initiated to lose weight at around 100 °C, which was attributed to dehydration of these composites (see Fig. 2.6(a)). The weight loss of the 0.9CHS-0.1WSiA composite fabricated via dry milling started around 160 °C, which was attributed to dehydration of composite. Another weight loss was detected at around 205 °C, which corresponded to decomposition of the sulfate groups of remnant CHS in this composite after the evaporation of physisorbed water. Such a weight loss originating from the thermal decomposition of sulfate groups of CHS was not observed for the 0.5CHS-0.5WSiA and 0.7CHS-0.3WSiA composites fabricated via dry milling. For the composite materials produced via wet milling and liquid-phase shaking, the first weight loss started at around 100 °C, which was also attributed to dehydration of physisorbed water. These composites also presented weight loss trends that started at around 205 °C, as shown in Fig. 2.6(b) and Fig. 2.7, which were ascribed to thermal decomposition of sulfate groups of CHS. This thermal decomposition behavior was analogous to that of CHS itself. The weight loss percentages of *x*CHS-(1−*x*)WSiA composite materials fabricated via mechanochemical wet milling and liquid-phase shaking were greater than those of the composites produced via dry milling because physisorbed water and DMAc solvent were detached from the composites formed via the wet condition during annealing [33]. However, we believe that all these weight losses within the measured temperature range involved the loss of remnant DMAc

solvent as Raman analysis of the composites and volatile DMAc solvent shows the presence of DMAc even after drying under vacuum at 80 ^{o}C for 3 h (Fig. 2.8).

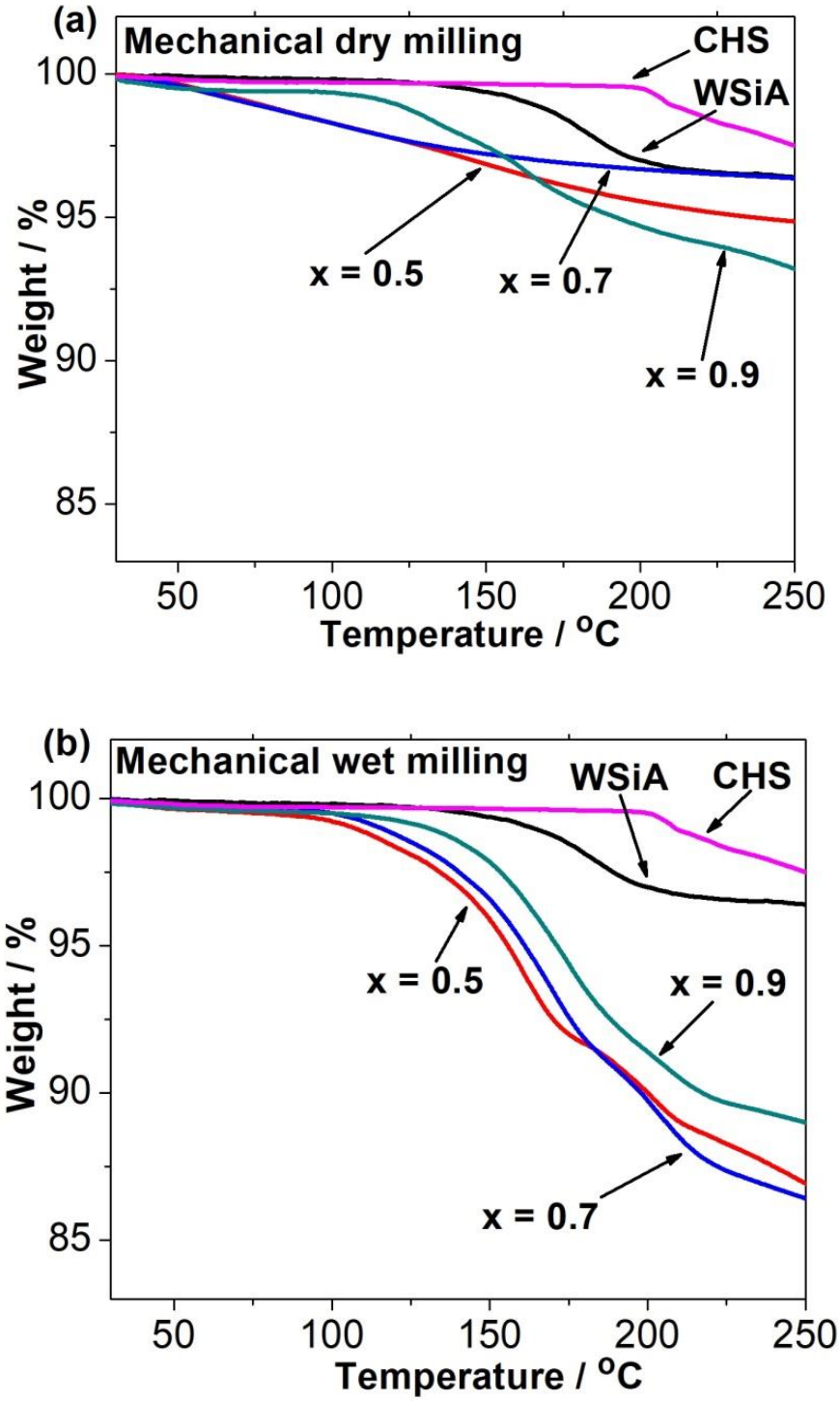

Fig. 2.6. TGA curves of WSiA, CHS, and *x*CHS-(1−*x*)WSiA composite materials with x = 0.5, 0.7, and 0.9 produced by mechanochemical (a) dry milling and (b) wet milling.

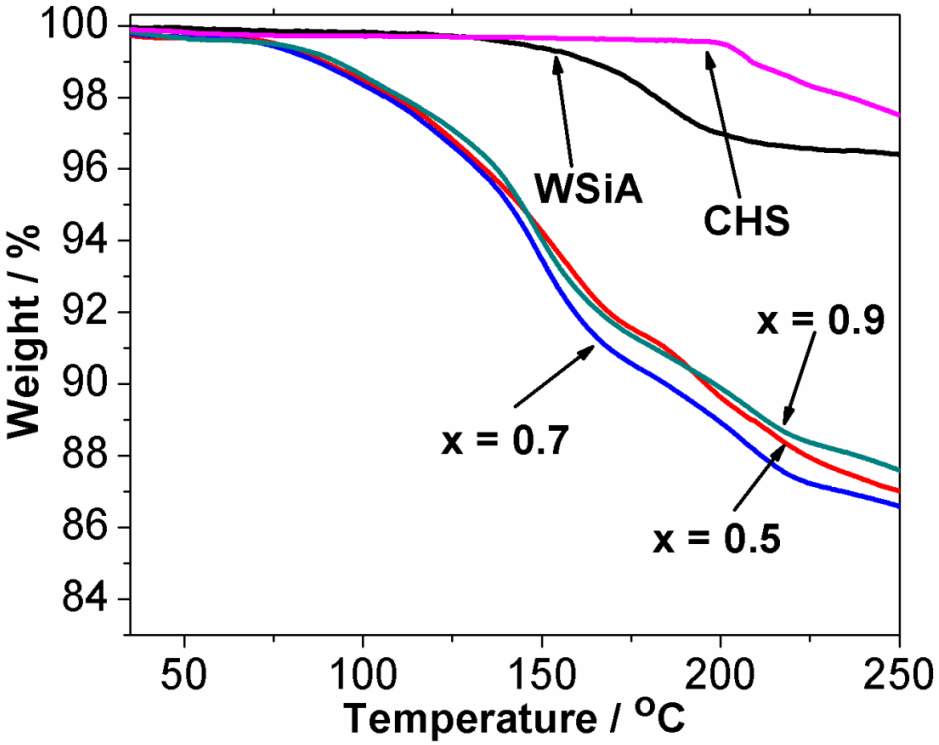

Fig. 2.7. TGA curves of the starting materials (WSiA and CHS) and prepared (*x*CHS-(1-*x*)WSiA) composite materials.

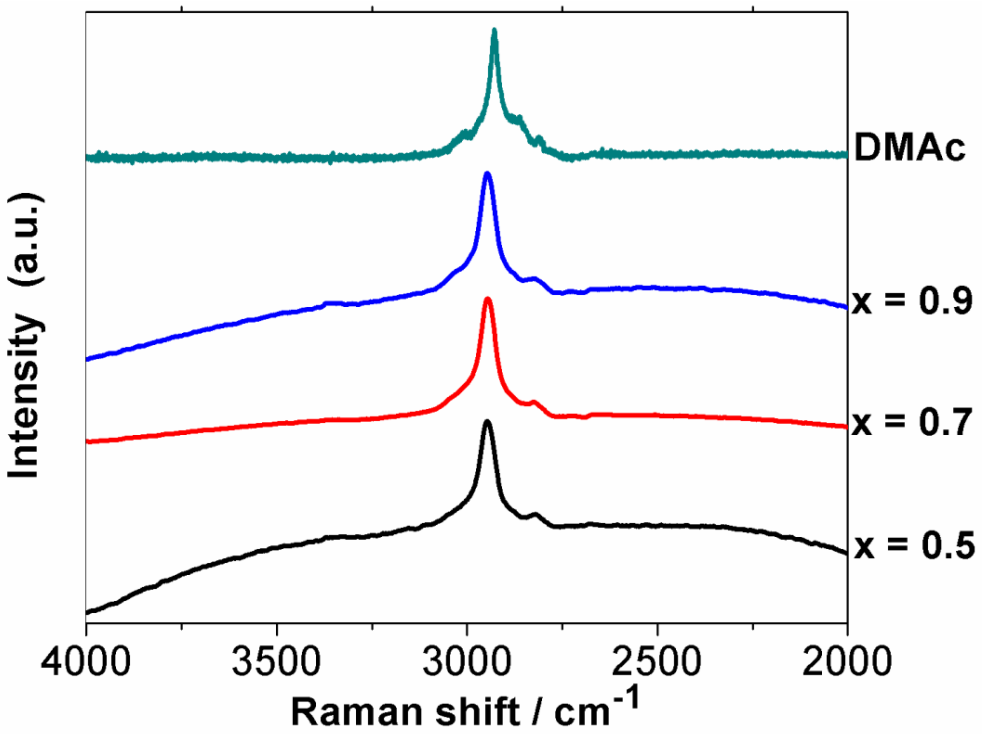

Fig. 2.8. FT-Raman spectra of DMAc solvent and the composite materials fabricated via liquid-phase shaking dried at 80 ^{o}C under vacuum showing remnant DMAc.

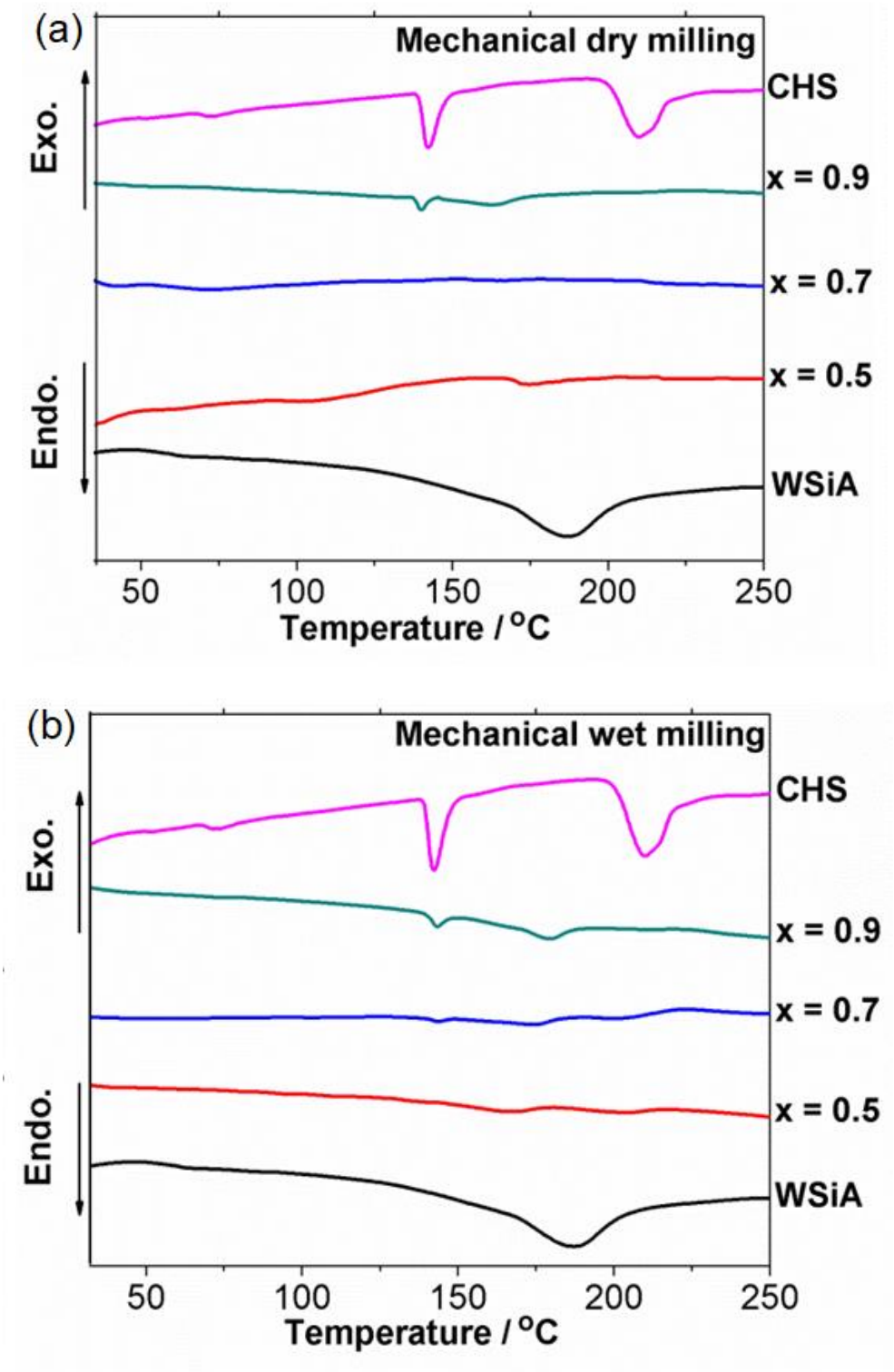

Fig. 2.9. DTA curves of WSiA, CHS, and *x*CHS-(1−*x*)WSiA composite materials with x = 0.5, 0.7, and 0.9 produced by mechanochemical (a) dry and (b) wet milling.

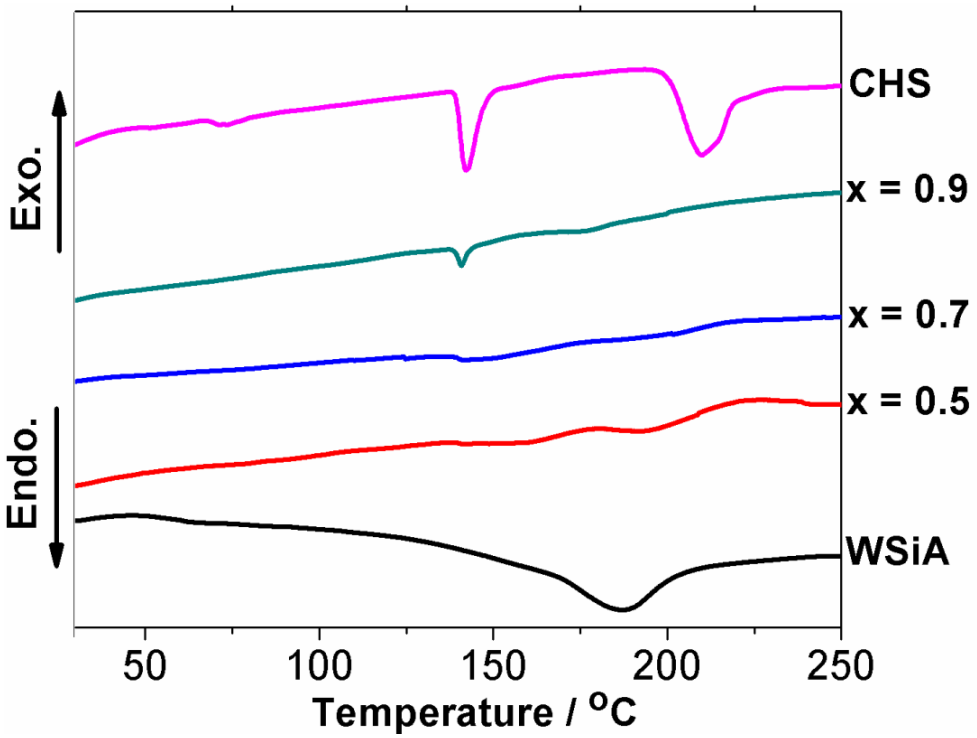

Fig. 2.10. DTA curves of the precursor materials (WSiA and CHS) and prepared (*x*CHS-(1-*x*)WSiA) composite materials via liquid-phase shaking.

DTA curves for precursor CHS without milling (Fig. 2.9(a), Fig. 2.9(b), and Fig. 2.10) contained distinctive endothermic peaks at around 141 and 205 °C, which were ascribed to its phase transition from a solid phase II to a liquid-like phase I, and thermal decomposition, respectively. According to these observations, CHS, which is the mono-cesium salt of sulfuric acid, shows a superprotonic phase transition from monoclinic to tetragonal at around 141 °C. The thermal decomposition of sulfate in CHS was observed at around 205 °C. A large endothermic peak was detected for WSiA at around 160 °C, which was attributed to dehydration of $WSiA.6H_2O$. For the 0.5CHS-0.5WSiA and 0.7CHS-0.3WSiA composite materials synthesized by dry milling, wet milling, and liquid-phase shaking, no appreciable peaks were observed in their DTA curves. In contrast, the 0.9CHS-0.1WSiA composite materials fabricated by dry milling, wet milling, and liquid-phase shaking displayed small peaks at around 141 °C, which were ascribed to a phase transition of remnant (unreacted part) CHS in their composites after fabrication processes. A phase transition ensued in these composites because of the large amount of CHS introduced into WSiA. These findings indicate that the phase transition of CHS from a solid phase II to a liquid-like phase I is preserved in the xCHS-(1−x)WSiA composite materials (x = 0.5, 0.7, and 0.9) despite the introduction of WSiA. CHS in these composites also acts as a fast proton transfer medium to enhance proton conductivity. Thus, these observations in the precursor samples and composite materials designate a permanent phase transition of CHS from monoclinic to tetragonal in the composite samples, induced by the substitution of Cs^+ ions from CHS into WSiA, suppressing its reversibility back to the monoclinic phase at low temperatures.

Differences in the chemical bonds and interactions of the composite materials produced by dry milling, wet milling, and liquid-phase shaking were investigated by FT-IR spectroscopy (Fig. 2.11(a), Fig. 2.11(b), and Fig. 2.12). The FT-IR spectra of the precursor materials and CHS-WSiA composite materials indicated the expected peaks in the 700–1300

cm^{-1} region. The FT-IR spectrum of CHS displayed bands at 850, 1020, 1180, and 1235 cm^{-1} that were accredited to vibrations of OH in HSO_4, SO_3, OH, and SO_4, respectively [1]. The characteristic bands of the WSiA Keggin anions at 980, 925, 880, and 800 cm^{-1} were attributed to the typical asymmetric stretching vibrations of W=O, Si-O, W-O_c-W (corner-sharing oxygen atoms), and W-O_e-W (edge-sharing oxygen atoms), respectively [1, 23, 28].

For the composite materials synthesized via mechanochemical dry milling under anhydrous condition, ion substitution by Cs^+ from CHS for H^+ of WSiA did not obviously change the FT-IR bands originating from W=O and Si-O in WSiA. The OH stretching vibration of CHS appeared at a low frequency of around 1180 cm^{-1} for the 0.9CHS-0.1WSiA composite because of the introduction of a large amount of CHS into WSiA via large ion-substitution reaction. It was also supposed that chemical reactions between CHS and WSiA were supported in DMAc, which produced a new proton conduction path in these composites to increase proton conductivity. On the one hand, for the composite materials produced via mechanochemical wet milling and liquid-phase shaking, ion exchange of Cs^+ from CHS for H^+ of WSiA caused the W=O and Si-O bands from WSiA to shift slightly to lower frequency compared with the case for pure WSiA. The OH signal of CHS shifted to higher frequency (around 1180 cm^{-1}) in these composites, representing that the OH bonding distance of CHS was shortened and much stronger. The band shifts observed for these composites were attributed to the electrostatic compaction induced by introducing Cs^+ into WSiA [1, 28]. Thus, these findings of the shifted bonds resulting from shorter new OH bonds corroborates the new formation of composite materials with a recommended interface between the two components to serve as a H^+ conduction path.

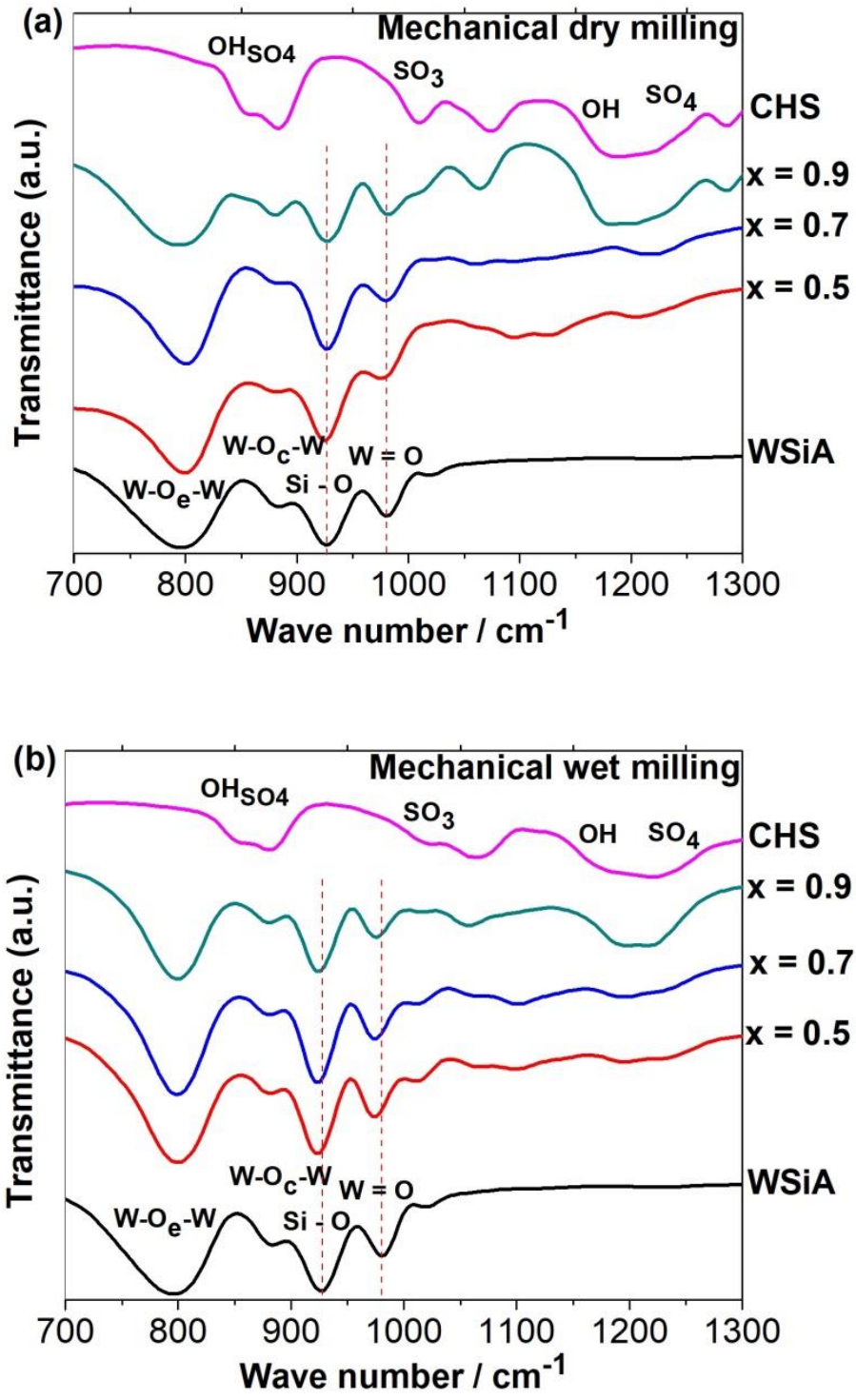

Fig. 2.11. FT-IR spectra of WSiA, CHS, and *x*CHS-(1−*x*)WSiA composite materials with x = 0.5, 0.7, and 0.9 produced by mechanochemical (a) dry milling and (b) wet milling.

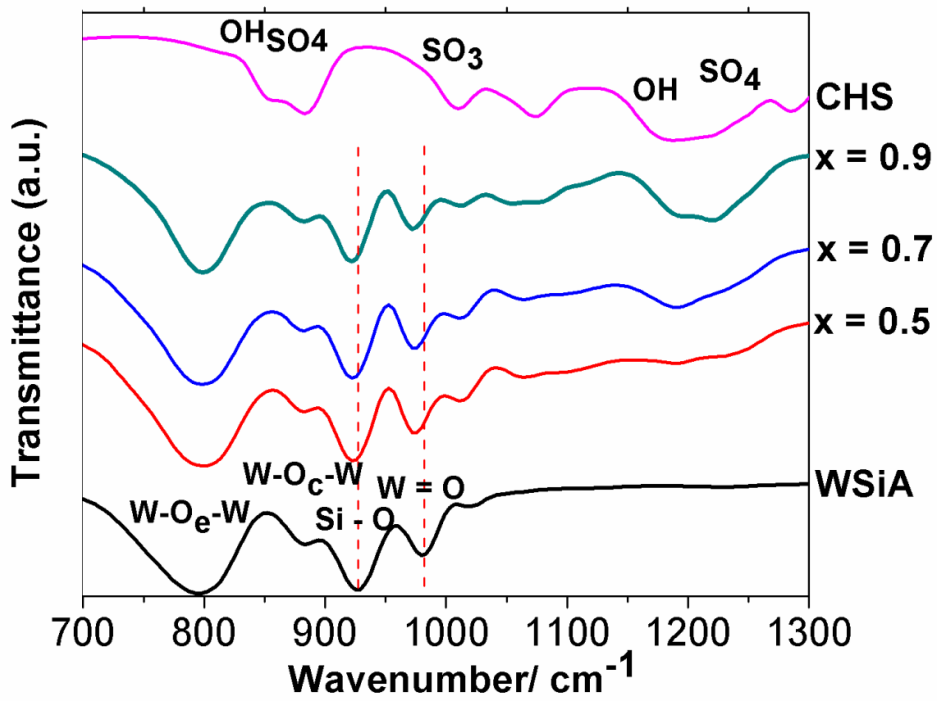

Fig. 2.12. FT-IR spectra of the starting materials (WSiA and CHS) and prepared (*x*CHS-(1-*x*)WSiA) composite materials via liquid-phase shaking.

From Fig. (2.13(a), 2.13(b), and 2.14), the FT-Raman bands for the asymmetric and symmetric stretching modes of W=O are clearly detected at around 998, and 974 cm^{-1} respectively, for the WSiA. The main intend bands at 996 cm^{-1} and 857 cm^{-1} in the spectrum for CHS are attributed to the chain S-O bond in SO_4^{2-} and the SOH of CHS, respectively. After dry milling, intend bands of CHS-WSiA composite materials were formed at around 998 cm^{-1}, which are accredited to precursor WSiA. For mechanochemical wet milling and liquid-phase shaking, the W=O bonds of WSiA slightly shifted to low frequency comparing with CHS-WSiA (dry milling) composite and precursor WSiA. The development of new bonds in these composites via wet milling and liquid-phase shaking was estimated in the FT-IR results in Fig. 2.13(b) and Fig. 2.14. The changes of W=O bonds probably occurred due to a newly developed hydrogen bond between the outermost of partially Cs-substituted WSiA and HSO_4^-, thus, shifted W=O bonds slightly lengthen by the attraction of HSO_4^-. Thus, these new observations indicated that the mechanochemical wet milling and liquid-phase shaking produced new chemical interaction between CHS and WSiA to form the CHS-WSiA composites with anhydrous high proton conductivities. It was also expected that the ion-exchange reaction between H^+ ions in WSiA and Cs^+ ions in CHS will enhance high proton conductivities.

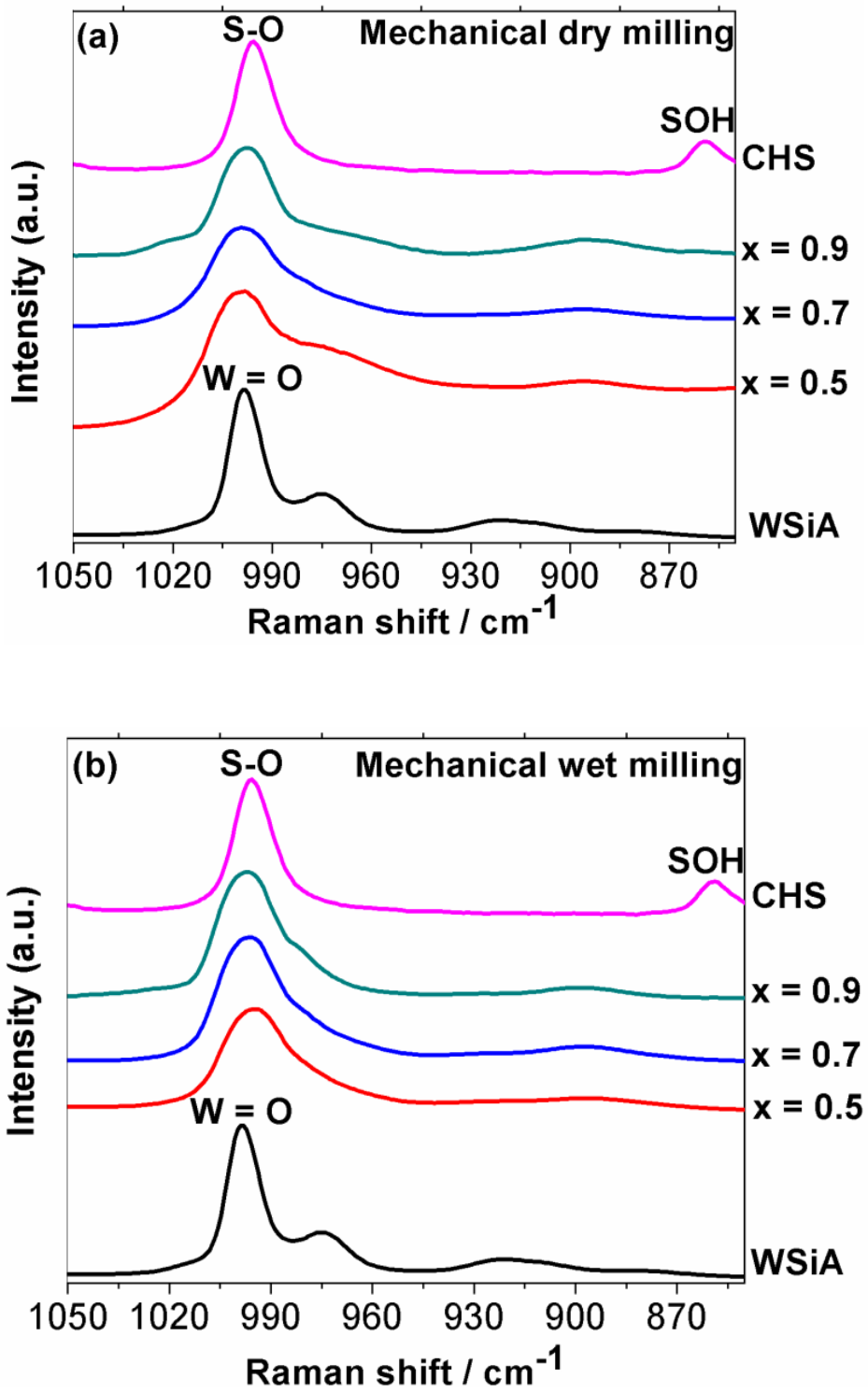

Fig. 2.13. FT-Raman spectra of WSiA, CHS, and *x*CHS-(1−*x*)WSiA composite materials with x = 0.5, 0.7, and 0.9 produced by mechanochemical (a) dry milling and (b) wet milling.

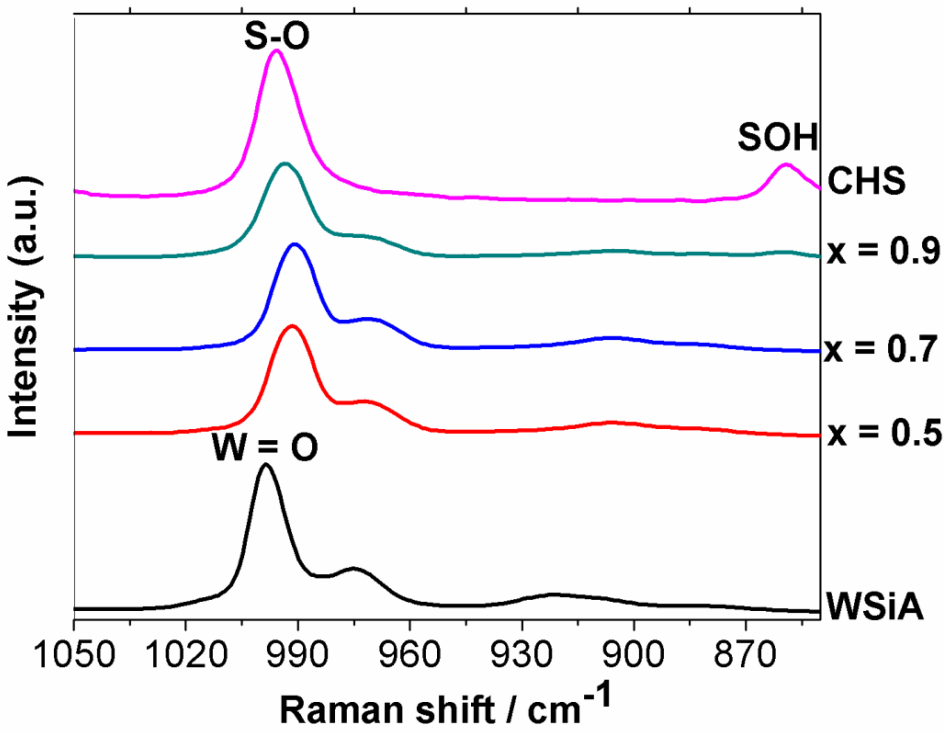

Fig. 2.14. FT-Raman spectra of the starting materials (WSiA and CHS) and prepared (*x*CHS-(1-*x*)WSiA) composite materials via liquid-phase shaking.

2.3.2 FESEM analysis of CHS-WSiA composite materials

FE-SEM images of *x*CHS-(1−*x*)WSiA composite materials synthesized by dry milling, wet milling and liquid-phase shaking are presented (Fig. 2.15 (a-c), Fig. 2.15 (d-f), and Fig. 2.16(a-c)) respectively. The FE-SEM images revealed that the *x*CHS-(1−*x*)WSiA composite materials showed fine composite powders with homogeneous surface structures. Increasing the content of CHS caused the grain size to decrease and become more homogeneous for composite materials produced via dry milling, wet milling, and liquid-phase shaking. The wet milling and liquid-phase shaking methods provided composite materials that were denser and had a much smaller grain size with less agglomeration than those of the composites fabricated via dry milling. These findings implied that the introduction of a large amount of CHS increased ion substitution in these composites during dry milling, wet ball milling, and liquid-phase shaking. In particular, the composite materials synthesized via wet milling and liquid-phase shaking was more uniform than those fabricated via dry milling because DMAc as the solvent/dispersing agent promoted ion-substitution between the precursor materials. Thus, DMAc was an effective collision medium in wet milling and liquid-phase shaking, helping to strengthen chemical interactions between CHS and WSiA and supporting the formation of composites with new proton conduction paths.

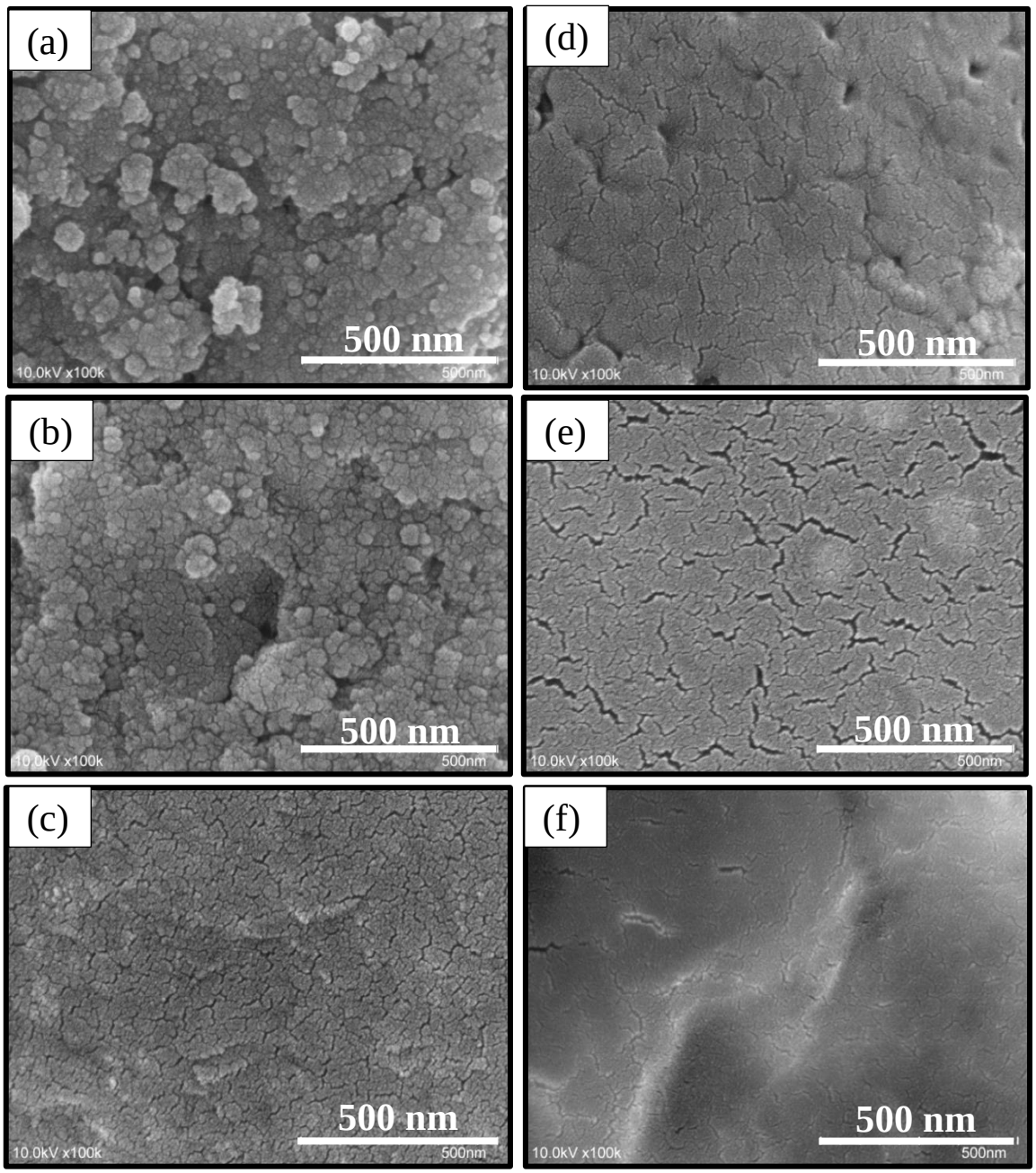

Fig. 2.15. FESEM images of *x*CHS-(1−*x*)WSiA composite materials (*x* = 0.5, 0.7,0.9) by (a-c) dry ball milling, and (d-f) wet ball milling.

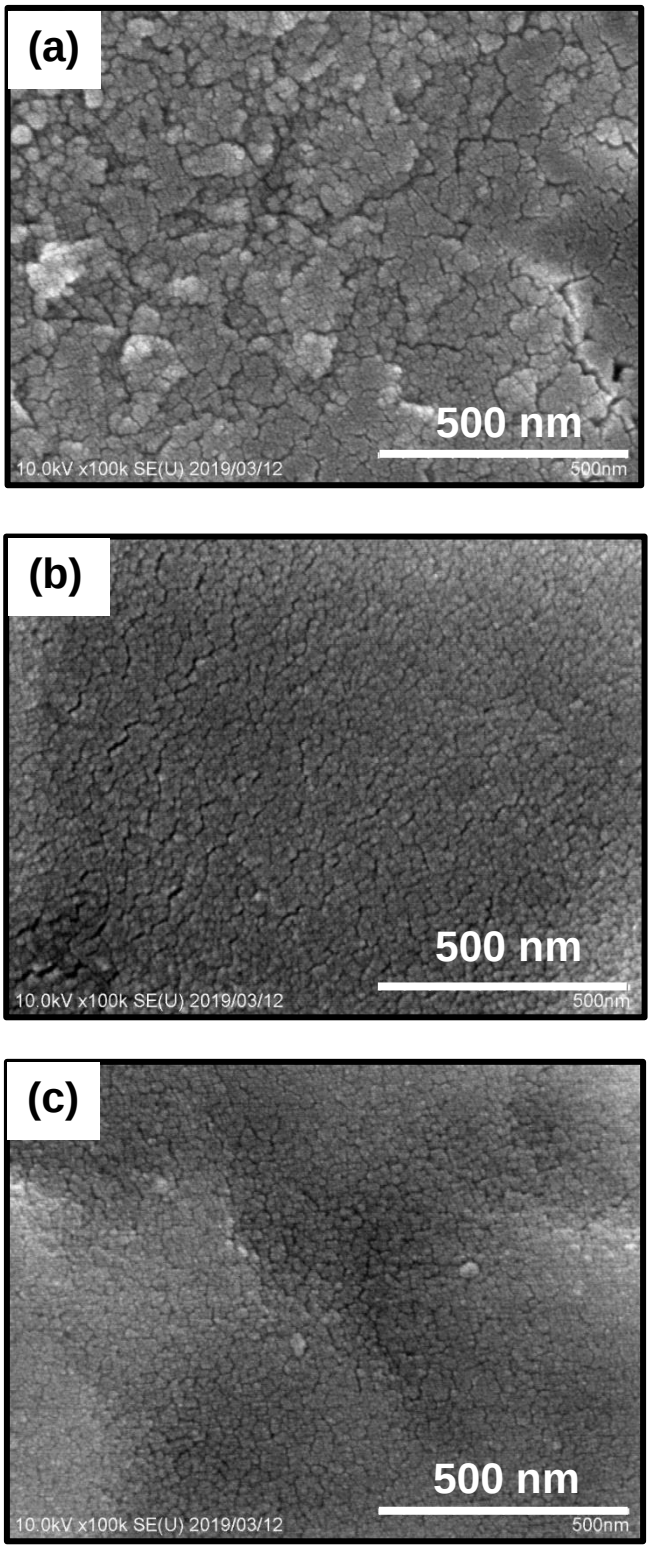

Fig. 2.16. FE-SEM images of *x*CHS-(1-*x*)WSiA composite materials with (a) $x = 0.5$, (b) $x = 0.7$, and (c) $x = 0.9$ via liquid-phase shaking.

2.3.3 Proton conductivity of CHS-WSiA composite materials

The mechanochemically synthesized CHS-WSiA composite materials exhibited high anhydrous proton conductivities over a wide temperature range, especially under the phase transition temperature of CHS, as presented in Fig. 2.17(a), Fig. 2.17(b), and Fig. 2.18. The proton conductivities of the *x*CHS-(1−*x*)WSiA composite materials fabricated by mechanochemical dry milling, wet milling, and liquid-phase shaking were evaluated during cooling in the large temperature range from 170 to 50 °C. Pristine CHS showed a superprotonic phase transition from monoclinic (5.53×10^{-9} S cm^{-1}) to tetragonal with high conductivity (8.04×10^{-4} S cm^{-1}) around 141 °C even under a dry Nitrogen (N_2) atmosphere. Under the superprotonic condition, the proton conductivity of CHS jumps abruptly to a high conductivity state [3,25]. WSiA showed high proton conductivities of 9.54×10^{-7} to 1.74×10^{-8} S cm^{-1}. The 0.5CHS-0.5WSiA, 0.7CHS-0.3WSiA, and 0.9CHS-0.1WSiA composite materials produced via dry milling showed proton conductivities higher than those of precursor CHS and WSiA, particularly under the superprotonic phase transition temperature (141 °C). These observations showed that the xCHS-(1-x)WSiA composite materials had effective substitution of Cs^+ from CHS for H^+ in WSiA. The 0.9CHS-0.1WSiA composite produced via dry milling showed highest proton conductivities of 3.26×10^{-4} to 6.75×10^{-4} S cm^{-1} for the dry milling composite materials. These findings indicated that some CHS and H_2SO_4 remained as remnants in the 0.9CHS-0.1WSiA composite after mechanochemical dry milling. These remnant components were highly acidic and facilitated proton conduction, thus markedly enhancing proton conductivity. The proton conductivities of the composite materials increased with the content of CHS [33].

On the other hand, the *x*CHS-(1−*x*)WSiA composite materials with x = 0.5, 0.7, and 0.9 synthesized via mechanochemical wet milling showed very high proton conductivities of 8.99×10^{-6} to 1.21×10^{-3}, 1.20×10^{-4} to 1.23×10^{-3}, and 1.31×10^{-4} to 1.05×10^{-3} S cm^{-1},

respectively. The proton conductivities measured ranged from 5.78×10^{-6} to 5.37×10^{-4} S cm^{-1}, from 5.08×10^{-5} to 7.66×10^{-4} S cm^{-1}, and from 1.38×10^{-4} to 2.42×10^{-3} S cm^{-1} for *x*CHS-(1-*x*)WSiA with x = 0.5, 0.7, and 0.9 via liquid-phase shaking. The proton conductivities of *x*CHS-(1−*x*)WSiA composite materials produced via mechanochemical wet milling and liquid-phase shaking were higher than those of the composites fabricated by mechanochemical dry milling, especially for the 0.5CHS-0.5WSiA and 0.7CHS-0.3WSiA composites with lower CHS contents. The 0.9CHS-0.1WSiA composite materials produced via dry milling, wet milling, and liquid-phase shaking contained remnant CHS and H_2SO_4, which behaved as proton-conducting media and enhanced the proton conductivity of these composites. These observations specified that the proton-conducting mechanisms of the composites are quite dissimilar from those of the precursor materials. Thus, the composite materials showed high performance with the proton conductivity of 0.9CHS-0.1WSiA showing the highest conductivity. But, for the purpose of inorganic additive fillers in the polymer electrolyte membrane fuel cells, the low concentration of CHS (for instance, x = 0.5) will be more effective for inorganic-organic polymer electrolyte membranes. Thus, the composite materials fabricated via wet milling and liquid-phase shaking will be more usable as inorganic additives for the fabrication of polymer electrolyte membrane fuel cells.

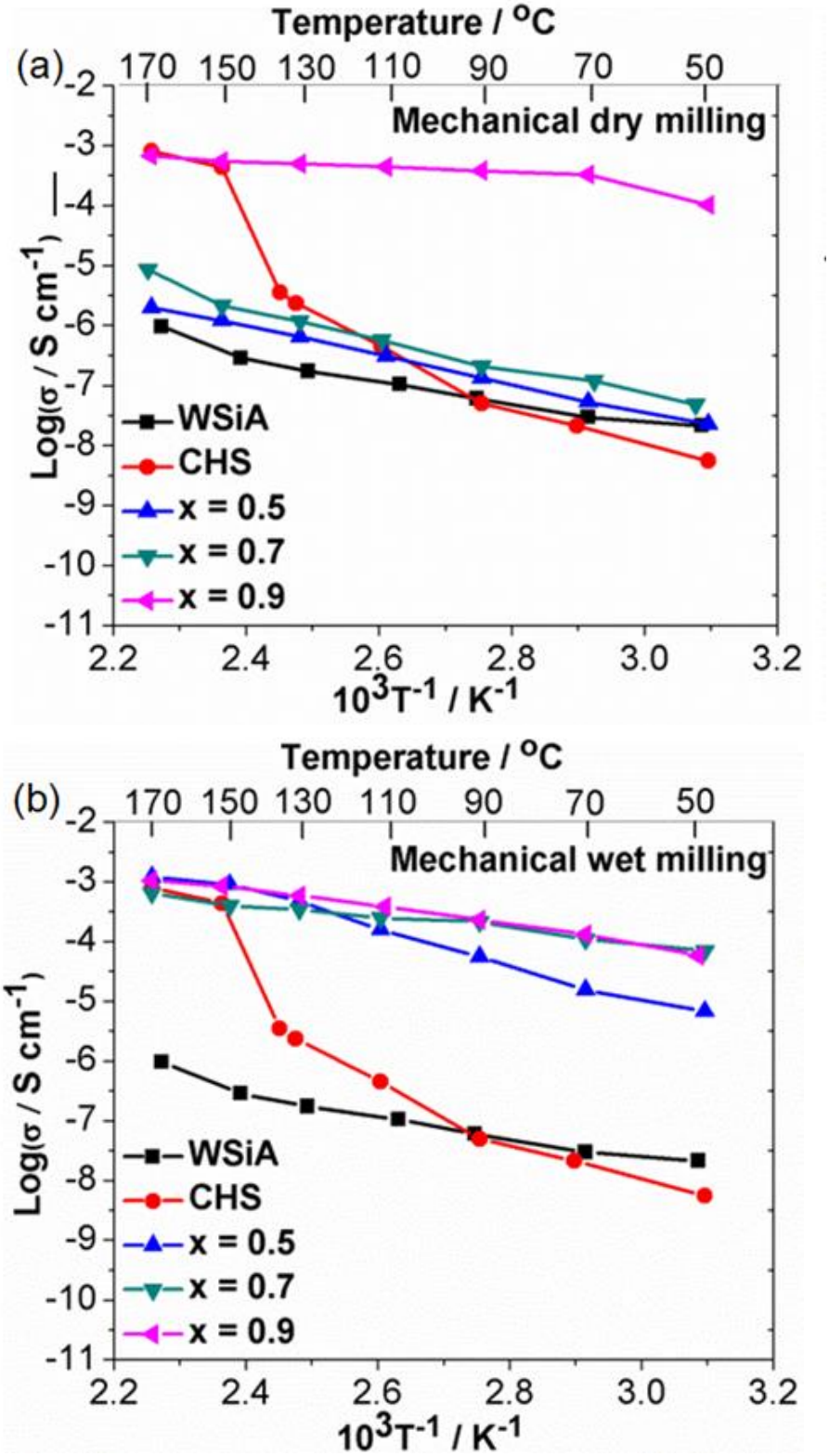

Fig. 2.17. Temperature dependence of anhydrous proton conductivities of WSiA, CHS, and *x*CHS-(1−*x*)WSiA composite materials with x = 0.5, 0.7, and 0.9 produced by mechanochemical (a) dry milling and (b) wet milling.

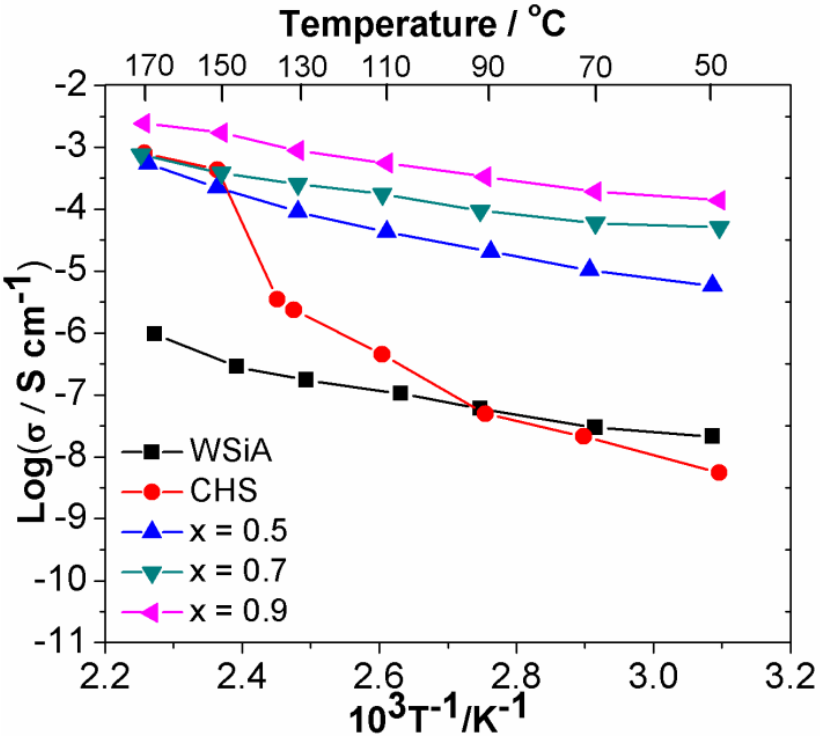

Fig. 2.18. Temperature dependent anhydrous proton conductivities for WSiA, CHS and the prepared xCHS-(1-x)WSiA composite materials via liquid-phase shaking.

2.3.4 Correlation between anhydrous proton conductivity and hydrogen bonding distance under ambient pressure

Solid-state ^{1}H-MAS-NMR spectra were observed to determine the chemical interactions and dynamics of protons in the composite materials and precursor materials, as shown in Fig. 2.19(a), Fig. 2.19(b), Fig. 2.20 respectively. The spectrum of WSiA contained one signal at 8.30 ppm, which was attributed to the proton in WSiA. CHS showed one signal at 10.52 ppm, which was attributed to the proton in CHS. The *x*CHS-(1−*x*)WSiA (*x* = 0.5, 0.7, and 0.9) composites produced via mechanochemical dry milling clearly exhibited proton peaks corresponding to WSiA. As the molar content of CHS increased, the proton peaks of the *x*CHS-(1−*x*)WSiA composites shifted to a lower magnetic field (higher chemical shift), which was consistent with a decreased of hydrogen-bond length. The proton peaks of 0.5CHS-0.5WSiA, 0.7CHS-0.3WSiA, and 0.9CHS-0.1WSiA composites synthesized via dry milling were found around 8.43 ppm, 10.50 ppm, and 11.76 ppm, respectively (relative to TMS). These peak shifts clearly specified that strong chemical interactions formed in these composites during mechanochemical dry milling. The proton signals for *x*CHS-(1−*x*)WSiA (*x* = 0.5, 0.7, and 0.9) composites formed by mechanochemical wet milling shifted to a lower magnetic field (higher chemical shift) of around 11.54 ppm because of the strong chemical interaction between CHS and WSiA. On the one hand, the proton peaks of 0.5CHS-0.5WSiA and 0.7CHS-0.3WSiA composites fabricated via liquid-phase shaking were found around 11.92 ppm and 12.31 ppm, respectively. Increasing the molar concentration of CHS, the prominent proton peaks of composite materials were observed at around 12 ppm. For the high performing 0.9CHS-0.1WSiA composite, a new significant proton peak was detected at around 15.87 ppm. These observations further support the formation of new hydrogen bonds formation between WSiA and CHS in the composite materials which enhance proton conductivity.

Proton peaks at the lower magnetic field correspond to a higher interfacial proton concentration, which means that protons in this region are highly mobile and can enhance proton conductivity under anhydrous conditions. The NMR spectra indicated that a new chemical interaction occurred via the hydrogen bonds between HSO_4^- and partially Cs-substituted WSiA. Thus, the chemical shift of the composite signals exhibited that a new percolation region formed in these composites, which clarifies their improved proton conductivity over that of the precursor materials.

The hydrogen-bond distance (L / pm) between CHS and WSiA can be approximately calculated using the relation,

$$L=100\times(79.05-\delta_{iso})/25.5 \quad (2.1)$$

Where, δ_{iso} is the ^{1}H-MAS-NMR chemical shift, which is expressed in ppm with respect to the TMS signal [19, 26, 28]. In the ^{1}H-MAS-NMR spectra, the identified peak at the lowest magnetic field was chosen to calculate L. The relationship between the L values and proton conductivities at 110 °C of the xCHS-(1−x)WSiA (x = 0.5, 0.7, and 0.9) composite materials fabricated via dry milling, wet milling, and liquid-phase shaking are presented in Fig. 2.21(a), Fig. 2.21(b), and Fig. 2.22, respectively. These relationships indicated that the decrease of L value improves the anhydrous proton conductivity of the composites over a wide temperature range under ambient pressure. Thus, new proton conduction tracks were formed in the composite materials through ion-exchange reaction and hydrogen bonding between HSO_4^- and partly Cs-substituted WSiA. As a result, the anhydrous proton conductivities of the composite materials were evidently developed by the accelerated proton transfer in the interfacial region of the composite materials [1, 21]. This short bonding distance is clarified to result from the large amount of CHS which led to higher amount of Cs^+ ion-substitution into WSiA and ultimately the enhanced formation of H-bonds.

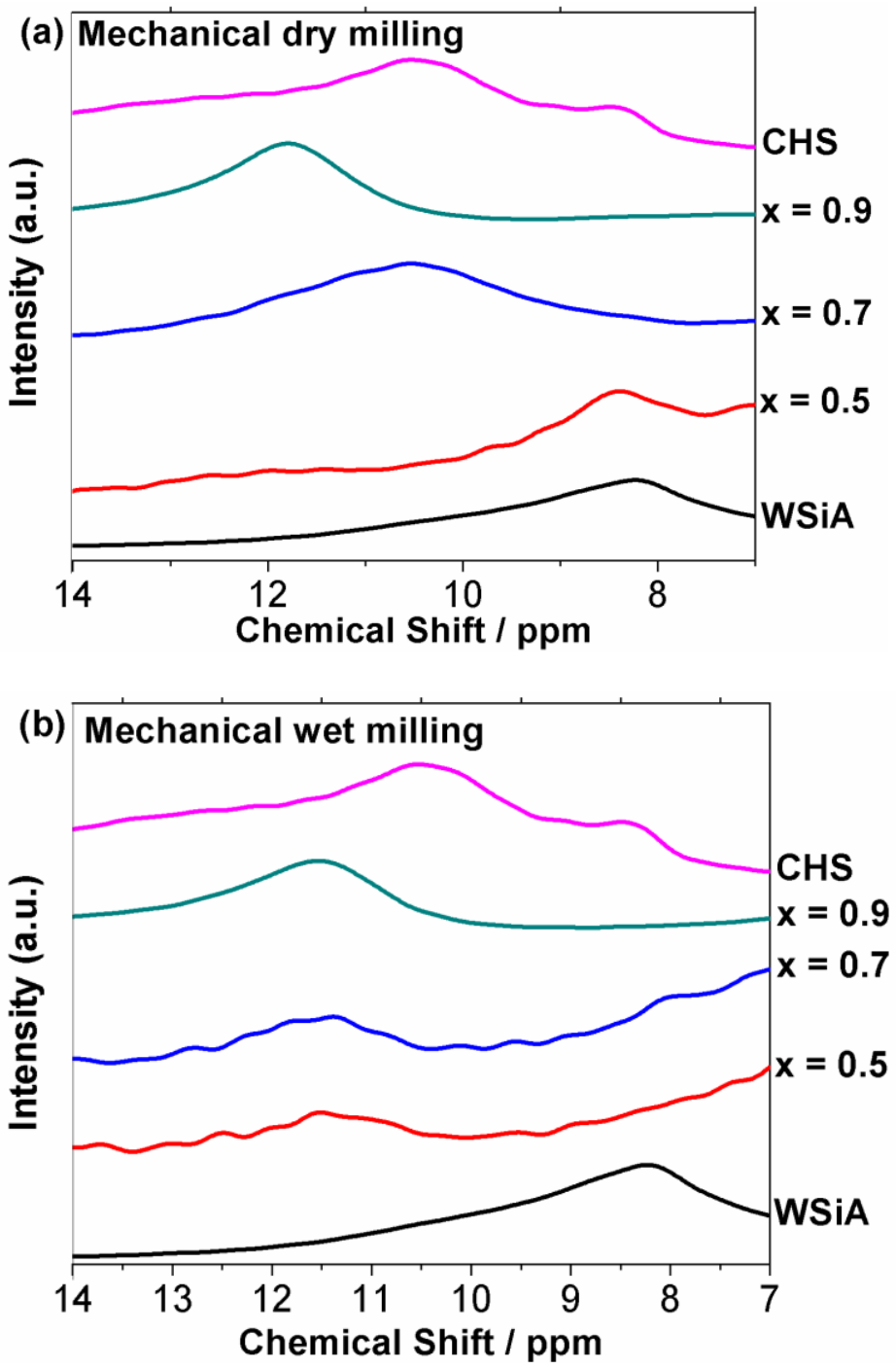

Fig. 2.19. Solid-state ^{1}H-MAS-NMR spectra of WSiA, CHS, and *x*CHS-(1−*x*)WSiA composite materials with x = 0.5, 0.7, and 0.9 produced by mechanochemical (a) dry and (b) wet milling.

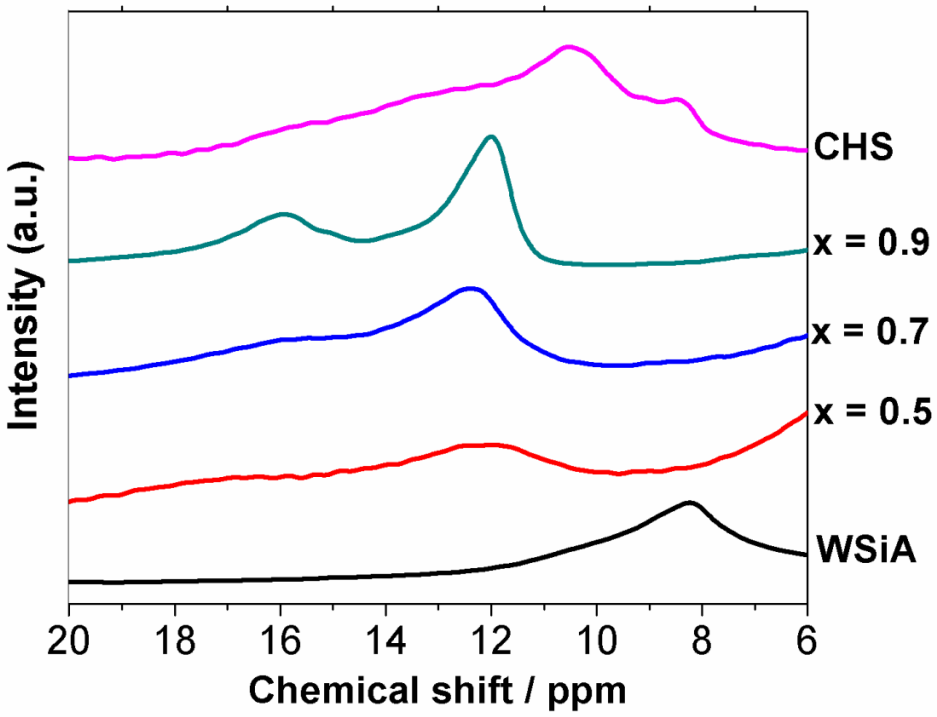

Fig. 2.20. Solid-state ^{1}H-MAS-NMR spectra for WSiA, CHS, and prepared *x*CHS-(1-*x*)WSiA composite materials via liquid-phase shaking.

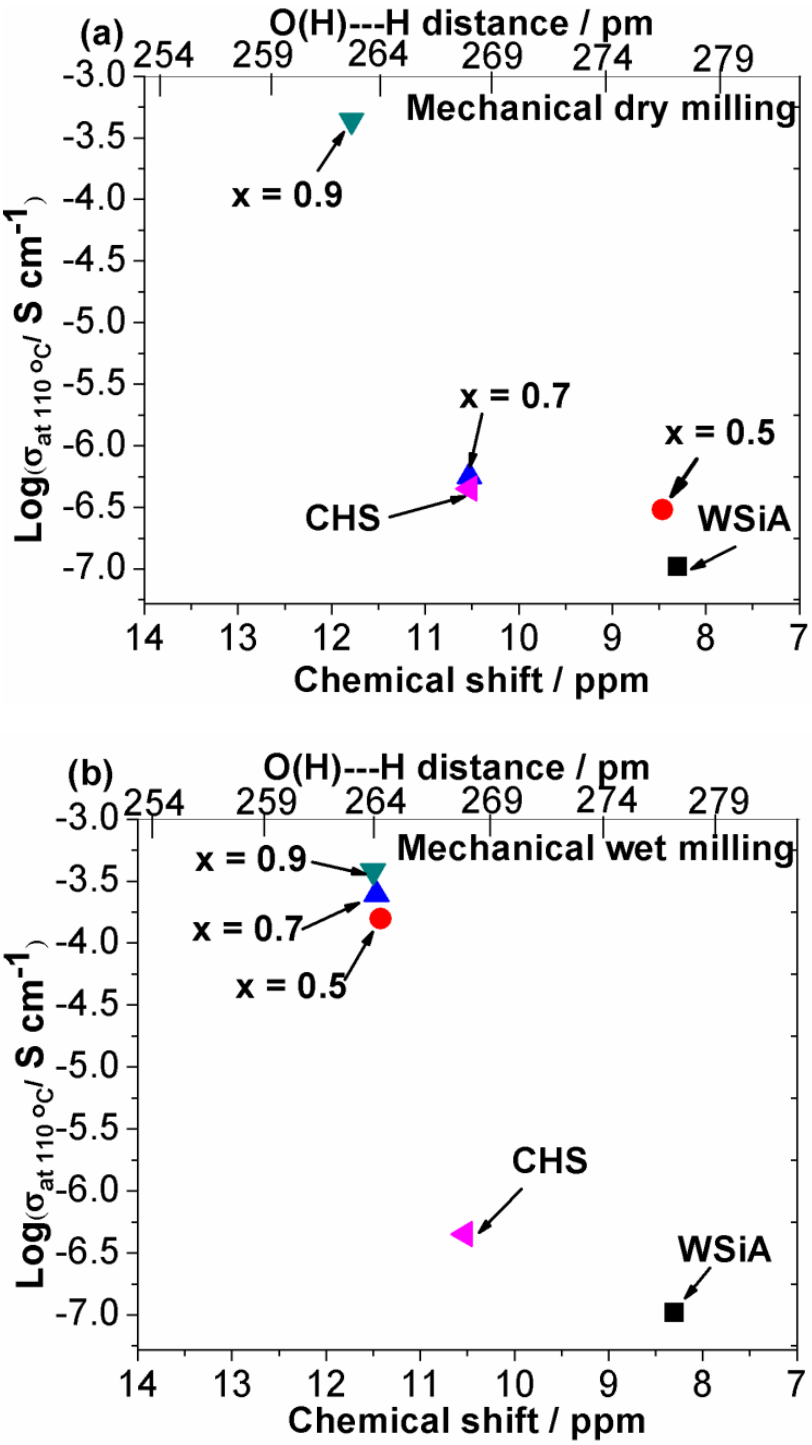

Fig. 2.21. Correlation between hydrogen-bond distance (L) and anhydrous proton conductivity at 110 °C under ambient pressure for WSiA, CHS, and xCHS-(1−x)WSiA composite materials with x = 0.5, 0.7, and 0.9 produced by mechanochemical (a) dry milling and (b) wet milling.

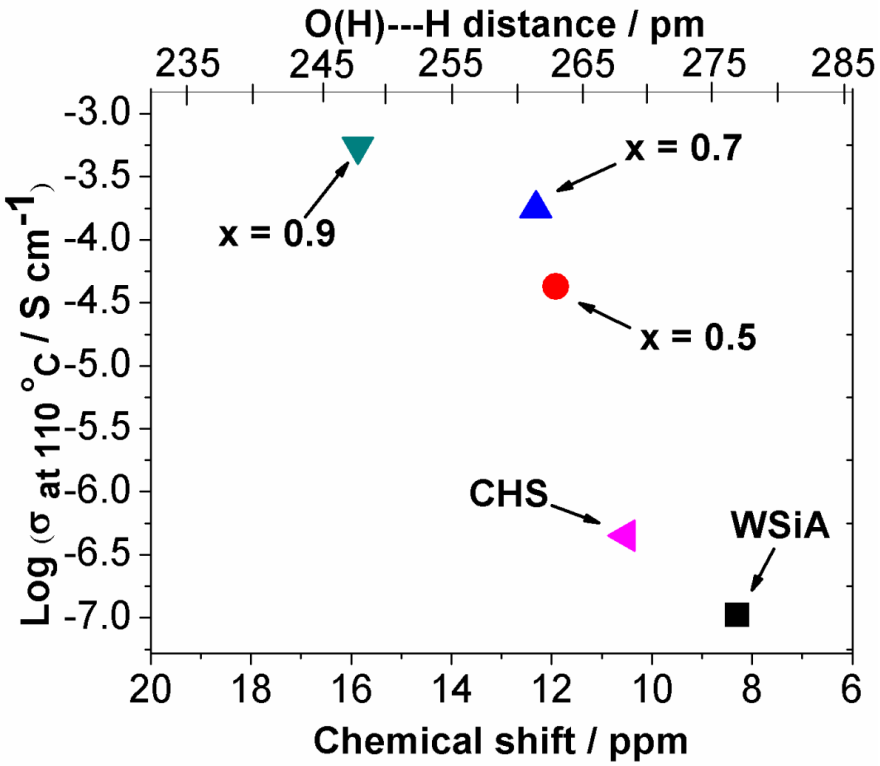

Fig. 2.22. Correlation between hydrogen bond distance and anhydrous proton conductivity at 110 ^{o}C under ambient pressure for WSiA, CHS and *x*CHS-(1-*x*)WSiA composite materials via liquid-phase shaking.

2.4 CONCLUSIONS

*x*CHS-(1−*x*)WSiA composite materials were effectively fabricated via mechanochemical dry milling, wet milling, and liquid-phase shaking. The structural characterization, thermodynamic properties, morphological observation, and the proton transfer of the composites were observed via characterization factors (XRD, FTIR, FT-Raman, FE-SEM, TG-DTA, and ^{1}H-MAS-NMR,). XRD results revealed that the diffraction peaks of the composite materials shifted to higher angles compared with those of the precursor materials, which specified that H^{+} in WSiA were partly exchanged with Cs^{+} ion to form new composite materials during the mechanochemical treatments and liquid-phase shaking. TGA and DTA results demonstrated that the 0.9CHS-0.1WSiA composite materials with the highest proton conductivities formed by dry milling, wet milling, and liquid-phase shaking showed distinguishable peaks that were consistent with a phase transition temperature of around 141 °C, which was caused by some remnant CHS after fabrication of composite materials and the large molar content of Cs^{+} introduced into WSiA. Proton conductivity results revealed that the proton conductivities of the composite materials increased with the content of CHS. In particular, the 0.9CHS-0.1WSiA composite materials produced by dry milling, wet milling, and liquid-phase shaking showed very high conductivities of around 10^{-3} S cm^{-1} at 170 °C. ^{1}H-MAS-NMR spectra indicated that new proton conduction regions formed in the composites via ion-exchange reaction according to the decrease of *L*, which promoted proton transfer. The composite materials fabricated by mechanochemical wet milling and liquid-phase shaking showed conductivities higher than those of the composites fabricated via dry milling, especially for the 0.5CHS-0.5WSiA and 0.7CHS-0.3WSiA composites with low molar content of CHS. These observations implied that the proton conduction mechanisms of the precursor materials and composite materials are quite different. Thus, these high proton conductive composite materials are high potential

candidates to apply as inorganic additive materials for the application of polymer electrolyte membrane fuel cells. Hereafter, liquid phase shaking method promoted the permanent transformation of the composite materials from monoclinic to tetragonal phase exhibiting high proton conductivities in a wide temperature range under ambient conditions from room temperature (RT) to 170 ^{o}C. These observations were clarified to be due to the formation of a proton conduction path at the nano-interface between CHS and WSiA as a result of Cs^{+} substitution into WSiA leading to the formation of short H-bonds which promoted enhanced fast proton percolation. Among them, liquid-phase shaking method can easily be achieved for large mass production without the complicated and more expensive vacuum system. The obtained high proton conducting composites show the high potential applications in proton conducting fields such as sensors and fuel cell electrolytes.

REFERENCES

[1] S.-Y. Oh, T. Yoshida, G. Kawamura, H. Muto, A. Matsuda, Electrochim. Acta **56** (2011) 2364-2371.

[2] P. Staiti et. al, Mater. Lett. **47** (2001) 241–246.

[3] M. Tatsumisago, T. Tezuka, A. Hayashi, K. Tadanaga, Solid State Ionics **176** (2005) 2909-2912.

[4] Y. Daiko, S. Hayashi, A. Matsuda, Chem. Mater. **22** (2010) 3418-3425.

[5] S. Hayashi, M. Mizuno, Solid State Ionics **176** (2005) 745-754.

[6] V. G. Ponomareva, K. A. Kovalenko, A.P. Chupkhin, E.S. Shutova, V.P. Fedin, Solid State Ionics **225** (2012) 420-423.

[7] T. Okuhara, N. Mizuno, M. Misono, Appl. Catal. A **222** (2001) 63-77.

[8] H.-J. Eom, D.-W. Lee, S. Kim, S.-H. Chung, Y. G. Hur, K.-Y. Lee, Fuel **126** (2014) 263-270.

[9] S.-Y. Oh, T. Yoshida, G. Kawamura, H. Muto, M. Sakai, A. Matsuda, Mater. Sci. Eng. B **173** (2010) 260-266.

[10] V.V. Sinitsyn, A. I. Privalov, O. Lips, A. I. Baranov, D. Kruk, F. Fujara, Ionics **14** (2008) 223-226.

[11] D. Aili, Y. Gao, J. Han, Q. Li, Solid State Ionics **306** (2017) 13-19.

[12] S.-Y. Oh, G. Kawamura, H. Muto, A. Matsuda, Electrochim. Acta **75** (2012) 11-19.

[13] S.-Y. Oh, K. Kawai, G. Kawamura, A. Matsuda, Mater. Res. Bull. **47** (2012) 2931-2935.

[14] M. Mizuno, S.Hayashi, Solid State Ionics **167** (2004) 317-323.

[15] S. Hayashi, M. Mizuno, Solid State Ionics **171** (2004) 289-293.

[16] J. Baran, M. K. Marchewka, J. Mol. Struct. **614** (2002) 133-149.

[17] F. J. Berry, G. R. Derrick, M. Mortimer, Polyhedron **68** (2014) 17-22.

[18] S. Sampurnam, T. Dhanasekaran, A. Padmanaban, S. Muthamizh, D. Latha, G. Gnanamoorthy, S. Munusamy, V. Narayanan, Mater. Today: Proc. **5** (2018) 8808-8811.

[19] U. B. Mioč, M. R. Todorović, M. Davidović, P. Colomban, I. H. Antunović, Solid State Ionics **176** (2005) 3005–3017.

[20] L. Pesaresi, D. R. Brown, A. F. Lee, J. M. Montero, H. Williams, K. Wilson, Appl. Catal. A **360** (2009) 50–58.

[21] X. Tong, W. Wu, Q. Wu, F. Cao, W. Yan, A.B. Yaroslavtsev, Mater. Chem. Phys. **143** (2013) 355-359.

[22] M. Amirinejad, S.S. Madaeni, E. Rafiee, S. Amirinejad, J. Membr. Sci. **377** (2011) 89-98.

[23] T. Okuhara, N. Mizuno, M. Misono, Adv. Catal. **41** (1996) 113-252.

[24] Z. Xie, H. Wu, Q. Wu, L. Ai, RSC Adv. **8** (2018) 13984-13988.

[25] J. Mbah, B. Krakow, E. Stefanakos, J. Wolan, Electrochem. Solid State Lett. **12** (2009) E12-E16.

[26] A. Matsuda, S.-Y. Oh, V. H. Nguyen, Y. Daiko, G. Kawamura, H. Muto, Electrochim. Acta **56** (2011) 9364-9369.

[27] A. Matsuda, T. Kikuchi, K. Katagiri, Y. Daiko, H. Muto, M. Sakai, Solid State Ionics **178** (2007) 723-727.

[28] A. Matsuda, V. H. Nguyen, Y. Daiko, H. Muto, M. Sakai, Solid State Ionics **181** (2010) 180-182.

[29] A. Srikanth, B. Viswanadham, V. P. Kumar, N. R. Anipindi, K. V. R. Chary, Appl. Petrochem. Res. **6** (2016) 145-153.

[30] V. V. D. Khastgir, Energy **142** (2018) 313-330.

[31] H. Wu, X. Wu, Q. Wu, W. Yan, Compos. Sci. Technol. **162** (2018) 1-6.

[32] Y.-C. Chiang, D.-S. Tsai, Y.-H. Liu, C.-W. Chiang, Mater. Chem. Phys. **216** (2018) 485-490.

[33] K. Z. Ya, P. Nbelayim, G. Kawamura, H. Muto, A. Matsuda, Solid State Ionics **337** (2019) 1-6.

[34] K.Z. Ya, P. Nbelayim, W. K. Tan, G. Kawamura, H. Muto, and A. Matsuda, E3S Web Conf. **83** (2019) 01008.

[35] N.H.H. Phuc, K. Morikawa, M. Totani, H. Muto, A. Matsuda, Solid State Ionics **285** (2016) 2-5.

[36] S.-Y. Oh, T. Yoshida, G. Kawamura, H. Muto, M. Sakai, A. Matsuda, J. Mater. Chem. **20** (2010) 6359-6366.

[37] A. H. Jadhav, H. Kim, RSC Adv. **3** (2013) 5131-5140.

CHAPTER 3

EFFECT OF MIXED ALKALI METAL IONS IN HIGHLY PROTON CONDUCTIVE K/Cs-HYDROGEN SULFATE-PHOSPHOTUNGSTIC ACID COMPOSITES PREPARED BY MECHANOCHEMICAL MILLING

3.1 INTRODUCTION

Fast proton conductors are currently attracting high interest due to their potential applications in various devices such as electrochemical sensors [1], fuel cells [2], capacitors [3], electrochromic devices and electrochemical reactors [4]; and especially more so as anhydrous proton conductors for the target application in the environmentally sustainable alternative energy source of fuel cells [5]. In this regard inorganic solid acids with the general formula, $MHXO_4$ or MHX (M = monovalent cation; X = S, P, Se, As) and heteropoly acids have been identified as high potential proton conducting materials [6-14]. The inorganic solid acids with the general chemical formula of $MHSO_4$ (MHS) (with M being a large cation, eg Cs^+, Rb^+, NH_4^+, etc) were discovered to exhibit high proton conductivity above a certain superprotonic phase transition temperature, T_{sp} [15, 16]. This is attributed to a phase transition into a plastic phase with high level dynamic structural repositioning of the sulphate tetrahedron, allowing for fast proton transport. Thus, these acids intrinsically have low proton conductivities and high activation enthalpies at ambient conditions. Heteropoly acids (famous as re-usable catalysts in chemical reactions), on the other hand with Kegging-type structure, have very high proton conductivities on the order of 10^{-2} Scm^{-1} under humid conditions and at ambient temperatures and pressures. However, they have poor chemical stabilities such as

very high solubility (eg. Phosphotungstic acid ($H_3PW_{12}O_{40}$; WPA) has a solubility of 200 g/ 100 g water). Thus, a composite of these two solid proton conductors to exploit their good properties suggests potential for high and stable proton conducting materials.

In addition, with the current surge in nanoscience and nanotechnology, it has been suggested that a nanoscale interface control for fast ionic transfer, so called nanoionics effect [17], could lead to high enhanced proton conductivities. Hence, on the basis of the above discussions made so far, there have been some attempts at preparing these composite materials in reported literature. Selezneva et al. [18] studied the structure of $(K0.967(NH_4)0.033)_3H(SO_4)_2$ crystals, belonging to the $K_3H(SO_4)_2$–$(NH_4)_3H(SO_4)_2$–H_2O salt system and found that phase transition kinetics of these materials was determined by the amount of ammonium entering the structure, the type of site they enter and the additional bonds they forms. T. Huang et al. [19] successfully synthesized a Keggin-type vanadium-substituted heteropoly acid, $H_7ZnW_{11}VO_{40}\cdot 8H_2O$, with a transition metal as its central atom. They determined its molecular formula to be $(H_5O_2^+)_2H_5$-$ZnW_{11}VO_{40}\cdot 8H_2O$ and decomposition temperature as 533 °C; with a conductivity of 6.85 x 10^{-4} S cm^{-1} at 18 °C and 3.26 x 10^{-3} S cm^{-1} at 58 °C, at 50% relative humidity. In our previous reports, we have described quite vastly on diverse sectors of this field such as: successful application of KH_2PO_4-$H_3PW_{12}O_{40}$ system as an electrolyte in a fuel cell setup to achieve higher performance than the precursor materials, obtaining a maximum power of 20 mW cm^{-2} at 120 ^oC [6]; investigated the chemical characteristics of $xMHS\cdot(100\text{-}x)H_4SiW_{12}O_{40}$ (M = K, NH_4, Cs) via mechanochemical milling, and observed high proton conductivities of up to orders of 10^{-2} S cm^{-1}, with the highest at x = 80. And using XRD results, showed the substitution of M^+ into $H_4SiW_{12}O_{40}$ and that the reversal of the superprotonic phase was suppressed by the mechanochemical treatment [7]; ^{1}H-MAS-NMR studies of CsHS-WPA to reveal that enhanced anhydrous proton conductivities were directly correlated to new

hydrogen bond distance that forms between the O atom of the WPA and the H atom of the CsHS, with increasing hydrogen bond distance leading to reducing conductivity. The facile technique of mechanochemical milling is a viable route to synthesizing new class of inorganic solid acid composites for enhanced proton conductivities [20]. During a milling process, a relatively high amount of impact (about 35 G; for 720 rpm rotation) is exerted on the precursor materials mix which results in significant distortions, and ultimately structural re-arrangements, in the material mix resulting in the formation of new material product(s). Anhydrous proton conductive cesium substituted-silicotungstic acid ($CsHSO_4$-$H_4SiW_{12}O_{40}$) composite materials were successfully synthesized and reported in our recent publications [21-23]. In this work, we have employed an easy and effective approach using mechanochemical milling to prepare a proton conducting composite material from a mixture of two inorganic solid acids (KHS and CHS) with one heteropoly acid, WPA. The properties obtained are also compared with their single inorganic solid acids counterparts. This is different from previous studies where only one inorganic solid acid is combined with one heteropoly acid. The structural and chemical changes are investigated in order to elucidate the enhanced proton conductivities achieved in comparison to the precursor materials as well as the single inorganic solid acid-single heteropoly acid composites [24, 25]. This finding leads to the observation of the best performing composite in the mixed alkali metal solid acids-heteropoly acid, 90(0.5K0.5Cs)HS-10WPA due to a formation of nanoscale amorphous inorganic acid/heteropoly acid interface from the double metal complementary substitution into the WPA, which induced a network of hydrogen bonds formation.

3.2 EXPERIMENTAL PROCEDURE

Phosphotungstic acid *n*-hydrate [$H_3PW_{12}O_{40}\cdot nH_20$] (Wako Pure Chemical Industries, Japan) was dried at 60 °C in a vacuum oven overnight to reduce the water of crystallization to 6 ($H_3PW_{12}O_{40}\cdot 6H_2O$). The other precursor materials used included, Potassium hydrogen sulfate [$KHSO_4$] (Soekawa Chemicals) and Cesium hydrogen sulfate [$CsHSO_4$] (Mitsuwa Chemical). To prepare the various composite samples (90CHS·10WPA; 90KHS·10WPA; and 90(50K·50Cs)HS·10WPA in mol%), the appropriate amounts of precursor materials to obtain the desired mole portions were mixed in an agate mortar to a total mass of 2 g, in each case. Ten agate balls (ϕ = 10 mm) were added in each case, closed, sealed, and milled under dry nitrogen atmosphere using a planetary ball miller (Pulverisette 7; Fritsch), at 720 rpm for 10 min. The obtained composites were subsequently dried at 100 °C under vacuum overnight.

Solubility tests were carried out via gravimetric by agitating 0.5 g of each sample in 10 ml each of Millipore ultrapure water, followed by 5 min sonification and centrifugation at 10000 rpm for 5 min. KHS, CHS, and WPA precursor materials were completely dissolved in IEW water. The clear supernatant solutions were completely drained and the residual samples were collected with container. Then, they were annealed at 60 ^oC to eliminate water and dried to get constant weight at 110 ^oC overnight. Composite samples with pellets forms were not dissolved in water for a short time but for longer time, these samples were dissolved at about 35 % with severe conditions which were ascribed to the unreacted precursor materials.

Powder X-ray diffraction (XRD) (Rigaku Corporation, Ultima IV) patterns of the composites and precursor materials were measured using a special vacuum sample holder at a tube voltage of 30 kV and current of 20 mA, to investigate the materials structural changes.

The anhydrous (nitrogen atmosphere) proton conductivity performance of the samples was evaluated using AC electrochemical impedance spectroscopy (EIS) over the frequency

range of 10^7-1 Hz from 160 to 40 ^oC in an electric furnace, using a frequency response analyzer (FRA: Toyo Technica Co., Impedance analyzer 1260) based on the software, Z-View SI 1260 Solartron (analysis software) and Smart software (control software).

The measurement samples were prepared by pressing them into pellets at 60 MPa and sandwiched between two conducting carbon paper sheets (ϕ = 13 mm) in contact with stainless steel electrodes at both ends. The setup was held fast by screws and insulated with Teflon sheets. The conductivity σ (S cm^{-1}) was calculated using the equation (3.1):

$$\sigma = d / (R \times A) \tag{3.1}$$

R: Resistance (Ω); *A*: Electrode area (m^2)

The resistance *R* was obtained from the extracted Nyquist plot from the EIS measurement; using the intercept/extrapolated intercept value of the graph with the real axis at the high frequency end (related to proton conduction) [26] based on a simplified equivalent circuit of the bulk resistance of the cell being connected in series to the interfacial capacitance and parallel to the bulk capacitance of the membrane. The resistances of the other components in the experimental setup were not included as the short circuit setup evaluation (i.e. without the membrane) showed a negligible resistance of >> 0.1.

Fourier-transform infrared spectroscopy (FT-IR) (Varian 3100) analysis of the samples was performed to evaluate the bonding, and hence structural, dynamics in these samples. A KBr : sample ratio of 120 : 1 was used. This was supported with Fourier-transform Raman spectroscopy (FT-Raman) (Jasco Co., NRS-3100) measurement.

Solid ^1H magic angle spinning nuclear magnetic resonance (^1H-MAS-NMR) (Brucker AV 400 M digital NMR; resolution: 0.2 Hz; observation frequency: 400 MHz) evaluation was carried out on the samples to investigate the hydrogen bonding and dynamics. The sample was vacuum dried overnight at 100 ° C before measurements. The nanostructure of

the composite materials was evaluated using a high resolution field-emission transmission electron microscopy (HR FE-TEM) (JEOL; JEM-2100 Plus).

3.3 RESULTS AND DISCUSSION

3.3.1 Structural evaluation

The formation of composite materials was confirmed via XRD analysis and the results are shown in Fig. 3.1. The XRD patterns of the pristine precursor samples matched their respective patterns from ICDD reference cards while those of the composites were different (in terms of peak position, peak size and completely new peak formation) from their precursor components, indicating the formation of composite materials induced by the mechanochemical milling treatment. A significant observation worth noting is the prominent $WPA{\cdot}6H_2O$ peak at $2\theta = 25.340°$; this peak is present in all three composites at $2\theta = 25.260$, 25.117 and 25.120° for KHS-WPA, CHS-WPA and mixed alkali metal ion-WPA, respectively. This peak is observed to shift to lower angles in the composites relative to the precursor $WPA{\cdot}6H_2O$ peak, indicating a resultant increase in d-spacing from the substitution of the respective precursor materials (the alkali metals specifically) into the WPA in the composites. A second significant observation is that, these peaks in the composites are less intense and broader than the $WPA{\cdot}6H_2O$ peak; a similar observation for all other peaks in the composites when compared to their corresponding peaks in their precursor components. This is attributed to a combination of two effects: the relatively smaller amounts of these components in the composites as mixtures of these precursor components compared to the pure pristine precursor materials; and secondly as a result of reduced crystallinity and particle size in the composite materials.

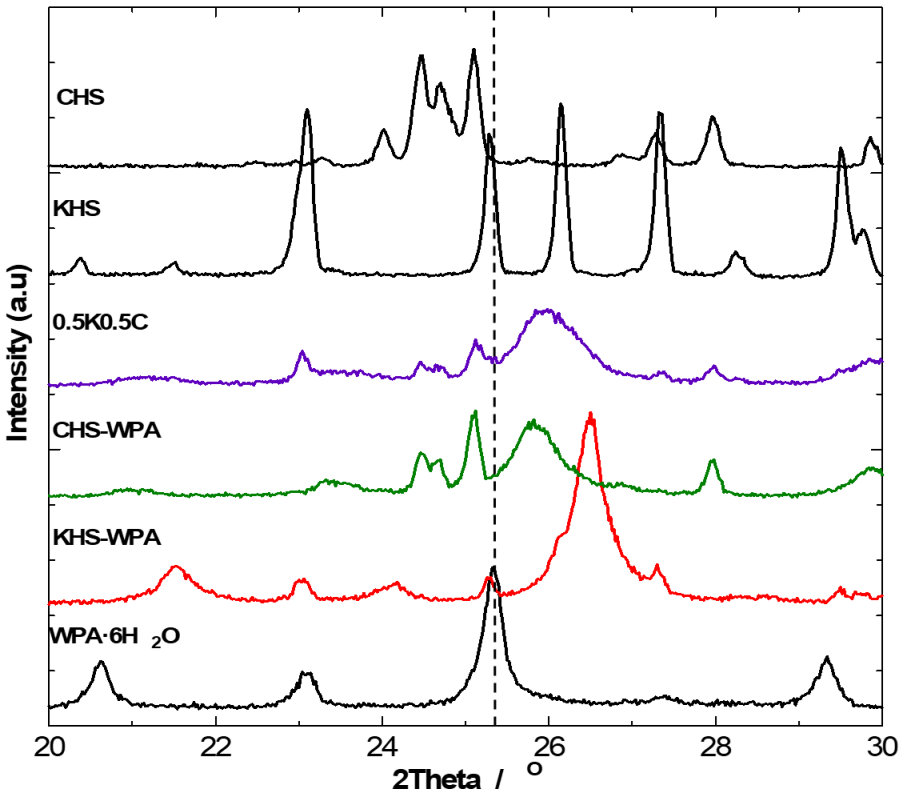

Fig. 3.1. XRD patterns of the pristine precursor materials and composite samples.

Table 3.1. Estimated particle size and d-spacing of precursor and composites materials.

Sample	**Avg. Particle size / nm**	**Particle size @ 2θ = ~ 25.34° / nm**	***d*-Spacing @ 2θ = ~ 25.34° / nm**
WPA	34.8 ± 2.0	28.3	0.35133
KHS	77.0 ± 11.6	-	-
CHS	55.9 ± 4.9	-	-
KHS-WPA	20.3 ± 2.7	53.8	0.35243
CHS-WPA	16.7 ± 0.2	62.7	0.35426
(K·C)HS-WPA	12.5 ± 0.8	48.9	0.35421

From table 3.1, and using Scherrer and Bragg's equations, the average particle sizes and *d*-spacing values of the samples were estimated. Under the "average (Avg.) particle size" column, it can be observed that the composites have smaller particle sizes than the pristine precursor materials; and since the pristine materials were milled under similar conditions as the composites it indicates that the composite mixtures also contribute to the reduction in particle size, in addition to the particle size reduction effect of the mechanochemical milling.

This is further confirmed when it was observed that for pristine WPA the particle size reduced from 66 to 35 nm for before and after ball milling, respectively; while for pristine KHS there was no significant change in particle size of before and after ball milling with values of 81 and 77 nm, respectively. Thus, this supports the additional chemical component effect of the mechanochemical milling treatment. Enhanced particle size reduction for nanoionics effect is one of the main targets of this research; and this is clearly seen under column 3 of Table 3.1.

The column under "Particle size @ 2θ = ~ 25.34°" in Table 3.1 targeted the particle size of the base material, WPA, using the peak position of 25. 34°, which was observed to be present in all the composite materials prepared, although shifted to different extents. Under this column, the trend of particle size is (K·C)HS-WPA < KHS-WPA < CHS-WPA. The relation of this changing particle size in relation to the changing alkali metal inorganic solid acid is interpreted to be due to a contributory effect from the substitution of the alkali metals into the WPA base material. This is corroborated by the *d*-spacing values in column 4 of Table 3.1, obtained at the characteristic WPA peak (2θ = ~ 25.34°) which was observed to be present in the composite materials. These values are larger in the composite materials than in the pristine WPA sample, indicating substitution into the WPA. Among the composite samples the *d*-spacing trend is CHS-WPA > (K·C)HS-WPA < KHS-WPA. This trend can be explained to be due to the relative ionic sizes of the alkali metal ions; Cs with a larger ionic

size (0.181 nm) increases the *d*-spacing the most and K with the smaller ionic size (0.152 nm) increases the d-spacing the least, and hence, in the mixture of the two composite the d-spacing is in between.

Thus, since the particle size trend, using the unique WPA peak region, does not follow as the *d*-spacing and average particle size trends, it indicates that the particle size is not controlled by only the substitution of alkali metal ions into WPA and the mechanochemical effect of the ball milling but also probably an additional chemical reaction effect.

3.3.2 Anhydrous proton conductivity performances

The results from the extracted proton conductivity measurements are shown in Fig. 3.2 a) while the Nyquist plots of the composites and precursors, with their extracted bulk pellet resistances as well as frequencies obtained at 160 °C are shown in Fig 3.2 b) and c), respectively. For CHS precursor, a relatively high conductivity of 4.9 x 10^{-3} S cm^{-1} is recorded at the beginning of the measurement at 160 °C. However, around the temperature region of 141 °C (T_{sp}) a large and sharp decrease in proton conductivity is observed, indicating a phase reversal from the superprotonic tetragonal phase to the low conducting monoclinic phase, and subsequently gradually reducing to an almost non-conducting material around 40 °C, with a conductivity of 1.6 x 10^{-8} S cm^{-1}. Regards the other two precursor materials, KHS and WPA, no superprotonic phase transition is observed, however, they exhibit low conductivities of 5.4 x 10^{-6} to 3.8 x 10^{-7} S cm^{-1} and 2.9 x 10^{-5} to 1.0 x 10^{-7} S cm^{-1}, respectively, over the measured temperature range of 160 to 40 °C, with minimal change. The composite samples however, showed higher conductivities, in ranges of 1.2 x 10^{-2} to 2.0 x 10^{-4} S cm^{-1} and 8.4 x 10^{-4} to 1.4 x 10^{-4} S cm^{-1}, for KHS-WPA and CHS-WPA, respectively, with minimal change indicating higher stability. More significantly, the (0.5K0.5C)HS-WPA composite employing a combination of two alkali metals from the two

inorganic solid acids exhibited the highest performance with a conductivity range of 4.9×10^{-2} to 1.4×10^{-3} S cm^{-1}.

Proton conductivity is mainly affected by the nanoionics effects of small particle size and fast proton conducting nano-interface; suggesting that a material with smaller particle size possesses more effective nano-interface which then lead to better nanoionics effect. From the discussions under section 3.3.1 and of Table 3.1 (K·C)HS-WPA did not have the smallest average particle, however, when considering the base material in relation to the peak around $2\theta = 25.34°$ (K·C)HS-WPA had the smallest particle. Thus, for the mixed (K·C)HS-WPA composite material to exhibit the highest conductivity suggests that the alkali metal mix induced an enhanced nano-interface proton conductive path to achieve the high proton conductivity result obtained. With KHS-WPA as the second highest performing proton conductor among the composites suggests the K^+ alkali metal ion is playing a probably unique role towards the formation of the nano-interface in a synergistic effect with the Cs^+ ion.

Fig. 3.3 shows the relationship between the average ionic radius of the MM-treated cation and conductivity at 160^oC under nitrogen atmosphere for the 90(0.5K0.5Cs)HSO_4· 10WPA (mol%) composite. Average ionic radius of the cations (K^+ and Cs^+) was the key factor which substituted with H^+ ions in WPA for the enhancement of conductivity under non-humidified conditions. The conductivity improved with the increment of the average ion radius from 1.5 to 1.65 Å. However, the conductivity showed a tendency to reduce when the average ionic radius is beyond 1.65 Å. This observation indicates that the conductivity can be improved through the optimization of plural alkali metal ions' ionic radius as the ions used for element substitution have an optimum ionic radius.

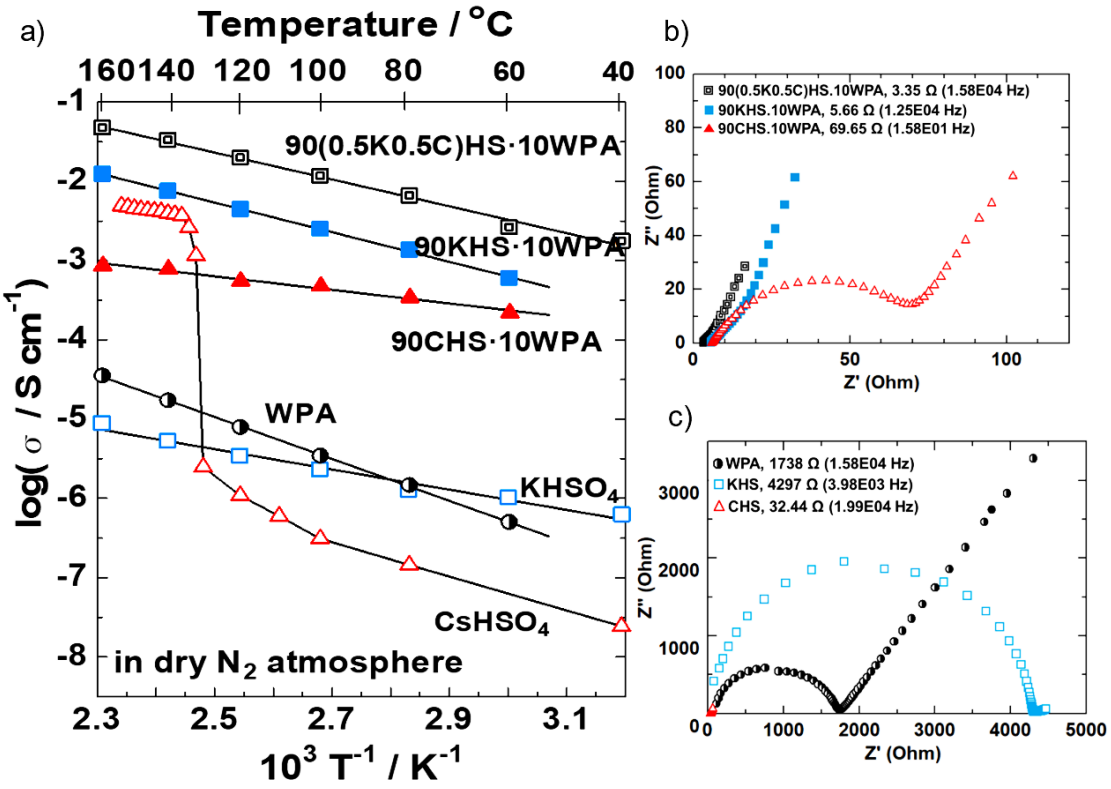

Fig. 3.2. a) Temperature-dependent anhydrous proton conductivities of composite materials and precursor materials; Nyquist plots of b) composites and c) precursor materials.

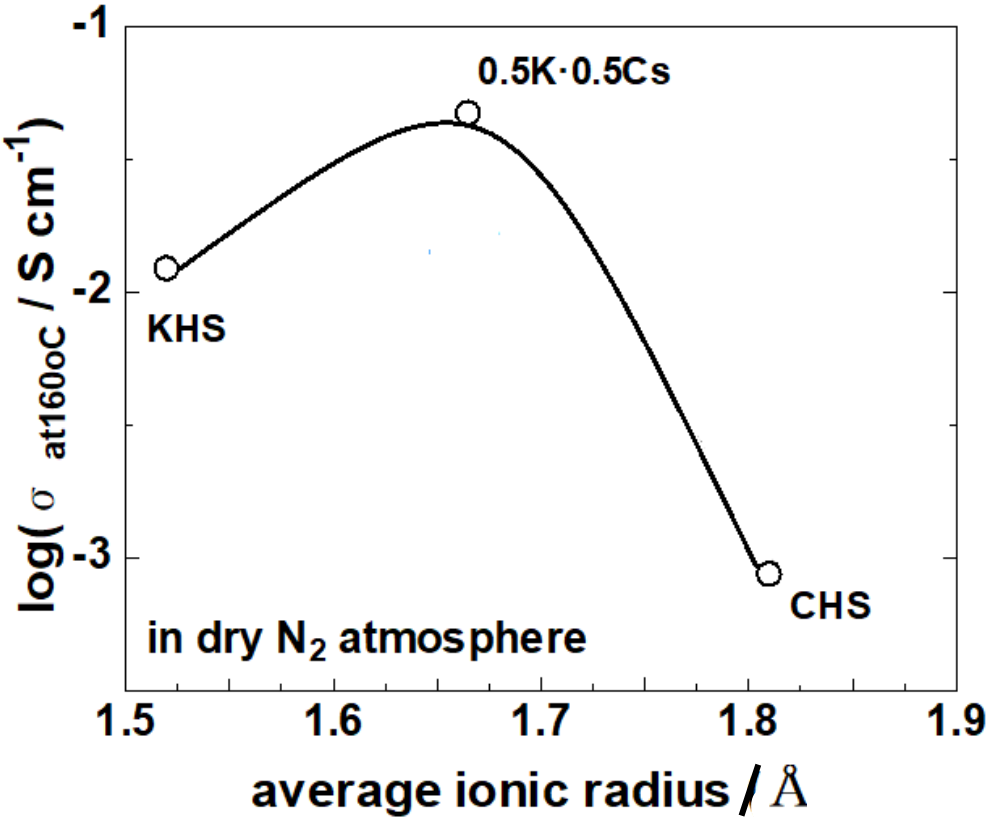

Fig. 3.3. The relationship between the average ionic radius of the cation using MM treatment and conductivity at 160^{o}C under Nitrogen atmosphere of 90(0.5K0.5Cs)HSO_4· 10WPA (mol%) composites.

3.3.3 Mechanochemical induced structural/chemical changes

To determine the chemical changes that occurred to form the fast proton conducting composites the IR, Raman and NMR spectroscopic studies of the samples were carried out. These spectroscopic techniques provide information on the structure and binding energy of phosphate–sulfate tetrahedrons and the potential changes in hydrogen bond networks which are thought to comprise the proton conductive pathways in the new composites prepared.
Since the XRD results showed WPA as the base material being substituted into by KHS and CHS, a schematic of the Keggin structure of WPA is shown in Fig. 4 identifying the potential reaction sites/oxygen types for easy understanding.

Fig. 3.5 shows the FT-IR results. In Fig. 3.5 a) bands observed around 1200, 1066 and 580 cm^{-1} are related to the asymmetric stretching, symmetric stretching and asymmetric bending modes of SO_4 group in the CHS and KHS [27-30]. These bands have been observed in the composites (except the symmetric stretching band) and generally shift to higher wavenumbers, which suggests a weakening of the bonds and hence indicates that these groups have been involved in new chemical reactions; ascribed to the formation of hydrogen bonds using the H attached to these groups. The bands around 3430 cm^{-1} (Fig. 3.5 b)) and 860 cm^{-1} (Fig. 3.5 a)) is ascribed to the stretching and bending modes of the OH group in the HSO_4 group [27-30]. These bands are absent in the composites, suggesting the involvement of the OH group in hydrogen bonding.

Fig. 3.5 a) also shows the four characteristic bands of WPA around 1080, 987, 891 and 814 cm^{-1}; attributed to the stretching vibrations of P-O, $W=O_d$, $W-O_b-W$ and $W-O_c-W$ bonds, respectively [29-30].

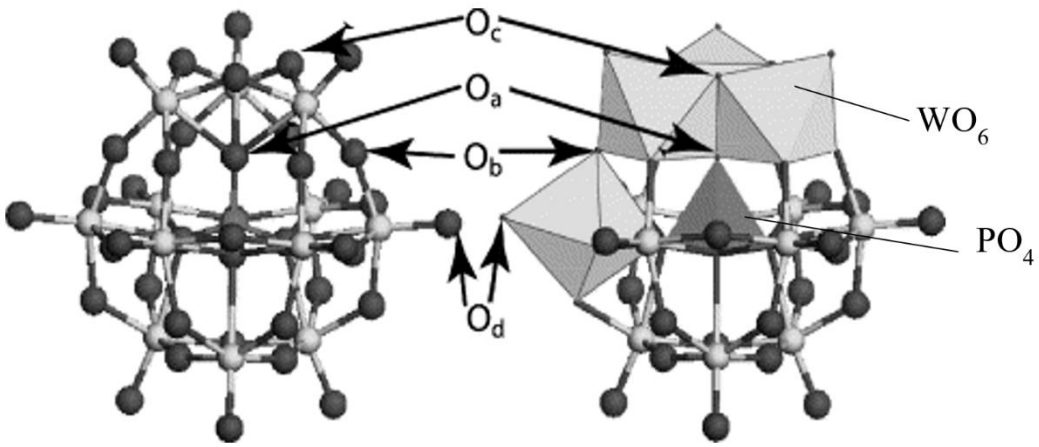

Fig. 3.4. The Keggin structure of WPA ion $[PW_{12}O_{40}]^{3-}$ identifying the four types of oxygen atoms/potential reaction sites in the structure:

— 4 O_a is the W atom-PO_4 O atom bond;

— 12 O_d, terminal oxygens linked to a lone W atom;

— 12 O_b in W–O_b–W bridging corner O atom of W_3O_{13} groups of different octahedra; and

— 12 O_c, in a W–O_c–W bridging edge O atom of W_3O_{13} groups of the same octahedra.

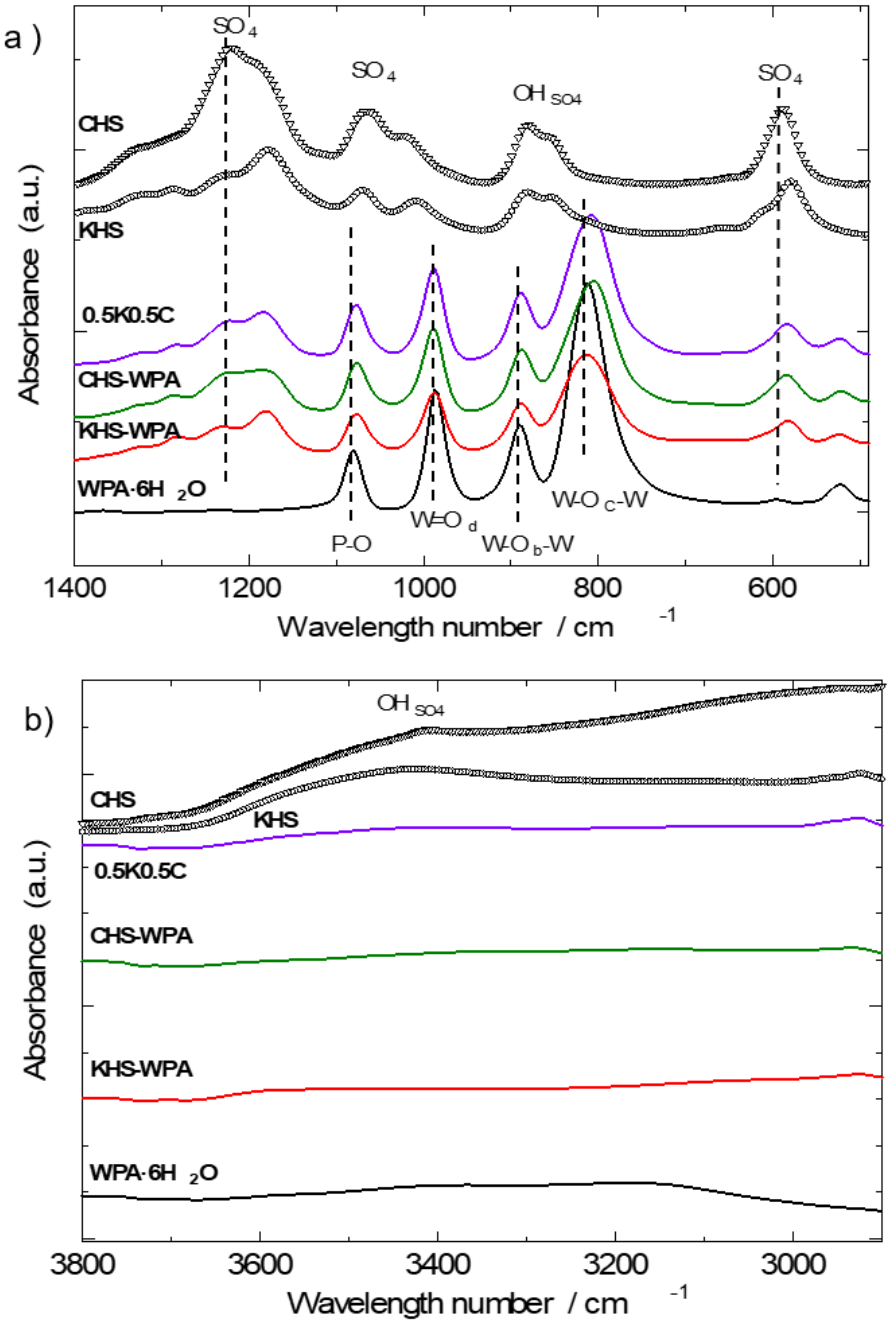

Fig. 3.5. FT-IR spectra of the precursor materials and composite materials in the wavenumber regions of: a) 1400 - 490 cm^{-1}; and b) 3800 - 2900 cm^{-1}.

These bands are also observed in all the composites since WPA is the base material and their bands for these bonds are generally observed to shift to lower wavenumbers, indicating that these bonds have been weakened/elongated in the composites and ascribed to the engagement of the electronegative oxygen atoms of the P-O_a-W O atom (P-O); the terminal O atom (W=O_d), the bridging corner O atom (W-O_b-W), and the bridging edge O atom (W-O_c-W), respectively) in hydrogen bonding with the H atoms from the KHS and CHS salts. However, for all the composites the band for the terminal O, W=O_d, does not shift and seems to suggest it is not involved in hydrogen bonding. From basic chemistry, this edge O should be the most active in the formation of hydrogen bonding, since it is more electron rich with its additional double bond and the electron lone pair; and the least sterically hindered. Nevertheless, this is in agreement with the works of Bardin et al. [31] who observed, by quantum chemical calculations, that the most energetically favorable site of the acidic proton is a bridging O atom.

Another apparent discrepancy is the KHS-WPA sample whose bands do not shift at all the O hydrogen bonding bands except for those of the sterically hindered O atoms of P-O and W-O_b-W. This is attributed to the observation that the larger Cs^+ seems to be more favored by O sites for cation substitution and ultimate protonic attachment for hydrogen bonding; however, at the sterically hindered sites the relatively smaller size K^+ ion is not easily displace by the sterically hindered Cs^+ ion or water clusters (from exposure to ambient conditions during sample preparation and measurement). This assertion is supported by the proton conductivity results of Fig. 3.2: it can be observed that the composites containing the K^+ ion (KHS-WPA and mixed composites) show higher conductivities ascribed to enhanced hydrogen bond formation as a consequence of enhance alkali metal ions substitution. However, when considering the range of change in proton conductivity over the measuring temperature range, the CHS-WPA composite exhibits the least change (~ 0.5 log units),

which is an indication of stability, but the lowest conductivity, an indication of fewer hydrogen bonds from less alkali ion substitution. While KHS-WPA, which contains only K^+ ions exhibited the highest change (~ 1.1 Log units), but a higher conductivity than CHS-WPA; and followed by (K·C)HS-WPA (~ 1.0 log units) that contains the K^+ ions in addition to the more stabilizing Cs^+ ion, and hence the highest conductivity.

In Raman analysis the effects of the mechanochemical treatment on the formation of the composite materials structures are observed too, as shown in Fig. 3.6. The peaks in Raman spectra are related to the presence and strength/length of bonds; where a peak shift to a higher wavenumber indicates the strengthening/shortening of the bond, and vice versa. Peak intensities are related to the amount and/or crystallinity of a molecule; where a reduced intensity indicates a reduced amount of the molecule and/or reduced crystallinity, and vice versa. The labelled peaks of interest in the composites do not match those of the pristine starting materials, indicating the formation/modification of bonds as a resultant consequence of induced chemical reactions from the mechanochemical treatment. The bands between 990 and 1015 cm^{-1} wavenumbers are attributed to the symmetric stretching of the SO_4 groups of the KHS and CHS pristine precursor materials; around 400 and 590 cm^{-1} to the asymmetric bending of these groups; and around 850 cm-1 to the S-O-H bending of their HSO_4 groups [30]. These groups are not observed in the composites and thus attributed to their reaction with the base kegging structure material, WPA.

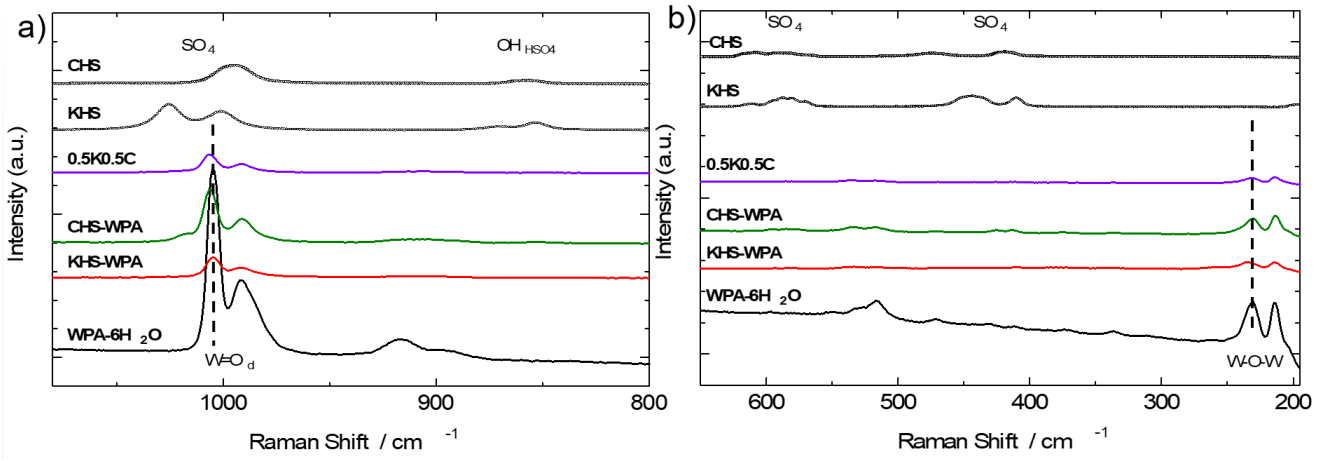

Fig. 3.6. Raman spectra of the precursor materials and composite materials in the Raman shift regions of: a) 1080 - 800 cm^{-1}; and b) 680 - 198 cm^{-1}.

The bands at 1005 and 991 cm^{-1} are attributed to the symmetric and asymmetric stretching of the $W=O_d$ bond of WPA, respectively; and 220 cm^{-1} to the bending of the bridging W-O-W bonds of WPA [32]. At the less energetically favored $W=O_d$ band the composites containing the observed more favored or stable Cs^+ substitution (CHS-WPA and mixed alkali ions) is observed to shift to higher wavenumber, indicating the substitution of the ion into the WPA structure, displacing water/proton clusters and consequently strengthening of the $W-O_d$ bond by increasing the electron cloud per unit ionic species surrounding/attached the electronegative O atom; while the observed less desirable or easily displaced K^+ ion only containing composite (KHS-WPA) does not shift. However, around 230 cm^{-1}, attributed to $W-O_b-W$ (the sterically hindered corner bridging O), only smaller K^+ ion containing composites (KHS-WPA and mixed alkali ions) shift to indicate substitution into WPA. This corroborates the assertion of the effects of ionic size, steric hindrance effect around potential substitution site and stability/desirability of substituting ion on the formation of these solid proton conducting composites via mechanochemical treatment.

In Fig. 3.6 it is observed that the spectral peaks of the composite materials are less intense than the precursor materials. These reduced intensities are attributed to the reduced relative amounts of WPA upon the addition of CHS and KHS in the composites and reduced crystallinity. The reduced crystallinity is corroborated by the broadening of the $W=O_d$ peaks in the composites relative to that in the pristine WPA. This also corroborates the observation made in the XRD results.

The solid NMR evaluation was carried out to investigate proton dynamics induced in the prepared composites. The results are shown in Fig. 3.7. The peaks in the spectra represent protons in the samples; their different positions arising from their different chemical environments of and within the samples; and the area of the peaks give indications as to the amount of the particular proton type present.

From Fig. 3.7 it can be observed that the pristine samples have single peaks which indicates that all their protons are in the same chemical environments, respectively; while the composite samples have peaks (12.4 ppm) with shoulders (11.5 ppm) (two clear peaks in the case of the mixed alkali metal composite; 12.2 and 9.4 ppm) and at higher chemical shift positions. This corroborates the formation of new materials and their higher chemical shift positions indicates the emergence of higher acidic protons, hence their higher proton conductivities than the pristine precursor materials.

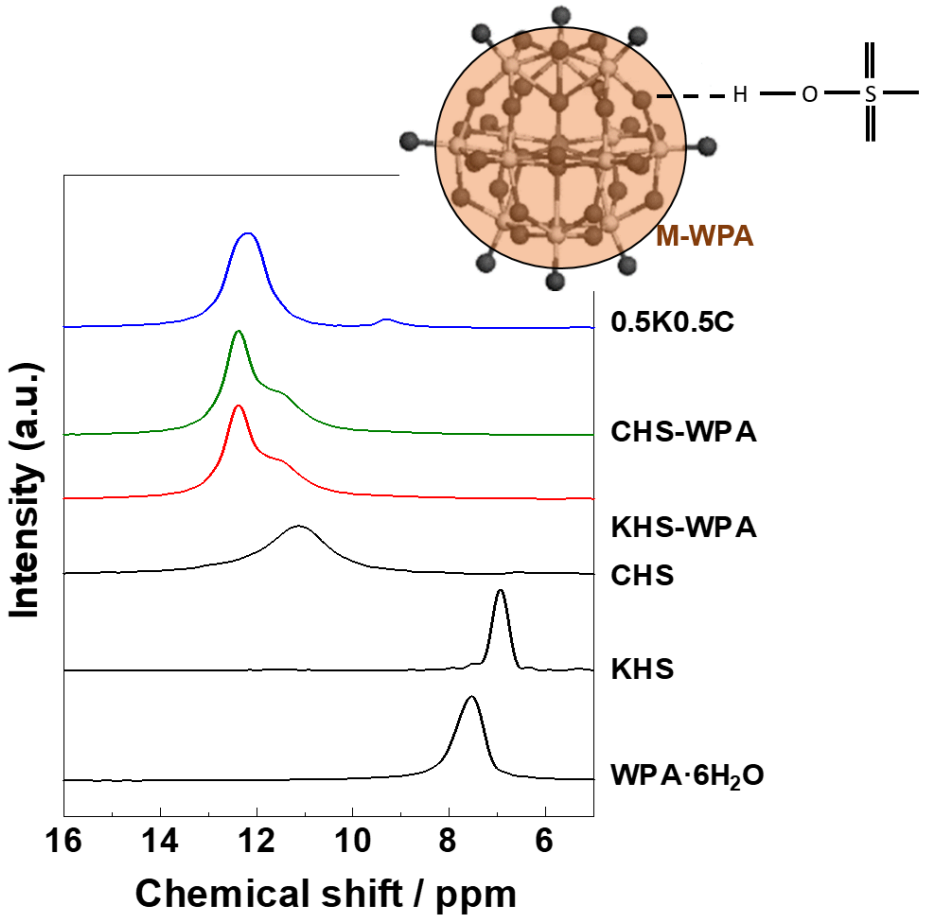

Fig. 3.7. Solid-state ^{1}H-MAS-NMR spectra of the precursor materials and composite materials; Inset: schematic of the formation of a hydrogen bond between a bridging atom of M-substituted WPA and HSO_4 of MHS.

The chemical shift of the pristine WPA·$6H_2O$ is a narrow peak around 7.5 ppm; this is attributed to protons from water clusters of very fast exchange among all available hydrogen in the water clusters [33]. The peak position of 11.1 ppm of CHS is attributed to the phase III of the monoclinic symmetry of CHS [34]. The new peaks at higher chemical shifts are attributed to the formation of hydrogen bonded protons from HSO_4^- ion from the MHS salts with alkali metal substituted kegging structure, $M_3PW_{12}O_{40}$ as shown in the inset image of Fig. 3.7; and the shoulder peaks (extra peak in mixed alkali composite) to either remnant unreacted protons or residual moisture in the composites.

The formation of the new hydrogen bonds between the WPA and MHS species is thought to result in the formation complex random 3D networks of amorphous nano-interface in the region between a base WPA and MHS units; with high proton concentration of flexible mobility and dynamism, which leads to high proton conductivity, as observed in the composite materials prepared. An HR FE-TEM image of KHS-WPA in Fig. 3.8 supports this assertion of amorphous nano-interface. As can be seen, the composite consists of a distribution of a core-shell (dark-light) pattern network: a single crystalline core of aggregates of K-substituted WPA (K-WPA), observed as crystalline fringes with a corroborating electron diffraction pattern in the inset image, and an amorphous shell than runs continuously around the crystalline aggregates. This nanoscale continuous amorphous phase is ascribed to the proton-rich nano-interface with nanoionics effect. The schematic diagram at the bottom of Fig. 3.8 illustrates the formation of the nanoionics interface.

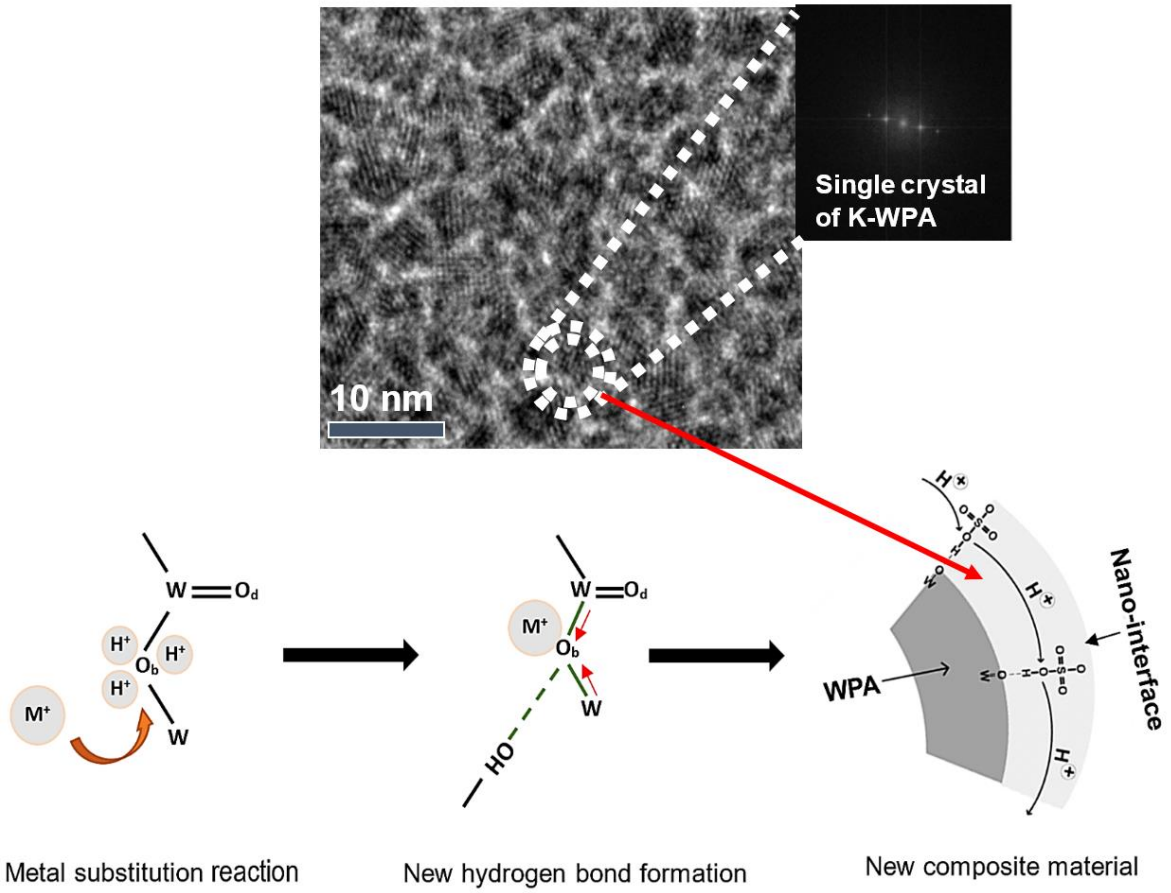

Fig. 3.8. An HR FE-TEM image (inset: electron diffraction pattern) of a KHS-WPA composite material exhibiting superprotonic amorphous shell and crystalline aggregate core; and a schematic of a proposed mechanism of the mechanochemical synthesis route leading to the superprotonic nano-interface.

3.4 CONCLUSION

This research investigated the effect of mixed alkali metals inorganic solid acids of KHS and CHS on the anhydrous proton conductivity in the form of a composite material with WPA; prepared by a mechanochemical milling method. These investigations were done with reference to the pristine precursor materials and the single metals MHS-WPA composites. Evaluation of XRD, FT-IR, FT-Raman, ^{1}H-MAS-NMR and HR FE-TEM results confirmed the formation of new composite materials. Temperature-dependent anhydrous proton conductivities of these materials, in a reducing temperature regime (160 to 40 °C) showed that the mechanochemical milling induced a chemical change in the composite materials to irreversible superprotonic phases, with the mixed alkali metals composite exhibiting the highest conductivities from 4.9 x 10^{-2} to 1.4 x 10^{-3} S cm^{-1} of a temperature range of 160 to 40 °C. Generally, the composites performed far better in terms of both stability and conductivity on the orders of 3 to 4, using the best composite and least pristine precursor materials in the measured temperature range. The results showed the enhanced conductivities in the composites resulted from the formation of a superprotonic nano-interface of a complex hydrogen bonding network between MHS and WPA, induced by the substitution reaction of the metal cations into the kegging structure ion. It also showed that the bridging oxygen atoms of the Kegging structure were the preferred sites of substitution; with Cs^{+} ions being the more preferred with higher stability and K^{+} ions the more preferred at the sterically hindered oxygen atoms, with lower stability but higher conductivity. The high proton conductive inorganic composite materials obtained will serve as good material in the anhydrous proton conductor material application fields; with our interest in the application in organic-inorganic electrolyte fuel cell membranes. The results also inspire further research with regards to the preferred, more stable and high proton conducting substituted alkali metal ion composite.

REFERENCES

[1] A. Miyamoto, Y. Kuwaki, T. Sano, K. Hatakeyama, A. Quitain, M. Sasaki and T. Kida, ACS Omega **2** (2017) 2994-3001.

[2] T. Norby, J. Chem. Eng. Jpn. **40** (2007) 1166-1171.

[3] T. Hibino, K. Kobayashi, M. Nagao and S. Kawasaki, Sci. Rep. **5** (2015) 7903.

[4] F. W. Poulsen, Proton Conduction in Solids in: T. Takehiko (Eds.), World Scientific Publishing Company. Singapore (1989) 166-200.

[5] A. Pawłowski, M. Połomska , K. Pogorzelec-Glaser, B. Hilczer, A. Pietraszko, E. Markiewicz, P. Ławniczak and L. Szcześniak, Phase Transit. **83** (2010) 854-867.

[6] S-Y. Oh, T. Kikuchi, G. Kawamura, H. Muto and A. Matsuda, Appl. Energy **112** (2013) 1108-1114.

[7] S-Y. Oh, K. Kawai, G. Kawamura, H. Muto and A. Matsuda, Mater. Res. Bull. **47** (2012) 2931-2935.

[8] S-Y. Oh, G. Kawamura, H. Muto and A. Matsuda, Solid State Ionics **225** (2012) 223-227.

[9] A. Matsuda, S-Y. Oh, V. H. Nguyen, Y. Daiko, G. Kawamura and H. Muto, Electrochim. Acta **56** (2011) 9364-9369.

[10] A. Matsuda, T. Kikuchi, K. Katagiri, H. Muto and M. Sakai, Solid State Ionics **177** (2006) 2421-2424.

[11] J.-D. Kim, I. Honma, Solid State Ionics **176** (2005) 547-552.

[12] K.D. Kreuer, M. Hampele, K. Dolde, A. Rabenau, Solid State Ionics **28-30** (1988) 589-593.

[13] U. Mioč, M. Davidović, N. Tjapkin, P. Colomban, A. Novak, Solid State Ionics **46** (1991) 103-109.

[14] I. Honma, H. Nakajima, O. Nishikawa, T. Sugimoto, S. Nomura, Solid State Ionics **162-163** (2003) 237-245.

[15] K-D. Kreuer, Chem. Mater. **8** (1996) 610-641.

[16] A. I. Baranov, A. L. Shuvalov, N. M. Schagina, JETP Lett. **36** (1982) 381-384.

[17] A. L. Despotuli and V. I. Nicholaichik, Solid State Ionics **60** (1993) 275-278.

[18] E. V. Selezneva, I. P. Makarova, V. V. Grebenev, and V. A. Komornikov, Crystallogr. Rep. **63** (2018) 178-185.

[19] T. Huang, X. Wu, Q. Wu and F. Cao, Funct. Mater. Lett. **8** (2015) 1550041.

[20] A. Matsuda, T. Tezuka, Y. Nono, K. Tadanaga, T. Minami and M. Tatsumisago, Solid State Ionics **176** (2005) 2899-2904.

[21] K. Z. Ya, P. Nbelayim, G. Kawamura, H. Muto, A. Matsuda, Solid State Ionics **337** (2019) 1-6.

[22] K. Z. Ya, P. Nbelayim, W. K. Tan, G. Kawamura, H. Muto, and A. Matsuda, E3S Web Conf. **83** (2019) 01008.

[23] K. Maegawa, K. Z. Ya, W. K. Tan, G. Kawamura, T. Hattori, H. Muto, A. Matsuda, Mater. Lett. **253** (2019) 201-204.

[24] A. Matsuda, V. H. Nguyen, Y. Daiko, H. Muto, M. Sakai, Solid State Ionics **181** (2010) 180-182.

[25] Y. Daiko, S. Hayashi, A. Matsuda, Chem. Mater. **22** (2010) 3418-3425.

[26] T. Soboleva, Z. Xie, Z. Shi, E. Tsang, T. Navessin and S. Holdcroft, J. Electroanal. Chem. **622** (2008) 145-152.

[27] I. N. Bagryantseva, V. G. Ponomareva, Solid State Ionics **225** (2012) 250-254.

[28] J. Baran, M. K. Marchewka, J. Mol. Struct. **614** (2002) 133-149.

[29] N. Essayem, A. Holmqvist, P. Y. Gayraud, J. C. Vedrine, Y. B. Taarit, J. Catal. **197** (2001) 273-280.

[30] A. Periasamy, S. Muruganand, M.Palaniswamy, RJC **2** (2009) 981-989.

[31] B. B. Bardin, S. V. Bordawekar, M. Neurock, R. J. Davis, J. Phys. Chem. B **102** (1998) 10817-10825.

[32] A. Martinelli, A. Matic, P. Jacobsson, L. Börjesson, M.A. Navarra, D. Munaò, S. Panero, B. Scrosati, S. Panero, B. Scrosati, Solid State Ionics **178** (2007) 527-531.

[33] N. Essayem, Y. Y. Tong, H. Jobic, J. C. Vedrine, Appl. Catal. A **194-195** (2000) 109-122.

[34] A. R. Lim, M. Hyung, Chem. Phys. **459** (2015) 59-64.

CHAPTER 4

PROTON CONDUCTIVE CESIUM-SUBSTITUTED SILICOTUNGSTIC ACIDS DOPED-POLYBENZIMIDAZOLE AND THEIR APPLICATIONS IN MEDIUM TEMPERATURE FUEL CELLS

4.1 INTRODUCTION

At present, environmental safety is of noteworthy importance for human beings as well as their lives of future generation. One of the harmful impacts of the environment is the large usage of electrical energy which growths day by day. In our daily survives, people strongly need energy, and the primary sources of energy are providing via the incineration of fossil fuels, which leads to huge levels of air pollution and the emission of greenhouse gasses [1]. To solve these challenges, new energy production technologies have to be progressive for upcoming energy production for our daily lives. Therefore, fuel cells are the great potential candidates for new energy production system. The fuel cell can make directly conversion from chemical energy to electrical energy as an electrochemical cell between fuels. Fuel cells are one of power generations with high attention because they perform to enhance power conversion efficiency with a reduction of pollution levels. In particular, the electrolyte membrane is a main component in fuel cell performance to produce electrical power [2]. Polymer electrolyte membrane fuel cells (PEMFCs) contain perfluorosulfonic acid electrolyte such as Nafion® which is one of the most production methods for clean energy and are explored for usage as power sources for energy converters. They present positive characteristics, such as high performance like power density and conductivities, good efficiency and tolerance of pollutant levels. But, PEMFCs need humid condition for proton generation with low fuel cell performance and efficiency under the operating temperature (< 100 ^{o}C). Hence, to increase the fuel cell performance and efficiency of PEMFCs, a high

operating temperature and kinematic reaction are necessary for high fuel cell efficiency [3-10]. After increasing the operating temperature (>100 ^{o}C) for PEMFCs, they are improved with faster kinematic reaction, higher tolerance for impurities in the fuel stream, and affable thermal-water maintainance. Thus, polybenzimidazole (PBI) is the most attractive water insoluble polymer among the non-fluorinated ionomers (non-PFI) under active development because it shows good properties not only as an electronic insulator but also an ionic insulator. Polybenzimidazoles are also a class of tremendously heat-resistant heterocyclic thermo-engineering plastics. They are synthesized from an aromatic tetra-amine and an aromatic di-carboxylic acid or a derivative of it. A well-known example is the condensation reaction of diphenyl isophthalate and 3,3',4,4'-tetraaminodiphenyl which undergo spontaneous cyclization at temperatures around 350 to 400 °C in an inert atmosphere. Polybenzimidazole and their derivatives are very expensive and difficult to manufacture but have outstanding properties. They possess a very high glass transition temperature of about 425°C (800°F) and no melting point and its heat deflection temperature at 264 psi (1.8 MPa) is about 815°F (435 °C). In addition, PBI have also attracted positive attention because of their high mechanochemical properties and thermal stability. However, after pristine PBI membrane is doped with phosphoric acids (PA), mechanochemical strength of PBI membrane was reduced for the higher the PA content in PBI. And hence, PBI membranes with large amount of acid doping might cause higher acid leaching problem comparing with lower amount of PA doping into PBI membrane in fuel cell applications. To solve these challenges, inorganic composite doped-PBI membranes are of high interest to achieve high tolerance acid leaching problems and enhance the proton conduction paths in PBI matrices [11-15].

Partially alkali metal-substituted heteropoly acids have attracted good attention due to their high catalytic properties with high proton conductivity in many acid-type reactions. Acidic or anhydrous inorganic compounds were mostly used for the performance enhancing

of inorganic solid-state proton conductor. Inorganic solid-state composite materials fabricated via high mechanochemical milling treatment shows a high promising way that improves the proton conductivity of inorganic composite materials and reduces particle and crystalline sizes [16-22]. Hence, the fabrication of inorganic composites have been focused on the many factors of low-cost, high-performance, medium temperature (at around 150 ^{o}C)-resistant for high temperature PEMFCs. Introducing solid acid composite materials (e.g. $CsHSO_4$-$H_4SiW_{12}O_{40}$) into the PBI membrane performs to increase absorption capability of PA and supports to prevent acid leaching of PA at high temperature [23].

In this research work, CHS-WSiA composite materials were synthesized to enhance the anhydrous proton conductivity and decrease the particle sizes via mechanochemical dry and wet milling as inorganic fillers of polymer electrolyte membranes' fabrication for the application of medium temperature fuel cells. For the medium temperature fuel cells (MT-FCs), proton conductivities and cell performances of CHS-WSiA/PBI membranes were improved after adding inorganic fillers into PBI matrix.

4.2 EXPERIMENTAL PROCEDURE

4.2.1 Starting materials

Reagent-grade cesium hydrogen sulfate ($CsHSO_4$, CHS) (Soekawa Chemical Co.Ltd., Japan) and silicotungstic acid ($H_4SiW_{12}O_{40}$, WSiA) (Wako Pure Chemical Industries, Japan) were obtained to fabricate CHS-WSiA composite materials. *N,N*-dimethylacetamide (DMAc, 99.0 vol%, WAKO Pure Chemical Industries, Japan) was also purchased to use as dispersing solvent for precursor materials to fabricate composite materials via wet milling and a casting solvent for electrolyte membrane fabrication. Commercial polybenzimidazole (PBI) (Sato Light Industry; MRS0810H, 10wt% in DMAc) was used as received precursor without further purification.

4.2.2 Synthesis of partially cesium-substituted silicotungstic acid composites

To synthesize 0.5CHS-0.5WSiA dry composite materials, the planetary dry milling was carried out under a dry nitrogen atmosphere using a planetary ball mill (Purverisette 7, Fritsch) with an agate pot (45 mL) and agate balls (10 mm of 10 balls) at 720 rpm and a rotation ratio of 1:1 for 1 h. After dry milling, the composite materials were collected from the mechanochemical milling pot and were heated at 80 ^{o}C in a vacuum oven overnight to obtain dry and fine composite powders. On the other hand, for 0.5CHS-0.5WSiA wet composite materials, *N*,*N*-Dimethylacetamide (DMAc, 5 mL) (Wako; 99 %) was used as solvent/disperse media at 300 rpm for 1 h. After wet milling, the composite precursors were dried at 60 ^{o}C oven overnight to remove hydrated water and DMAc from the composite materials. Then, it was also heated at 80 ^{o}C for 3 h in a vacuum oven to acquire dry and fine composite materials. The detailed explanations of xCHS-(1-x)WSiA composite materials' fabrication via mechanochemical wet milling and dry milling were clearly seen in Chapter II. A schematic diagram for *x*CHS-(1-*x*)WSiA composites produced by wet mechanochemical milling method was shown in Fig. 4.1 [24,25].

4.2.3 Preparation and fabrication of pristine PBI and CHS-WSiA doped-PBI electrolyte membranes

For electrolyte membrane fabrication, DMAc (43.23 g) and polybenzimidazole solution (PBI, MRS0810H) (10wt% of PBI solution, 4.8 g) were used to cast pristine PBI membrane. Before membrane casting, a magnetic stirrer and a sonicator were used to stirr PBI solution at 500 rpm for 1 h and do sonication the PBI solution about 30 min. Then, petri dish (φ = 9.7 cm) was used to cast PBI solution under the casting temperature (60-120 ^{o}C) for 24 h drying condition. Hot-water durability test was also performed for PBI membrane to eliminate residual materials and DMAc solvent from fabricated PBI membrane at 90 ^{o}C for

5 h. Finally, it was dried to eliminate hydrated water from membrane under dry temperature (at 60 ^{o}C) overnight.

Besides, composite doped-PBI membranes were prepared using the same method of fabrication of PBI membrane as comparison. 20 wt% of CHS-WSiA composite materials was added into PBI solution to fabricate CHS-WSiA/PBI membranes under the same fabrication method of pristine PBI membrane, at weight percent (PBI:CHS-WSiA, 5:1 wt%), before casting.

Finally, phosphoric acid (PA) doping of CHS-WSiA/PBI membranes and pristine PBI membrane was performed by immersing into 85 % of PA (Wako) and heated at 60 ^{o}C for desired PA doping levels (PADLs). Prior to conductivity and fuel cell measurement, PA doped membranes were heated at 60 ^{o}C for 1 h to remove excess PA and water. The amount of PA doped in pristine PBI and CHS-WSiA/PBI composite membranes were calculated based on phosphoric acid doping level (PADL), which was calculated using Eq. (4.1),

$$PADL = [(W - W_0) \times 0.85 / M_{PA}] / (W_{PBI} / M_{PBI}) \quad (4.1)$$

Where, W and W_0 are weight of membrane before and after doping with 85 wt% PA; W_{PBI} is the weight of membrane (without CHS-WSiA composites); M_{PA} and M_{PBI} are molecular weight of PA and PBI, respectively.

4.2.4 General characterization

X-ray diffraction ((Ultima IV, RINT 2200, Rigaku) patterns of the mechanochemically synthesized Cs-substituted WSiA composite materials via dry milling and wet milling were evaluated at room temperature (RT).

The morphologies of the CHS-WSiA/PBI membranes and pristine PBI membrane were observed by field emission scanning electron microscopy (FE-SEM; S-4800, Hitachi).

Thermal properties, dehydration temperature, and decomposition temperature of main chain of pristine PBI and CHS-WSiA/PBI membranes were determined by thermogravimetric analysis (TGA) using a Thermo Plus TG 8121 analyzer (Rigaku). The TGA measurements of pristine PBI and CHS-WSiA/PBI membranes were programmed from RT to 900 °C with heating rate 10 °C min^{-1} under air atmosphere.

Changes in the chemical structures of pristine PBI and CHS-WSiA/PBI composite membranes were examined by Fourier Transform Infrared (FT-IR) spectroscopy (3100 FT-IR, Varian) between 400 and 4000 cm^{-1} in transmission mode.

4.2.5 Electrochemical characterization

AC impedance spectroscopy measurement was performed to evaluate temperature-dependent proton conductivities of pristine PBI and CHS-WSiA/PBI membranes over a frequency range of 10^7-1 Hz (Solartron; SI 1260) under dry nitrogen condition. Before conductivity measurement, pristine PBI and CHS-WSiA/PBI electrolyte membranes were kept at 150 ^oC for 1 h under N_2 atmosphere.

For membrane electrode assembly (MEAs), commercially 0.5 mg cm^{-2} of Pt-loaded carbon papers (EC-TP1-060) were used as electrodes. Pt-loaded carbon sheets were prepared the sizes (1 × 1 cm^2) and (1.5 × 1.5 cm^2) for anode and cathode electrodes, respectively. The membranes with PA doping were sandwiched by the Pt-loaded carbon catalysts to set MEAs measurement condition. 100 mL min^{-1} of H_2 and 100 mL min^{-1} of O_2 were used to supply during FC evaluation. Measurement temperature was set at 150 ^oC for single fuel cell test under dry condition [24, 26]. To observe the membrane degradation behaviors in the fuel cell environment, in-situ durability test of the MEA fabricated with pristine PBI and CHS-

WSiA/PBI (20 wt%) membranes was carried out under a constant current density of 200 mA cm^{-2}. During the single-cell testing, H_2 and O_2 were fed to the anode and cathode at 0.1 MPa with the flow rate of 100 and 100 mL min^{-1}, respectively. Gold-plated steel bolts were attached on the graphite blocks as electrical leads. Schematic diagram for 0.5CHS-0.5WSiA composites fabricated via wet mechanochemical milling method and the test cell assembly for conductivity measurement were shown in Fig. 4.1 and Fig. 4.2. Schematic diagram of the Fabrication and application method of CHS-WSiA doped PBI membranes was shown in Fig. 4.3. Photo image of the AUTO PEM-Dry PEFC machine for medium temperature fuel cell evaluation was shown in Fig. 4.4.

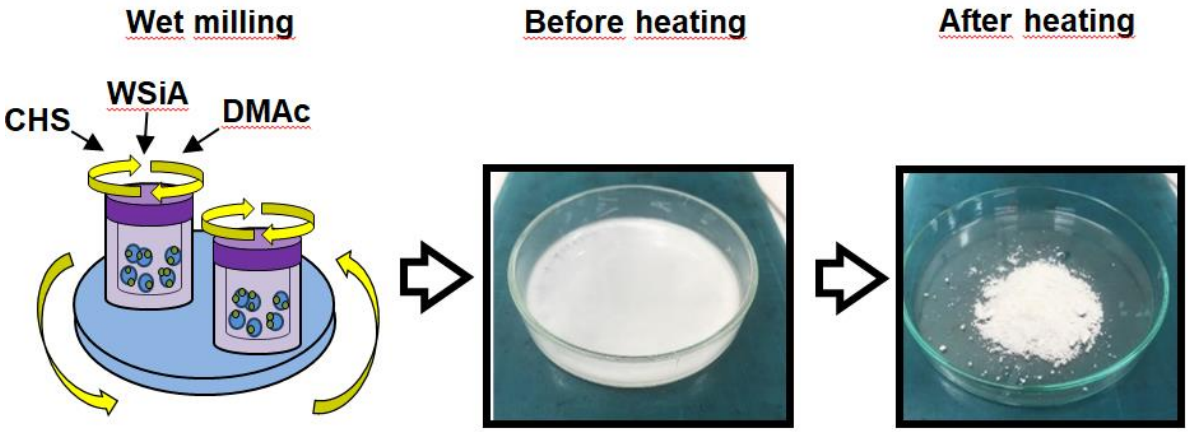

Fig. 4.1. Schematic diagram for 0.5CHS-0.5WSiA composite materials produced by wet mechanochemical milling method.

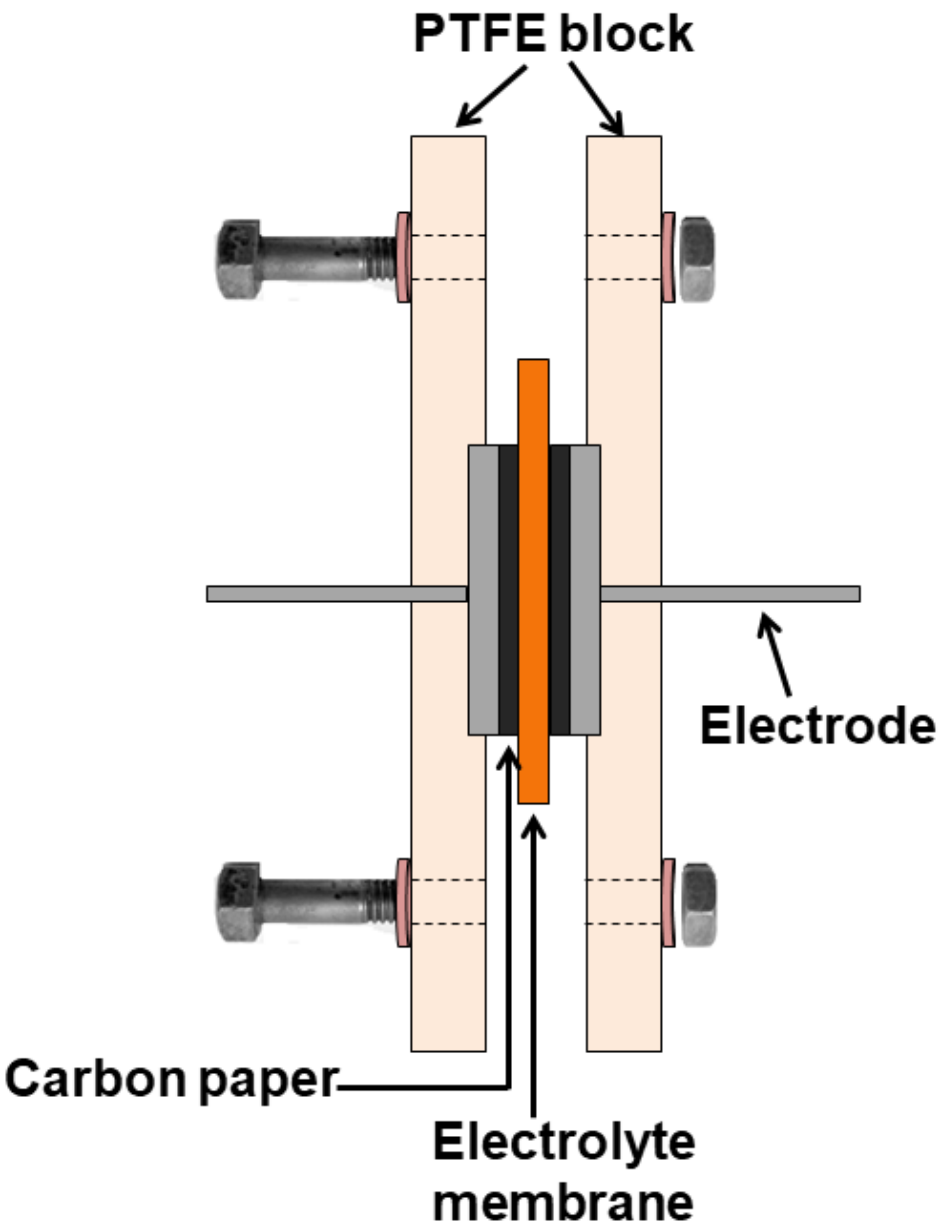

Fig. 4.2. Schematic diagram of the test cell assembly for conductivity measurement.

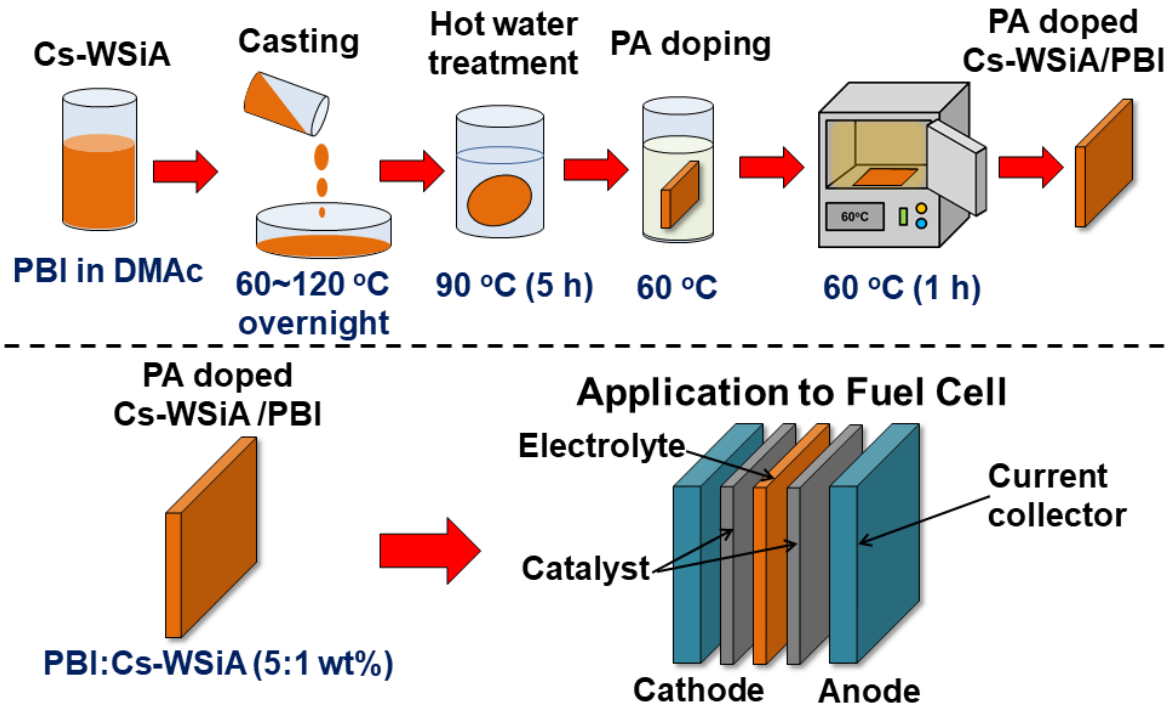

Fig. 4.3. Schematic diagram of the Fabrication and application method of CHS-WSiA doped PBI membranes.

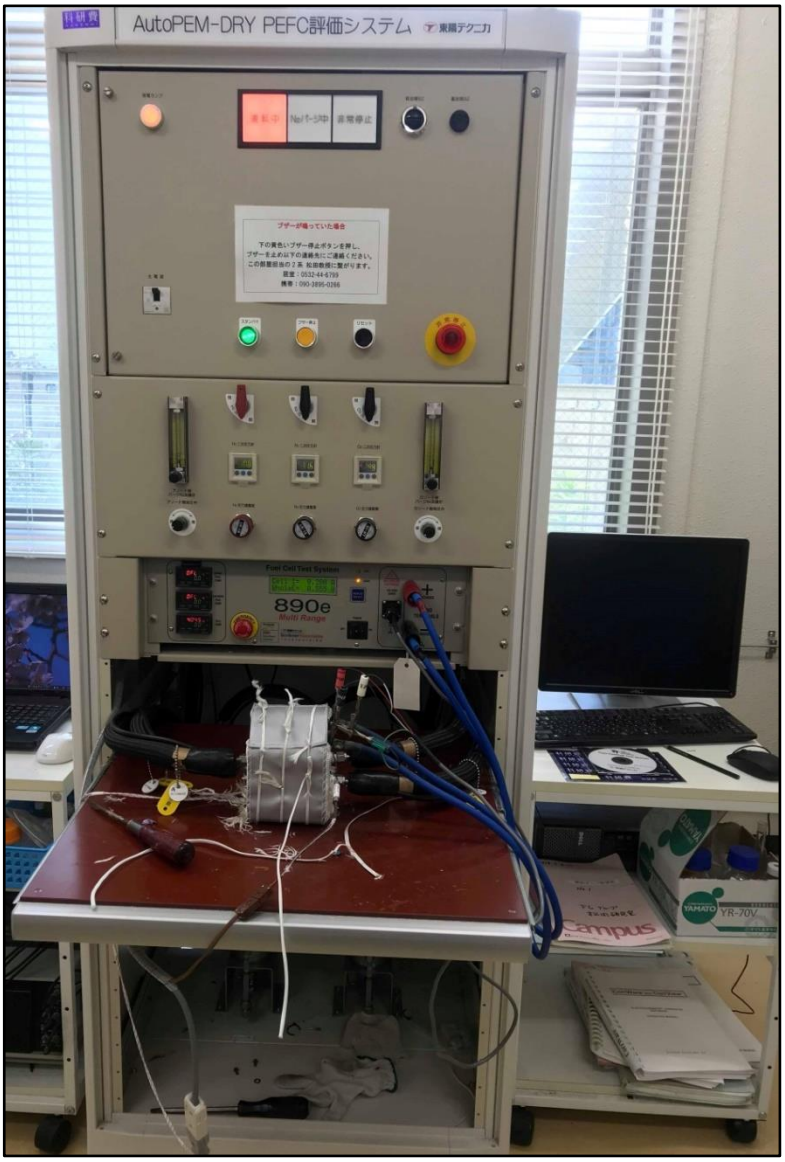

Fig. 4.4. Photo image of the AUTO PEM-Dry PEFC machine for medium temperature fuel cell evaluation.

4.3 RESULTS AND DISCUSSION

4.3.1 Characterization of 0.5CHS-0.5WSiA composites via mechanochemical dry milling and wet milling

From XRD measurement, precursor WSiA, CHS, and 0.5CHS-0.5WSiA composite materials via mechanochemical dry milling and wet milling are shown in Fig. 4.5. Prior to mechanochemical millings, diffraction peaks of CHS and WSiA (in Fig. 4.5) were well matched with standard JCPS library files. After mechanochemical dry milling to fabricate $Cs_xH_{4-x}SiW_{12}O_{40}$, noticeable changes are observed in the XRD results from 25.6 ^{o} to 26 ^{o}; and it showed broad diffraction peak with low crystallinity comparing with composite materials fabricated via mechanochemical wet milling. After mechanochemical wet milling, the diffraction peaks of composite materials with high crystallinity slightly shifted to higher angle; that compared with composite materials via mechanochemical dry milling. Both composite materials fabricated via dry and wet milling revealed the highest intensities of crystalline nature with the high peak shifting to higher angles which specifies that the H^+ ion in WSiA was partially substituted with large Cs^+ ion in CHS to fabricate $Cs_xH_{4-x}SiW_{12}O_{40}$ via mechanochemical dry and wet milling. As the detailed characterizations of CHS-WSiA composite system, it was clearly shown in chapter 2.

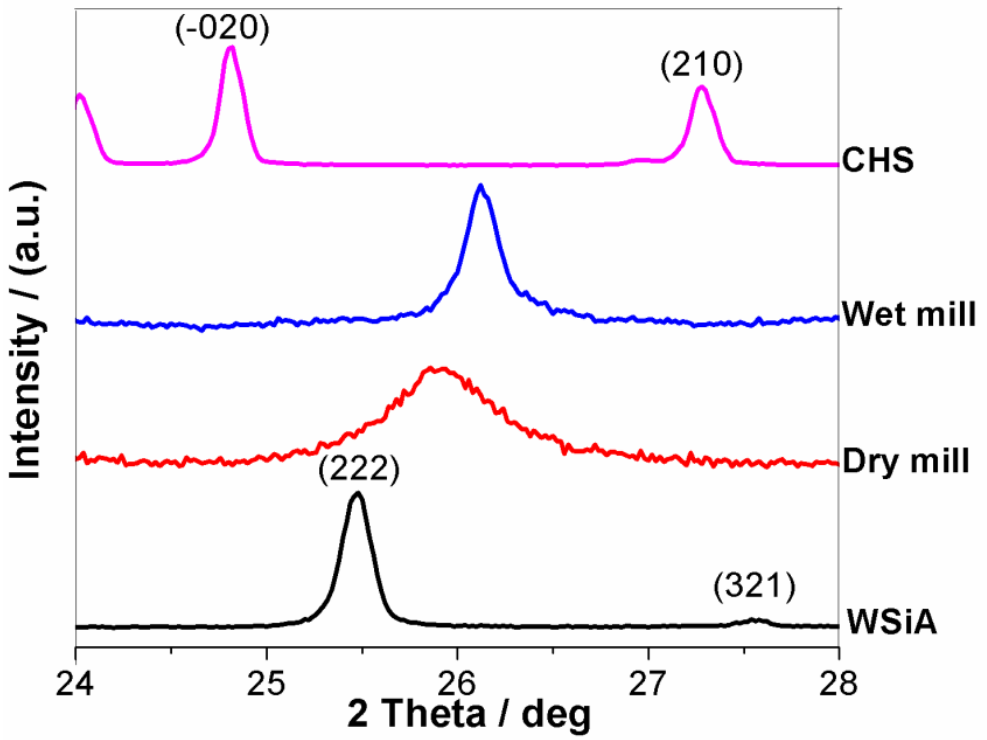

Fig. 4.5. Powder XRD patterns of precursor WSiA, CHS, and 0.5CHS-0.5WSiA composite materials via mechanochemical dry milling and wet milling.

4.3.2 Characterization of CHS-WSiA/PBI and pristine PBI membranes

The chemical structure and peak assignments of ^{1}H-MAS-NMR spectra of pristine PBI (MRS0810H) are shown in Fig. 4.6. The chemical shift at 7.63, 7.78, 7.94, 8.32 and 9.15 ppm are ascribed to H_b, H_d, H_c, H_f and H_e of PBI, respectively.

Different PADL values of CHS-WSiA/PBI and pristine PBI membranes with different doping time were shown in Fig. 4.7. For CHS-WSiA(wet)/PBI electrolyte membrane, after 35 min, PADL value was reached to 4 mol, and 6 mol for 55 min, and then reached to 8 mol during 70 min for FC evaluation. Then, it was slightly increased to be 8 mol over 70 min during PA doping time. 8 mol of PADL was selected to apply for membrane characterization and FC evaluation. On the other hand, after 65 min, 4 mol of PADL was achieved for the CHS-WSiA(dry)/PBI membrane, and 6 mol for 105 min, and then, reached to 8 mol PADL during 150 min. For pristine PBI, it showed 4 mol of PADL within 8 min, and reached to 6 mol during 70 min, and then saturates 8 mol PADL after 85 min. Especially, PA dopants in composite PBI membranes and pristine PBI exist in different forms. For instance, they exist not only chemically reacted PA with nitrogen of imidazole rings in PBI but also physically adsorbed PA in PBI as free acids [10]. CHS-WSiA(wet)/PBI membrane with nonosized-composite materials showed good hygroscopic properties and maintained a large amount of PA after PA doping.

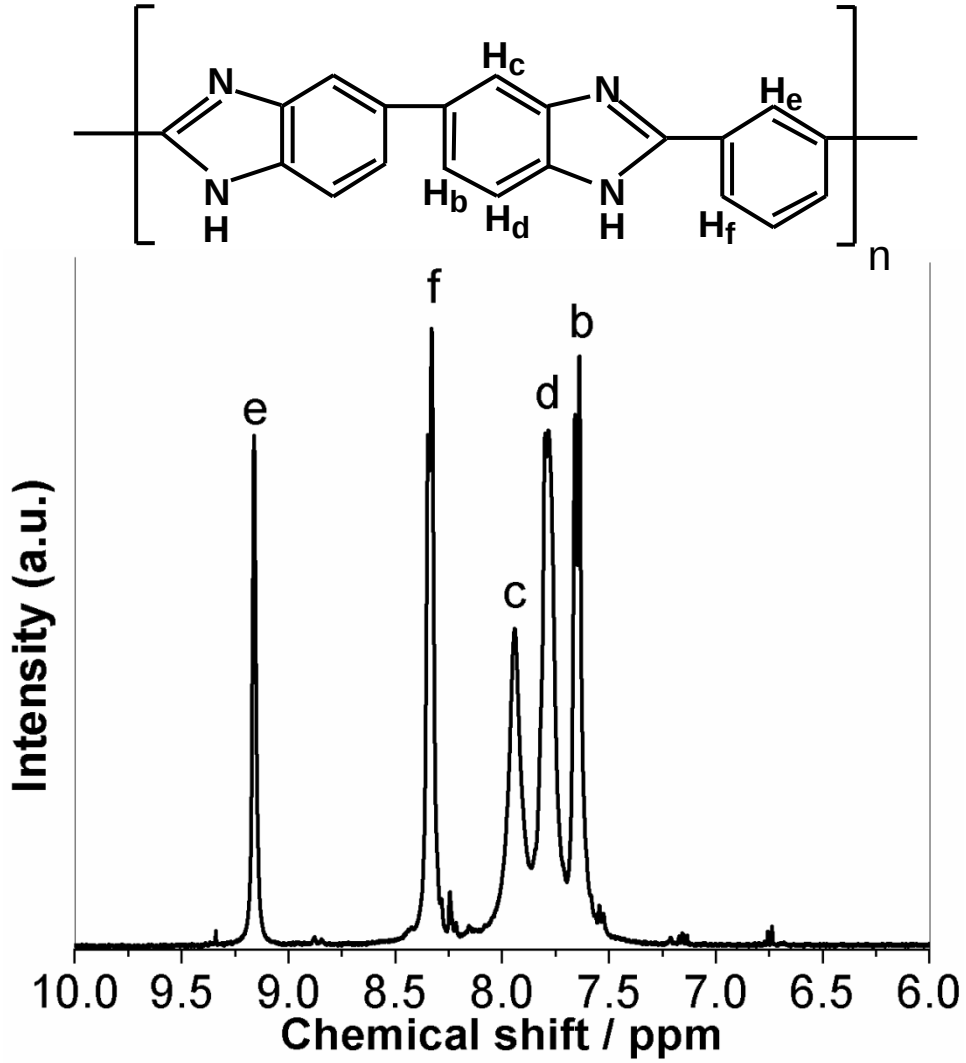

Fig. 4.6. Liquid ^{1}H-MAS-NMR spectrum of PBI in the chemical shift region 10-6 ppm.

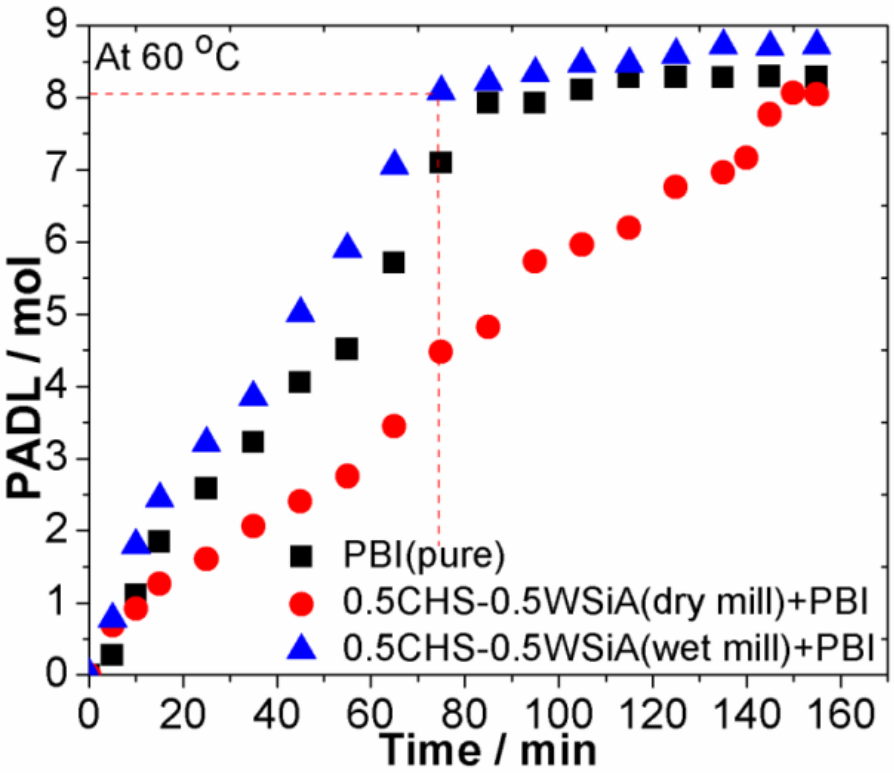

Fig. 4.7. Time-dependent of PADL for pristine PBI, 0.5CHS-0.5WSiA(dry mill)/PBI, and 0.5CHS-0.5WSiA(wet mill) /PBI membranes, respectively.

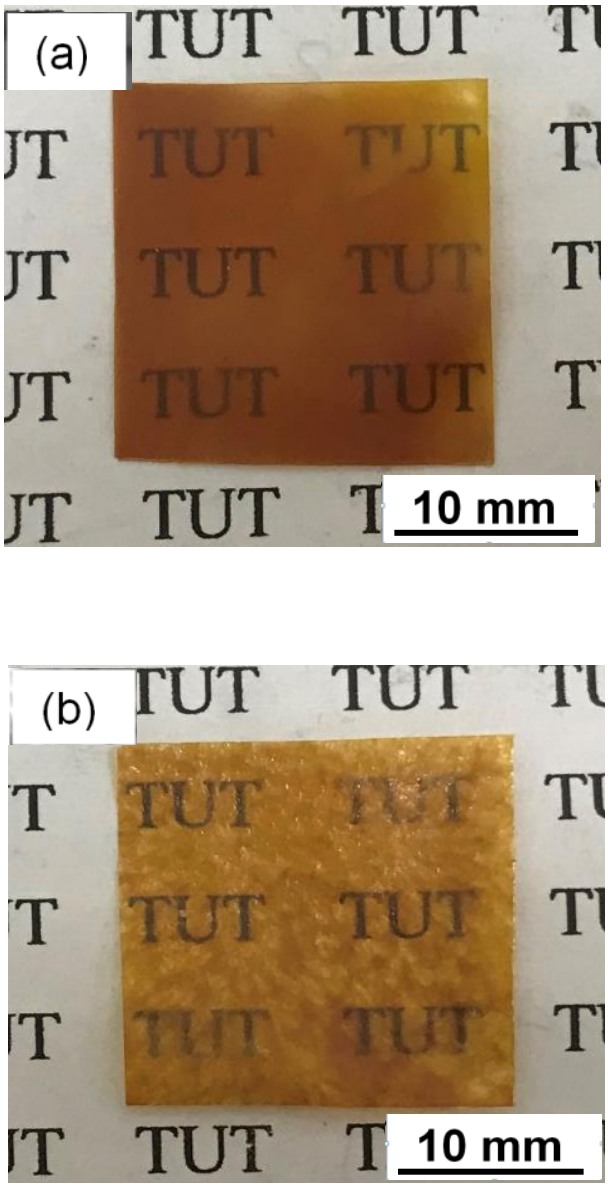

Fig. 4.8. Photographs of (a) 0.5CHS-0.5WSiA (dry mill) /PBI membrane and (b) 0.5CHS-0.5WSiA (wet mill) /PBI composite membranes.

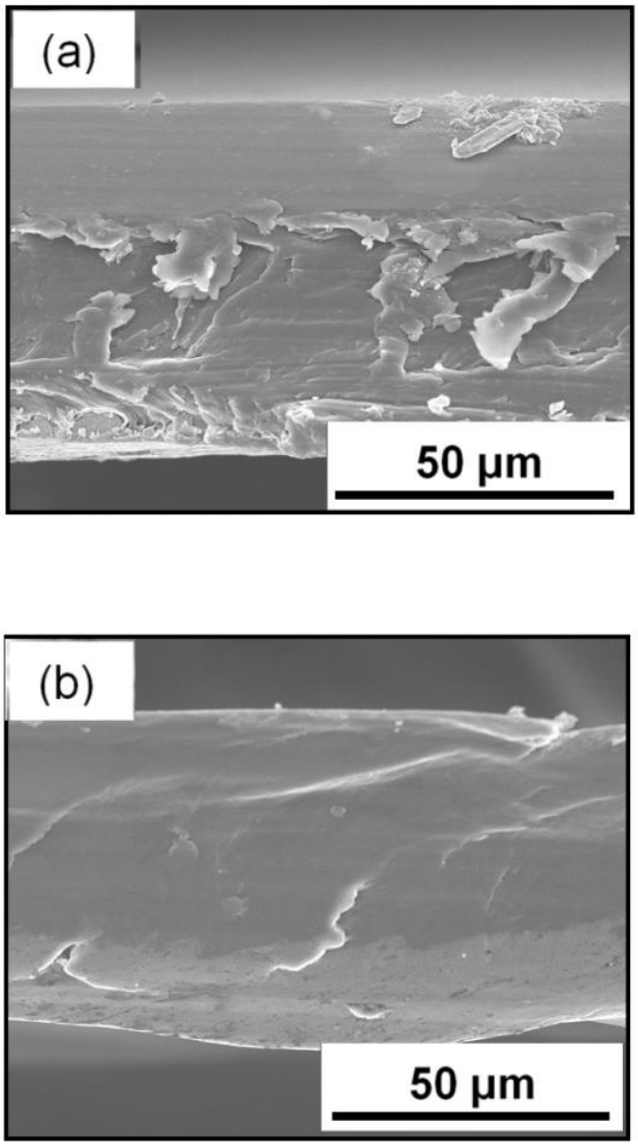

Fig. 4.9. Cross-sectional FE-SEM images of (a) 0.5CHS-0.5WSiA (dry mill)/PBI and (b) 0.5CHS-0.5WSiA(wet mill)/PBI composite membranes.

Photographs of 0.5CHS-0.5WSiA (dry mill) and 0.5CHS-0.5WSiA (wet mill) composite electrolyte membranes are shown in Fig. 4.8. They were seen to be good transparent and homogenous appearances as composite-doped-PBI matrices. FE-SEM morphologies of cross-sectional measurements of the composite membranes were shown in Fig. 4.9 with the typical thickness of 50-70 μm for the composite membranes; and they indicated inorganic composite materials were thoroughly distributed in PBI matrix after fabrication of CHS-WSiA/PBI composite membranes. These observations suggested that the homogeneous and thin membranes with sufficient thickness were convenient to apply for anhydrous conductivity measurements and FC performance evaluation in the medium temperature range (100-200 ^{o}C).

The thermal stabilities of pristine PBI, CHS-WSiA(dry)/PBI, and CHS-WSiA(wet)/PBI composite membranes were evaluated as shown in Fig. 4.10. In the TGA measurement, the pristine sample and CHS-WSiA-doped-PBI membranes indicated first weight loss trend at around 120 ^{o}C, attributed to water structure molecules, and second at around 495-560 ^{o}C, associated with decomposition of the main chain of PBI. Furthermore, weight loss ascribed to the thermal decomposition or evaporation of DMAc in the temperature range from 120 to 180 ^{o}C was not found which means boiling point of DMAc (165 ^{o}C). These results show that the incorporated Cs-HPAs composites with PBI matrix are stable in their composite electrolytes. Pristine PBI, CHS-WPA(dry)/PBI, CHS-WSiA(wet)/PBI composite membranes were thermally stable below 500 ^{o}C, which fulfilled the thermal requirement for medium temperature fuel cells.

Fig. 4.11 shows the FT-IR spectra of pristine PBI, CHS-WSiA(dry)/PBI, CHS-WSiA(wet)/PBI electrolyte membranes, as well as mechanochemically prepared CHS-WSiA composite materials. The FT-IR spectra of the pristine PBI and CHS-WSiA-doped-PBI composite membranes indicated the expected peaks in the 400–2000 cm^{-1} of FTIR

measurement region. Four main characterization peaks of CHS-WSiA composite materials, which were 976 cm^{-1}, 921 cm^{-1}, 883 cm^{-1} and 800 cm^{-1}, were observed and assigned as W=O, Si-O, W-O_c-W (corner-sharing oxygen atoms) and W-O_e-W (edge-sharing oxygen atoms), respectively. Incorporation of CHS-WSiA composites into PBI matrix were confirmed by forming and shifting of peaks of pristine membranes around range 400-2000 cm^{-1}. The characterization peaks of CHS-WSiA composite materials were found in the CHS-WSiA/PBI composite membranes at around 976 cm^{-1}, 921 cm^{-1} and 883 cm^{-1}, which were completely incorporated into PBI matrices to form composite-doped-PBI electrolyte membranes. From these observations, CHS-WSiA composite materials were successfully incorporated with PBI matrices for the further physicochemical and electrochemical characterization.

Anhydrous proton conductivities of pristine PBI and CHS-WSiA/PBI composite electrolyte membranes were measured along the temperature range 50-150 ^oC. Fig. 4.12 indicates the temperature-dependent conductivity measurements of pristine PBI and composite PBI membranes with 8 mol of PADL. The conductivity's trends of all membranes were increasing with increasing the temperature in the range 50 to 150 ^oC. However, CHS-WSiA/PBI electrolyte membranes showed the conductivities larger than that of the pristine PBI. CHS-WSiA (dry)/PBI and CHS-WSiA(wet)/PBI showed the conductivities from 2.79×10^{-4} to 1.104×10^{-3} S cm^{-1} and 1.78×10^{-4} to 1.302×10^{-3} S cm^{-1} when the proton conductivities of pristine PBI was achieved from 2.11×10^{-4} to 8.99×10^{-4} S cm^{-1}. Especially, CHS-WSiA(wet)/PBI membrane exhibited high conductivity above 110 ^oC that compared with CHS-WSiA(dry)/PBI membrane and pristine PBI. These observations recommended that CHS-WSiA composite membranes with nano-scale composite materials maintain acid and water retention properties comparing with pristine PBI membrane for the enhancement of proton conductivity after adsorbing PA.

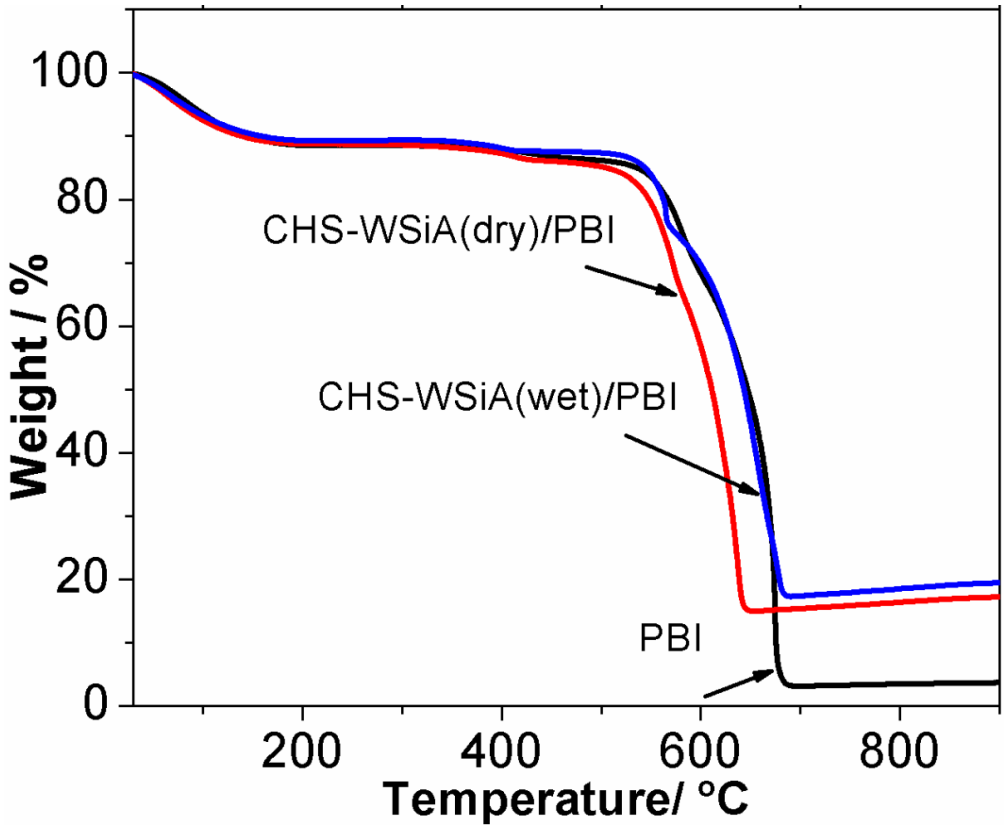

Fig. 4.10. TGA curves of pristine PBI, 0.5CHS-0.5WSiA(dry mill)/PBI, and 0.5CHS-0.5WSiA(wet mill) /PBI membranes, respectively.

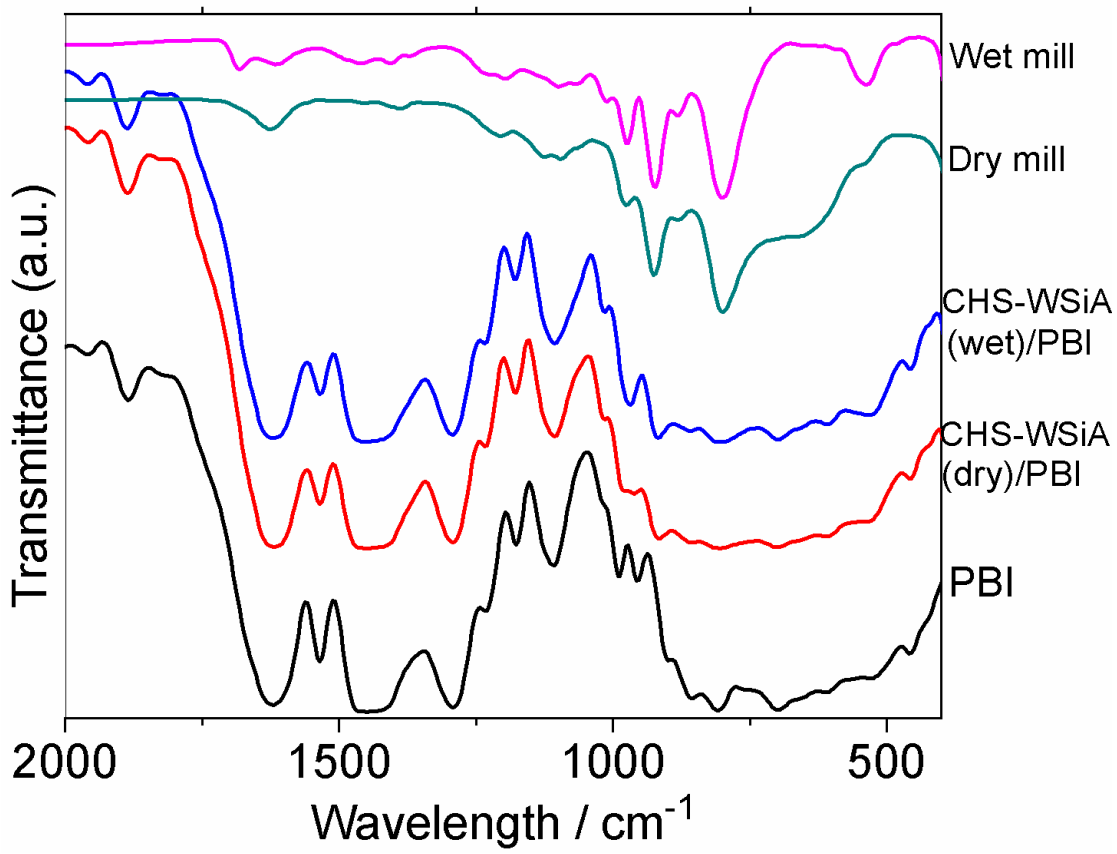

Fig. 4.11. TGA curves of pristine PBI, 0.5CHS-0.5WSiA(dry mill)/PBI, and 0.5CHS-0.5WSiA(wet mill) /PBI membranes, respectively.

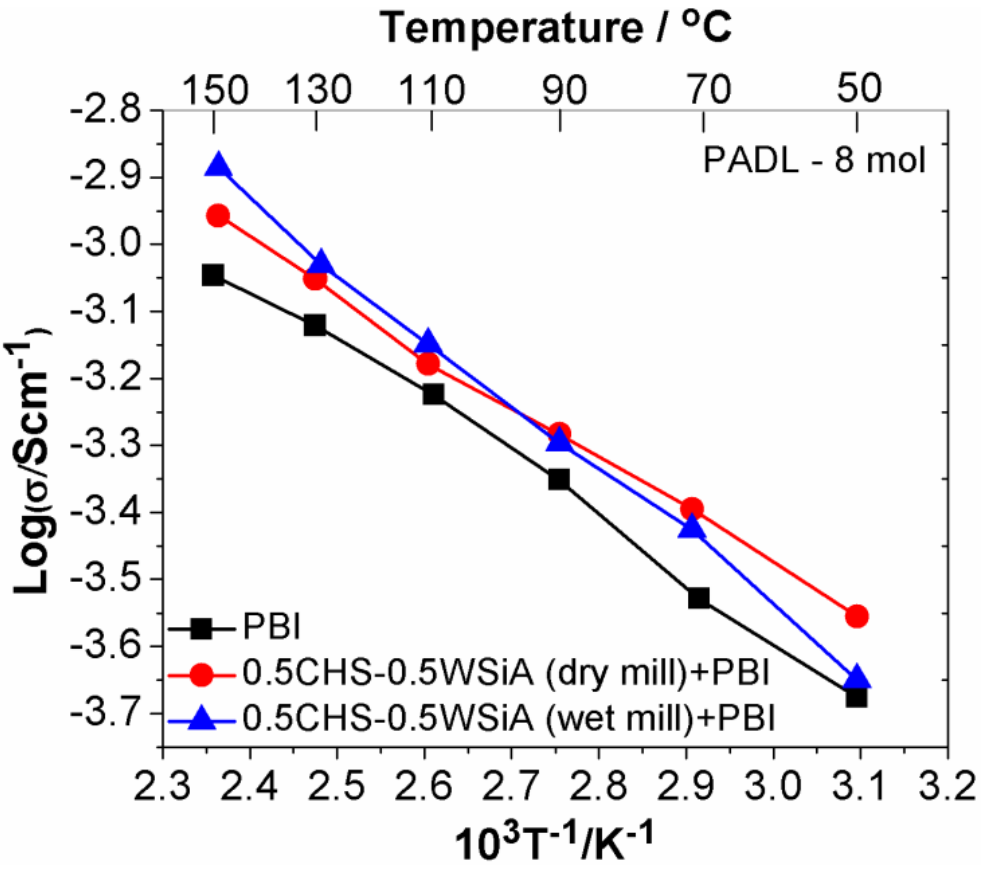

Fig. 4.12. Temperature dependence of conductivity of pristine PBI membrane, 0.5CHS-0.5WSiA (dry mill)/PBI and 0.5CHS-0.5WSiA (wet mill) /PBI composite membranes under anhydrous condition.

The fuel cell evaluation of electrolyte membranes was performed according to their results (shown in Fig. 4.13); with highest power density values of 268, 292, and 378 mW cm^{-2} for pristine PBI, CHS-WSiA(dry)/PBI, and CHS-WSiA(wet)/PBI, respectively. While CHS-WSiA/PBI membranes exhibited the open circuit voltages (> 0.8 V) for low gas permeability, pristine PBI showed the open circuit voltage less than 0.8 V. To make the comparison between CHS-WSiA/PBI membranes and pristine PBI in Fig. 4.13, it can be seen that all the CHS-WSiA/PBI membrane fuel cells indicated good performance compared with pristine PBI. Thus, the CHS-WSiA components in the PBI matrix emphatically adsorbed and retained the PA acid groups in their CHS-WSiA/PBI composite membranes to improve proton conduction mechanism and prevent acid leakage problem.

The current stability test of 20 wt % of CHS-WSiA/PBI composite membranes and pristine PBI was observed to make confirmation of the acid retention properties and thermal stability of the CHS-WSiA composites/PBI matrix (shown in Fig. 4.14). The stability test of composite membranes and pristine PBI was performed as fixed current measurements (0.2 A/cm^{-2}, 24 h). While 20 wt % of CHS-WSiA/PBI composite membranes exhibited constant potential condition throughout the constant current measurement (0.2 A cm^{-2}), the pristine one was observed the degradation of potential after 8 h measurement. These observation of cell performances suggested that inorganic composites partly supported to the PA acid retention of the adsorbed PA ligands via to new proton conduction of CHS-WSiA composites/PBI matrix. Thus, the grain nanostructures of the CHS-WSiA composites with grain nano-sized particles by wet milling in the PBI matrix supported to be homogeneously dispersed in the membrane matrix and also created new proton conduction path after adsorption of PA [26].

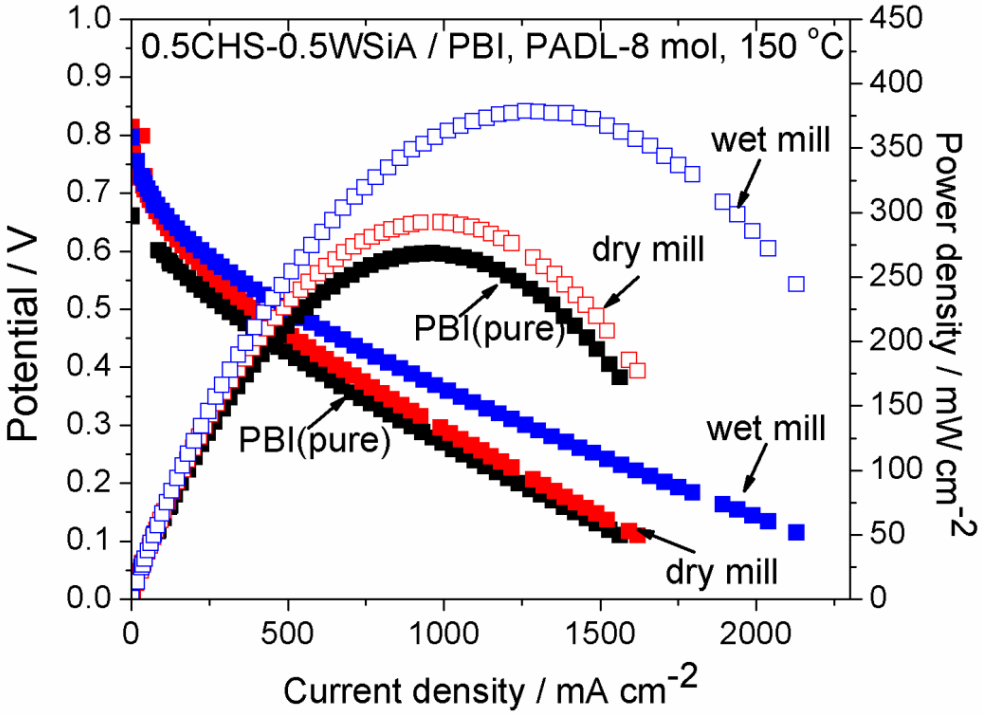

Fig. 4.13. Polarization curve of pristine PBI membrane, 0.5CHS-0.5WSiA (dry mill) /PBI and 0.5CHS-0.5WSiA(wet mill) /PBI composite membranes under anhydrous condition.

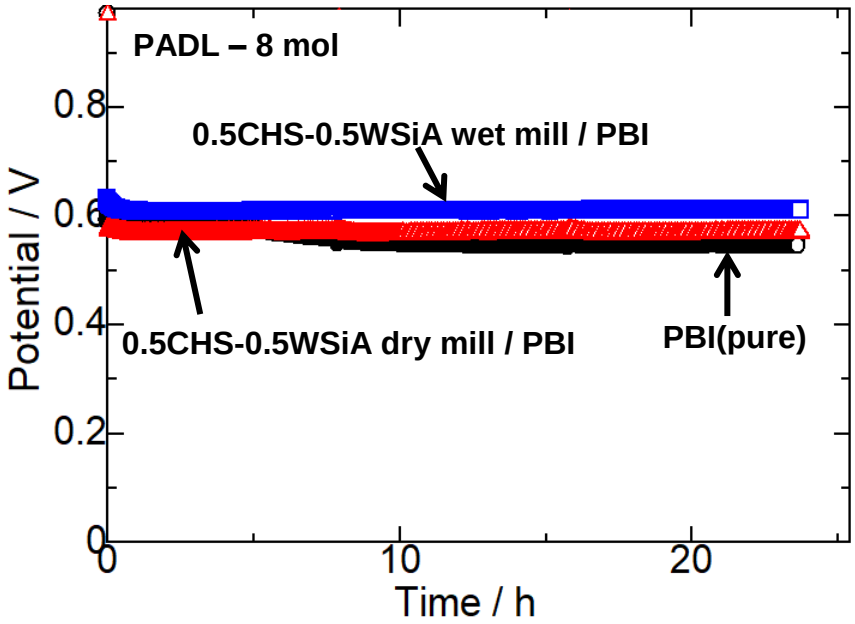

Fig. 4.14. Constant current density measurement of pristine PBI membrane, 0.5CHS-0.5WSiA (dry mill)/PBI and 0.5CHS-0.5WSiA (wet mill)/PBI composite membranes under anhydrous condition.

4.4 CONCLUSIONS

CHS-WSiA composite materials were effectively fabricated via mechanochemical dry milling and wet milling, and characterized their structural properties, thermal properties and chemical properties using XRD, FE-SEM, and proton conductivity measurements. The XRD diffraction peaks of these composite materials shifted to a higher angle via an ion-exchange reaction of the mechanochemical milling effects. The grain sizes (about 25 nm) of CHS-WSiA composite materials obtained by wet milling are smaller than the composite obtained by dry milling. From conductivity measurement, CHS-WSiA composite (wet milling) showed high conductivity of about 10^{-3} S cm^{-1}, compared to the precursor substances at low temperatures. Inorganic-organic CHS-WSiA/PBI membranes were observed for enhanced adsorption and retention properties of PA in the medium temperature (100-200 ^{o}C) fuel cell evaluation via new proton conduction path of CHS-WSiA composites. CHS-WSiA/PBI membranes exhibited higher performances with 378 mW cm^{-2} for CHS-WSiA(wet)/PBI and 292 mW cm^{-2} for CHS-WSiA(dry)/PBI in comparing with 268 mW cm^{-2} of pristine PBI membrane. For constant current test, CHS-WSiA/PBI composite membranes showed stable potential over 24 h measuring period while the potential of pristine PBI was slightly decreased after 8 h. Moreover, CHS-WSiA(wet)/PBI showed fast PA doping and high PA retention ability compared with CHS-WSiA(dry)/PBI and pristine PBI. Addition of inorganic solid acid complex with high proton conductivity into PBI matrix caused fast proton transfer in these composites/PBI electrolyte membranes. Both CHS-WSiA/PBI electrolyte membranes showed proton conductivities higher than pristine PBI. A new proton conduction path was also proposed in these composite membranes due to the inorganic solid composites' effect in the PBI matrix. CHS-WSiA(wet)/PBI showed the highest power density and best durability test with high potential stability among these electrolyte membranes because it

exhibited a stable performance even in a second cycle fuel cell performance measurement by suppressing of PA leaching.

REFERENCES

[1] N. Abdullah, S.K. Kamarudin, J. Power Sources **278** (2015) 109-118.

[2] M. Mizuno, S. Hayashi, Solid State Ionics **167** (2004) 317-323.

[3] O. Barron, H. Su, V. Linkov, B. G. Pollet, S. Pasupathi, J. App. Electrochem. **44** (2014) 1037-1045.

[4] Q. Li, R. He, J. O. Jensen, N. J. Bjerrum, Fuel cells **4** (2004) 147-159.

[5] J. Loboto, P. Cañizares. M.A. Rodrigo, J.J. Linares, J. A. Aguilar, J. Membr. Sci. **306** (2007) 47-55.

[6] A. Matsuda, T. Kanzaki, K. Tadanaga, M. Tatsumisago, T. Minami, Electrochim. Acta **47** (2001) 939-944.

[7] A. Matsuda, T. Kanzaki, K. Tadanaga, M. Tatsumisago, T. Minami, Solid State Ionics **139** (2001) 113-119.

[8] N. Nakamoto, A. Matsuda, K. Tadanaga, T. Minami, M. Tatsumisago, J. Power Sources **138** (2004) 51-55.

[9] K. Tadanaga, H. Yoshida, A. Matsuda, T. Minami, M. Tatsumisago, Electrochim. Acta **50** (2004) 705-708.

[10] Y. Oono, T. Fukuda, A. Sounai, M. Hori, J. Power Sources **195** (2010) 1007-1014.

[11] J. Lablo, P. Cañizares, M. A. Rodrigo, D. Úbeda, F. Javier Pinar, J. Membr. Sci. **369** (2011) 105-111.

[12] F. J. Pinar, P. Cañizares, M. A. Rodrigo, D. Ubeda and J. Lobato, RSC Adv. **2** (2012) 1547-1556.

[13] S. Yuk, D-H. Lee, S. Choi, G. Doo, D. W. Lee, H-Tak. Kim, Electrochim. Acta **270** (2018) 402-408.

[14] J. Halter, S. Thomas, S. K. Kær, T. J. Schmidt, F. N. Büchi. J. Power Sources **399** (2018) 151-156.

[15] D. Ergun, Y. Devrim, N. Bac, I. Eroglu. J. Appl. Polym Sci. **124** (2012) E267-E277.

[16] S-Y. Oh, T. Yoshida, G. Kawamura, H. Muto, M. Sakai, A. Matsuda, J. Mat. Chem. **20** (2010) 6359-6366.

[17] Y. Daiko, H. Takagi, K. Katagiri, H. Muto, M. Sakai, A. Matsuda, Solid State Ionics **179** (2008) 1174-1177.

[18] S. Shanmugam, B. Viswanathan, T.K. Varadarajan, J. Membr. Sci. **275** (2006) 105-109.

[19] S.Y. Oh, T. Yoshida, G. Kawamura, H. Muto, M. Sakai, A. Matsuda, J. Power Sources **195** (2010) 5822-5828.

[20] A. Matsuda, V.H. Nguyen, Y. Daiko, H. Muto, M. Sakai, Solid State Ionics **181** (2010) 180-182.

[21] E. Y. Safronova, A.K. Osipov, A. E. Baranchikov, A.B. Yaroslavtsev, Inorg. Mat. **51** (2015) 1157-1162.

[22] Suryani, Y-L. Liu, J. Membr. Sci. **332** (2009) 121-128.

[23] A. Matsuda, S-Y. Oh, V.H. Nguyen, Y. Daiko, G. Kawamura, H. Muto, Electrochim. Acta **56** (2011) 9364-9369.

[24] J. Mbah, B. Krakow, E. Stefanakos, J. Wolan, Electrochem. Solid St. **12** (2009) E12-E16.

[25] C. Xu, X. Wu, X. Wang, M. Mamlouk, K. Scott, J. Mater. Chem. **21** (2011) 6014-6019.

[26] K. Z. Ya, K. Kumazawa, G. Kawamura, H. Muto, A. Matsuda, J. Ceram. Soc. Jpn. **126** (2018) 789-793.

CHAPTER 5

FABRICATION OF PROTON CONDUCTIVE CESIUM-SUBSTITUTED PHOSPHOTUNGSTIC ACIDS AND COMPOSITE DOPED-POLYBENZIMIDAZOLE AND THEIR APPLICATIONS IN MEDIUM TEMPERATURE FUEL CELLS

5.1 INTRODUCTION

Inorganic-organic proton conductors with high potential efficiencies have been popular as large research attention in numerous electrochemical strategies such as polymer electrolyte fuel cells (PEMFC), lithium batteries, electrolyte sensors, and membrane electrode assembly (MEA), etc [1-4]. Particularly, these solid-state proton conductors exhibited very high conductivities in the medium temperature range (100-200 ^{o}C) for different kinds of electrochemical devices. For the applications of solid-state proton conductors in the PEMFC, they own the potential properties not only as proton conductive electrolytes in polymer membranes but also reduce the Pt catalyst poisoning problem due to carbon monoxide (CO) in the fuel gas during FC measurement at temperature range (100-200 ^{o}C). These solid electrolytes show as chemical and thermal stable superprotonic conductors but they still obligate a vital goal of polymer research in solid state electrochemistry and materials science [5-7].

Non-perfluorinated inomers (non-PFIs) were advanced for the medium temperature fuel cells. Especially, polybenzimidazole (PBI) is not only the good engineering plastic and water insoluble polymer, but also the electronic/ionic insulator. But, phosphoric acid doped-PBI displays high proton conductivity and achieves as the potential candidate in the polymer electrolyte fuel cells (PEMFCs). PA doped-PBI is the best known example which occupied

reasonable electrolyte membrane for fuel cells, with excellent thermo-chemical stability and high conductivity [8-14].

Recently, solid state conductors, alkali sulfates such as $CsHSO_4$ (CHS), $KHSO_4$(KHS), $NaHSO_4$(NHS), $LiHSO_4$(LHS), $RbHSO_4$(RHS) have been widely used as additive inorganic materials for the medium temperature polymer electrolyte fuel cells because they own high proton conductivity under ambient condition. Among alkali solid acids, cesium hydrogen sulfate (CHS) shows the superprotonic phase transition property to achieve very high proton conductivity (~10^{-2} S cm^{-1}) over 140 ^oC by electrochemical impedance spectroscopy (EIS). However, the conductivity of CHS was decreased by 4 orders of magnitude by Haile et al. reported the fuel cell properties of CHS [15] with the superprotonic phase transition. As a weak point of CHS, it shows low conductivity at about 10^{-7} S cm^{-1} range at around 100-120 °C below phase transition temperature (from phase I to phase II), 141 ^oC [16-20]. It is not good appropriate to use as inorganic additive materials in the composite membrane fabrication for medium temperature fuel cells. Matsuda et al. have reported $MHSO_4$-$H_3PW_{12}O_{40}$ (MHS-WPA) composite system using nanocomposite effects via dry mechanochemical milling method to maintain the high conductivity even under superprotonic phase transition of CHS [21]. From their ^{1}H-MAS-NMR measurements, it was revealed that new hydrogen bonding was generated between WPA and Sulfo groups of $CsHSO_4$ to promote the high proton conductivity of composite system. On the one hand, research interest of heteropolyacids (HPAs) has been increased recently which are also good potential conducting materials with high proton conductivity according to their strong acidity and catalytic properties even below ambient temperature and pressure. They are also good inorganic additive modifiers to improve the fuel cell performance membranes due to their high crystalline nature with the properties of high proton conductive and thermally stable materials. But, even though HPAs exhibited good thermal stability, high acidity, and high oxidizing

ability, their chemical stability and water durability are very poor because of their high hygroscopic properties. Consequently, HPAs electrolyte membranes are not directly convenient for fuel cell evaluation due to their high solubility in water and strong influence of humidity on proton conductivity [22-25]. M. J. Janik et al. reported WPA has very low proton conductivity of ~1×10^{-7} S cm^{-1} with activation energy of ~100 kJ/mol [26]. For proton conductive materials research, partially Cs-substituted heteropoly acids fabricated via mechanochemical dry milling showed good attraction because they have not only high catalytic properties but also stable chemical properties of composites with high proton conductivity. A solid-state chemical reaction was employed by high mechanochemical impact treatment using a high-energy ball mill that enhances the proton conductivity of inorganic solid acid-based composites [27, 28]. Especially, Cesium substituted-heteropoly acids (CHS-HPA composites) exhibited strong catalytic activity effect in many acid-type reactions via the mechanochemical milling technique. Hayashi et al., had widely learned hydrogen bonding structures and proton transfer of inorganic solid acid composites by solid state-proton NMR measurement [29-31]. From our recent lab work, anhydrous proton conductive CHS-WPA composites fabricated by dry mechanochemical milling showed high proton conductivities even under ambient condition. Particularly, low CHS mole concentration of these composites is more convenient to apply as inorganic additive chemical in the polymer electrolyte fabrication [32].

In this work, CHS-WPA composite materials with high proton conductivities were synthesized via dry milling and wet milling. Especially, the affect and influence of DMAc solvent on CHS-WPA composites via wet milling was clearly seen to achieve very high proton conductivities in their composite materials comparing with mechanochemical dry milling. These inorganic composite materials using dispersion agent/solvent (DMAc) have been achieved good chemical and thermal stabilities, and high proton conductivity under dry

nitrogen condition. From our main intention, it is the correlative between conductivities and hydrogen bonding formation of CHS-WPA composites with high proton conductivity from ^{1}H-MAS-NMR and EIS measurements. Thus, CHS-WPA composites with high proton conductivity were applied as inorganic additive materials in the membrane fabrication for MT-PEMFC evaluation.

5.2 EXPERIMENTAL PROCEDURE

5.2.1 Starting materials

Reagent-grade Cesium hydrogen sulfate ($CsHSO_4$, CHS from Soekawa's Pure Chemicals) and Phosphotungstic acid ($H_3PW_{12}O_{40}.nH_2O$, WPA from Wako Pure Chemical Industries, Japan) were purchased to fabricate CHS-WPA composite materials. Especially, commercially available *N, N*-dimethylacetamide (DMAc, 99.0 vol%, WAKO Pure Chemical Industries) was also purchased to use as dispersing solvent with precursor materials for wet milling and casting agent for electrolyte membrane production. Agate was selected as the material for the milling pot and milling balls. Polybenzimidazole (PBI) (Sato Light Industry; MRS0810H, 10wt% in DMAc) was used as received without any purification.

5.2.2 Mechanochemical dry and wet milling

The mechanochemical synthesis was carried out in dry nitrogen atmosphere using a planetary ball mill (Pulverisette 7, Fritsch) with an agate pot and balls. The dry milling and wet milling (with DMAc) were successfully performed to fabricate high proton conductive composite materials according to the experimental procedures. Initially, before fabrication of composites, $WPA.nH_2O$ was dried in a vacuum oven (60 ^{o}C) at about a day to eliminate the physisorbed water and reduce until WPA with 6 hydrates. Dry milling was performed in a dry nitrogen atmosphere using a mechanochemical mill system (Purverisette 7, Fritsch) with an agate pot (45 mL of volume) and 10 agate balls with diameter (10 mm). The rotation speed

(720 rpm) with a constant rotation ratio (1:1) was used for dry milling during 1 h milling period. The sample weight and constant molar ratio of *x*CHS-(1-*x*)WPA composite materials were fixed at 2.0 g and 0.5. After dry milling, CHS-WPA composites were collected and heated at 80 ^{o}C in a vacuum oven overnight [23]. On the one hand, for mechanochemical wet milling, same experimental procedure was used as same dry milling process but DMAc solvent (5 mL) was added into milling pot as a collision agent to disperse with precursor chemicals. The rotation speed of wet milling process was fixed at 300 rpm with same constant rotation ratio of dry milling. After wet milling, the samples were transferred into the petri dish and dried at 60 ^{o}C in an oven to remove hydrated water and DMAc solvent from the composites overnight and further dried at 80 ^{o}C for 3 h in a vacuum oven.

5.2.3 Preparation of pristine PBI and CHS-WPA doped-PBI electrolyte membranes

For the fabrication of electrolyte membrane, pristine PBI and CHS-WPA doped-PBI membranes were prepared using the same method of electrolyte membrane fabrication (shown in Chapter 4). 10 wt% of CHS-WPA composite materials were added into PBI solution to fabricate CHS-WPA/PBI membranes under the same fabrication method of pristine PBI membrane before casting. The thorough experimental process of membranes' fabrication was already clarified in Chapter 4.

Finally, PA doping of CHS-WPA/PBI membranes and pristine PBI membrane was achieved by dipping into 85 % of PA (Wako) and heated at 60 ^{o}C for wanted PA doping levels (PADLs). Prior to conductivity and fuel cell measurements, PA doped membranes were heated at 60 ^{o}C for 1 h to eliminate excess PA and water.

5.2.4 General characterization

X-ray diffraction (XRD; RINT 2200, Rigaku,) patterns of the mechanochemically fabricated precursor samples and prepared CHS-WPA composites were evaluated to

determine the structural properties and crystalline sizes using a Rigaku RINT 2200 with Cu Kα radiation source (at 40kV and 40 mA).

Thermogravimetry-differential thermal analysis (TG-DTA) was carried out to determine thermostability, phase-transition, and dehydration temperature of the precursor materials and prepared CHS-WPA composites using Thermo Plus TG 8121, Rigaku. The TGA and DTA measurement conditions of composite materials were programmed from RT to 500 ^{o}C at a rate of 10 ^{o}C min^{-1} under air flow.

Raman (FT-Raman; NRS-3100, Jasco) spectra of CHS-WPA composite materials were measured using a concave glass substrate, ranged between 4000 cm^{-1} and 400 cm^{-1} with a laser wavelength of 532 nm.

The morphologies of the CHS-WPA composite materials were observed using field emission scanning electron microscopy (FE-SEM; S-4800, Hitachi). Prior to FE-SEM measurement, the composite samples were put on carbon substrates and dried in a vacuum oven at 60 ^{o}C overnight and then sputtered using the Pt/Pd method to get electrical conduction under vacuum before FE-SEM observations.

The solid-state proton magic-angle-spinning nuclear magnetic resonance (^{1}H-MAS-NMR, Advance III 400, Bruker) was performed at room temperature using the typical single pulse sequence with the spinning rate (5 kHz) according to Tetramethylsilane (TMS) position. Before measurement, powder samples were dried at 110 ^{o}C under vacuum for 5 h to avoid moisture, and then packed into a MAS rotor in a dry nitrogen atmosphere.

5.2.5 Electrochemical characterization

Proton conductivities of precursor materials, CHS-WPA composite materials, and CHS-WPA doped PBI membranes were evaluated using AC impedance spectroscopy

measurement over a frequency range of 10^7-1 Hz (Solartron; SI 1260) under dry nitrogen condition. The pelletized samples (13 mm in diameter) were prepared with carbon papers on each side of composites by pressing at a loading pressure of 60 MPa for 10 min. The proton conductivities (σ), of the composite samples (between 170 ^oC and 50 ^oC) and composite electrolyte membranes (between 150 ^oC and 50 ^oC) were evaluated from the impedance data using the following equation,

$$\sigma = d / (RS) \quad (5.1)$$

Where, d and S are the thickness and face area of the sample, respectively. Prior to conductivity measurements, composite samples and electrolyte membranes were kept at 170 ^oC and 150 ^oC for 1 h under N_2 atmosphere, respectively. For membrane electrode assemblies (MEAs), commercially 0.5 mg cm^{-2} Pt-loaded carbon papers were used as electrodes. Pt-loaded carbon sheets were prepared the sizes (1 × 1 cm^2) and (1.5 × 1.5 cm^2) for anode and cathode, respectively.

The membranes with PA doping were sandwiched by the Pt-loaded carbon catalysts to set MEAs measurement condition. 100 mL min^{-1} of H_2 and 100 mL min^{-1} of O_2 were applied to supply during FC evaluation. Operating temperature was selected at 150 ^oC and 160 ^oC for single fuel cell test under dry condition [24, 26]. To characterize the membrane degradation behaviors in the fuel cell environment, in-situ durability test of the MEA fabricated with CHS-WPA(dry)/PBI and CHS-WPA(wet)/PBI with 10 wt% of composites was carried out under a constant current density of 200 mA cm^{-2}. During the single-cell testing, H_2 and O_2 were fed to the anode and cathode at 0.1 MPa with the flow rate of 100 and 100 mL min^{-1}, respectively.

Mechanochemical ball milling machine

(1) 300 rpm for wet milling

(2) 720 rpm for dry milling

(3) vacuum condition with Nitrogen

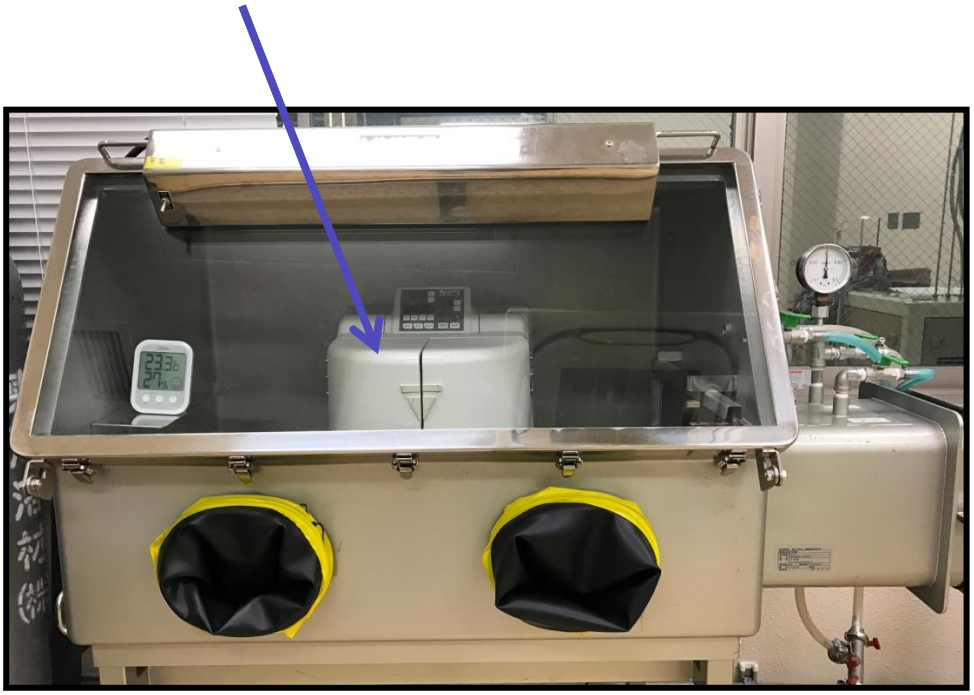

Fig. 5.1. Photo image of mechanochemical ball milling machine (Pulverisette 7, Fritsch).

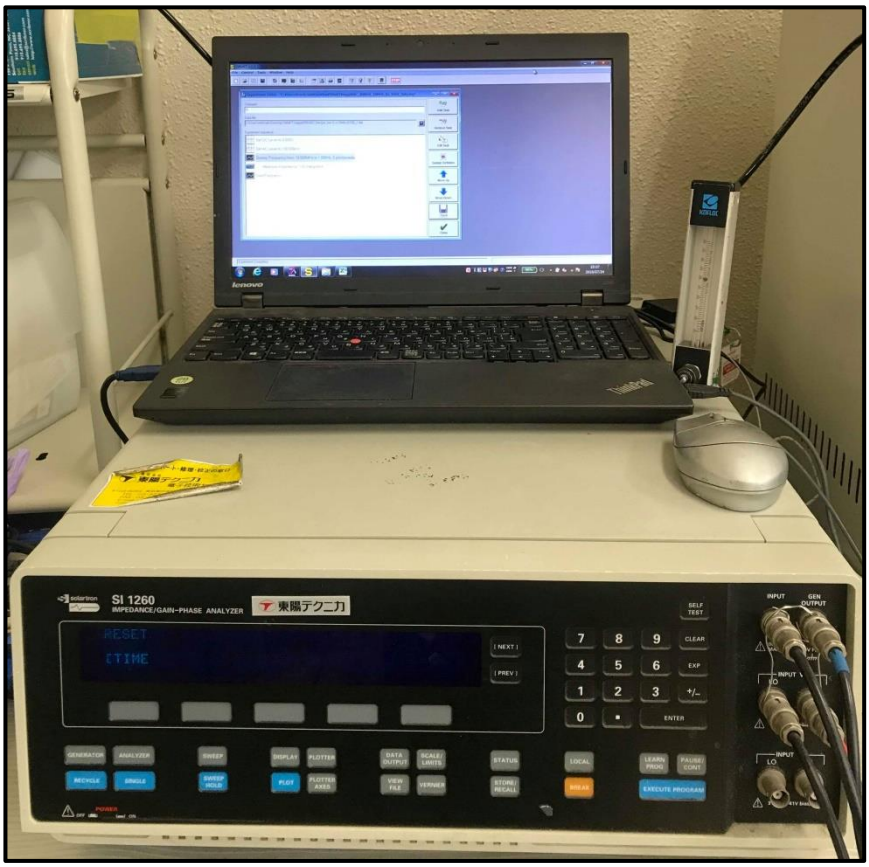

Fig. 5.2. Photo image of electrochemical impedance analyzer (Solartron; SI 1260).

5.3 RESULTS AND DISCUSSION

5.3.1 Structural analysis of CHS-WPA composite materials

Prior to the fabrication of composites, XRD diffraction patterns of precursor materials (WPA and CHS) were completely matched with the standard JCPDS library file (using MDI Jade 6 software). The XRD diffraction patterns showed the diffraction planes, (310), (222), (321) for WPA, and (111), (012), (-202), (210) for CHS, respectively (in Fig. 5.3). After CHS was just mixed with WPA without any treatments, there is no change for this sample, and the XRD diffraction patterns of mixed precursors were matched with precursors' diffraction patterns. After the composite fabrication, the main diffraction peaks of all CHS-WPA composite materials shifted to large angles because ion-substitution reaction (H^+ ion in WSiA and Cs^+ ion in CHS) occurred between CHS and WPA was formed for the formation of new composite materials via mechanochemical dry milling and wet milling. These shifted diffraction peaks were related with precursor WPA because of ion-exchange reaction of precursor materials. The interplanar spacing (d) for the CHS-WPA composite was calculated using the Bragg's equation of $2d\sin\theta = \lambda$, where θ and λ are the diffraction angle and wavelength of Cu Kα (1.5406 Å), respectively. The d-spacings of composites were decreased and found at about 0.3437 nm and 0.3427 nm for composites via mechanochemical dry milling and wet milling according to the peaks shifted to the large angle side. The crystalline sizes of CHS-WPA composite materials were at about 20-25 nm. The CHS-WPA composite materials fabricated via mechanochemical wet milling showed much higher crystalline nature compared with mechanochemical dry milling with broad diffraction patterns with low crystallinity. In this case, DMAc solvent also partially supported to have a strong chemical reaction between dispersed precursor samples during mechanochemical wet milling.

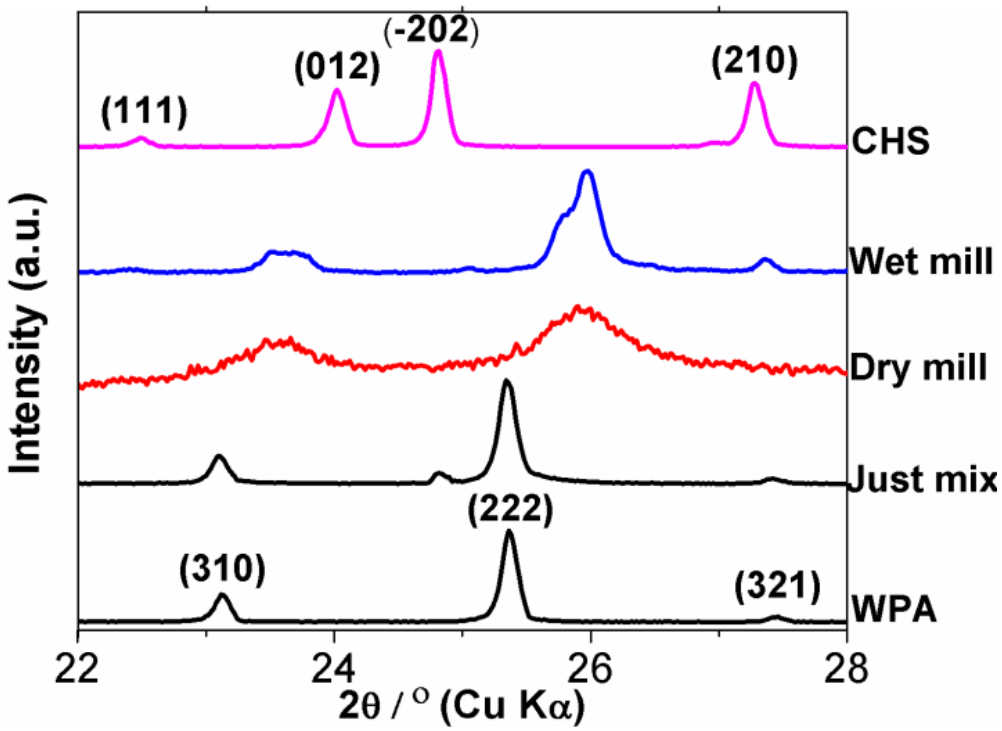

Fig. 5.3. Powder XRD diffraction patterns of WPA, CHS, and prepared CHS-WPA composite materials fabricated by mechanochemical dry milling and wet milling.

Thermal properties of CHS-WPA composite materials fabricated via mechanochemical dry milling and wet milling were evaluated by TG-DTA (shown in Fig. 5.4). According to the TGA curve, precursor CHS and WPA exhibited each one weight loss trend, which started at around 205 ^{o}C, and 153 ^{o}C corresponding to the thermal decomposition of sulfate in CHS and dehydration of hydrated water of WPA. After fabrication of CHS-WPA composite materials via dry milling, it exhibited the weight loss trend at around 100-120 ^{o}C which were attributed to dehydration of hydrated water. On the one hand, for the composite materials via wet milling, fabricated composite materials showed weight loss trend, which started around 200 ^{o}C and was attributed to a part of decomposition of sulfate group in CHS after dehydration of hydrated water. The weight loss percentage of CHS-WPA composites fabricated via mechanochemical wet milling was higher than the composite of CHS-WPA composite fabricated via dry mechanochemical milling because a part of physisorbed water and DMAc solvent still remained in the composites.

From DTA (in Fig. 5.5), the distinct endothermic peaks of precursor samples were observed at around 141 ^{o}C and 205 ^{o}C for CHS which were ascribed to the phase transition and thermal decomposition of sulfate in CHS, and at around 150 ^{o}C for WPA which was corresponded to dehydration of hydrated water in WPA, respectively. All CHS-WPA composite materials exhibited no phase transition after fabrication of composites. The broad endothermic peak of WPA at around 150 ^{o}C was analogous with the TGA data. For CHS-WPA composite materials via dry milling, the appreciable peaks were not found in the DTA curve. However, the appreciable peak of CHS-WPA composite materials fabricated via mechanochemical wet milling was observed at around 150 ^{o}C which attributed to dehydration of WPA. Thus, the phase transition of CHS was successfully retained in these composite materials fabricated using CHS and WPA. DTA results of the CHS-WPA composites were clearly different from precursor materials.

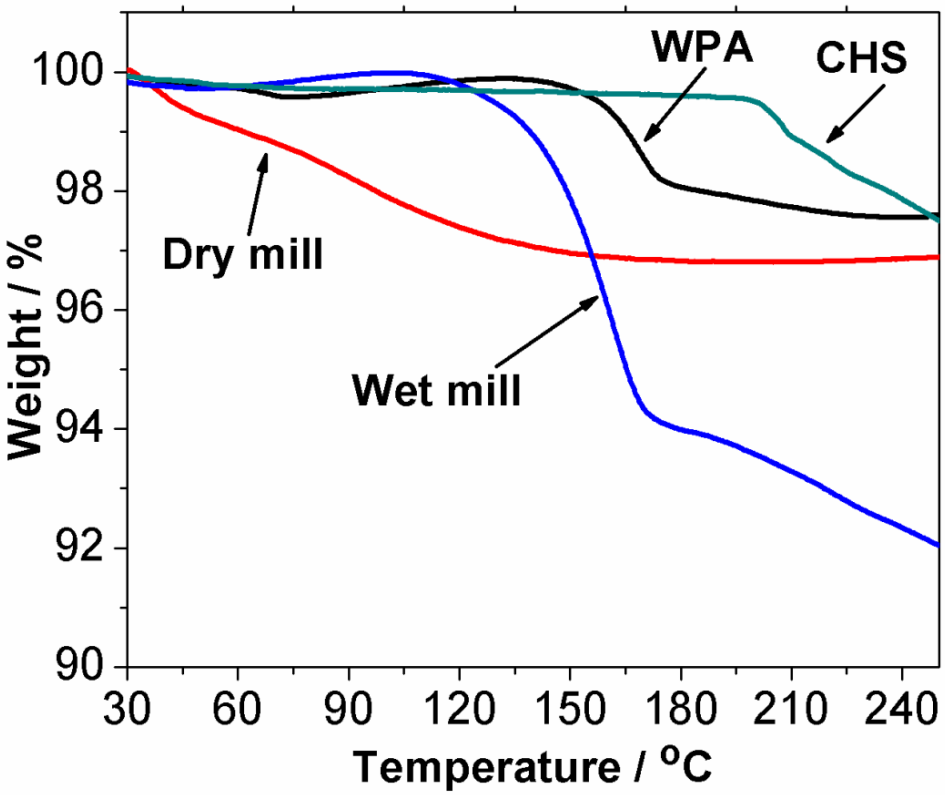

Fig. 5.4. TGA curves of precursor WPA, CHS, and prepared CHS-WPA composite materials fabricated by mechanochemical dry milling and wet milling.

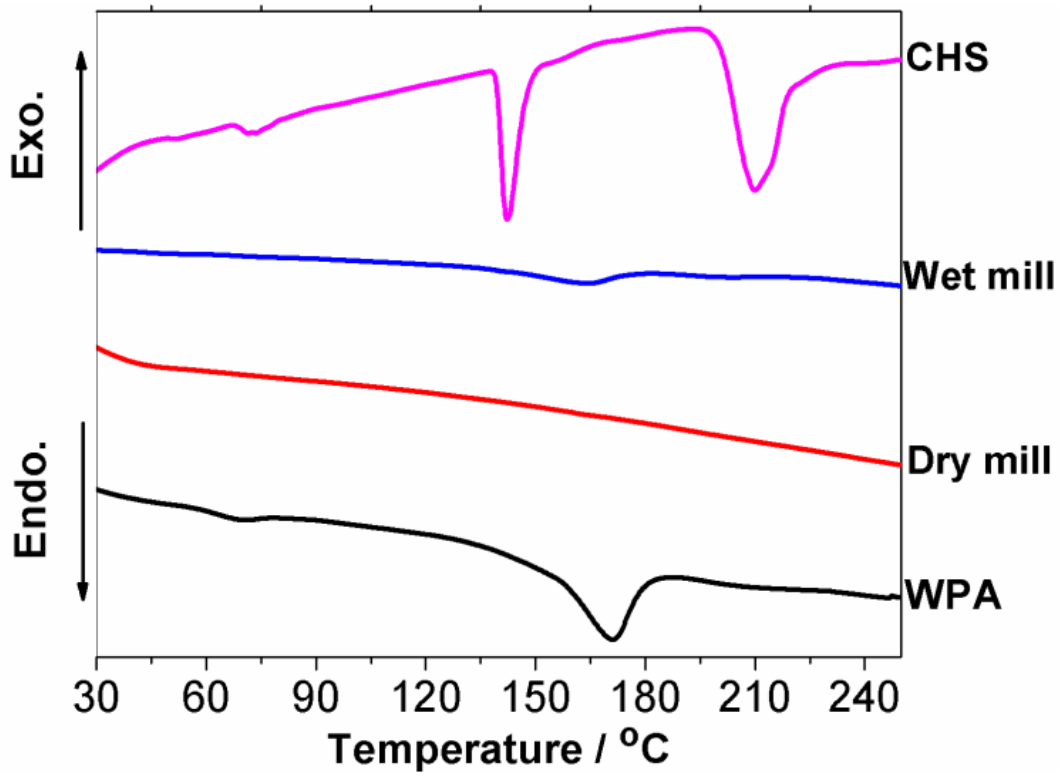

Fig. 5.5. DTA curves of precursor WPA, CHS, and prepared CHS-WPA composite materials fabricated by mechanochemical dry milling and wet milling.

From Fig. 5.6, the FT-Raman bands for the asymmetric and symmetric stretching modes of $W=O_d$ are clearly observed at around 998, and 974 cm^{-1} respectively, for the WPA. The main intend band at 996 cm^{-1} in the spectrum for CHS was attributed to chain S-O bond in SO_4^{2-} of CHS. After dry milling, intend band of CHS-WPA was shifted to higher frequency from precursor material WPA. For mechanochemical wet milling, the $W=O_d$ bonds of WPA largely shifted to high frequency compared with CHS-WPA (dry milling) and precursor materials. These observations of fabricated composite samples with strong $W=O_d$ proved that high chemical interaction was occurred between CHS and WPA and implied the change of chemical state, especially on the surrounding of WPA. The changes of $W=O_d$ bonds probably occurred due to a newly developed hydrogen bond between outermost of partially Cs-substituted WPA and HSO_4^-, thus, shifted $W=O_d$ bonds shorten by attraction of HSO_4^-. Thus, these findings indicated that the mechanochemical wet milling created very high chemical interaction between CHS and WPA to form the CHS-WPA composite materials with anhydrous proton conductivity. It was also expected that the ion-exchange reaction between H^+ ions in WPA and Cs^+ ions in CHS will improve proton conductivity of composite materials.

5.3.2 FESEM images of CHS-WPA composite materials

FE-SEM images of CHS-WPA composite materials fabricated via mechanochemical dry milling and wet milling are shown in Fig. 5.7 (a) and 5.7 (b). Fabricated CHS-WPA composite materials via wet milling showed more homogeneous surface structure and good distribution in their composite materials compared with CHS-WPA composite materials via dry milling. These observations implied that fabricated CHS-WPA composite materials using DMAc solvent showed the new formation of stronger chemical reaction and more compact with less agglomeration than CHS-WPA dry composites because DMAc helps during mechanochemical milling process as a good dispersion medium to occur easily high chemical

reaction between CHS and WPA and supported the formation of new high superprotonic conduction path within these composite materials.

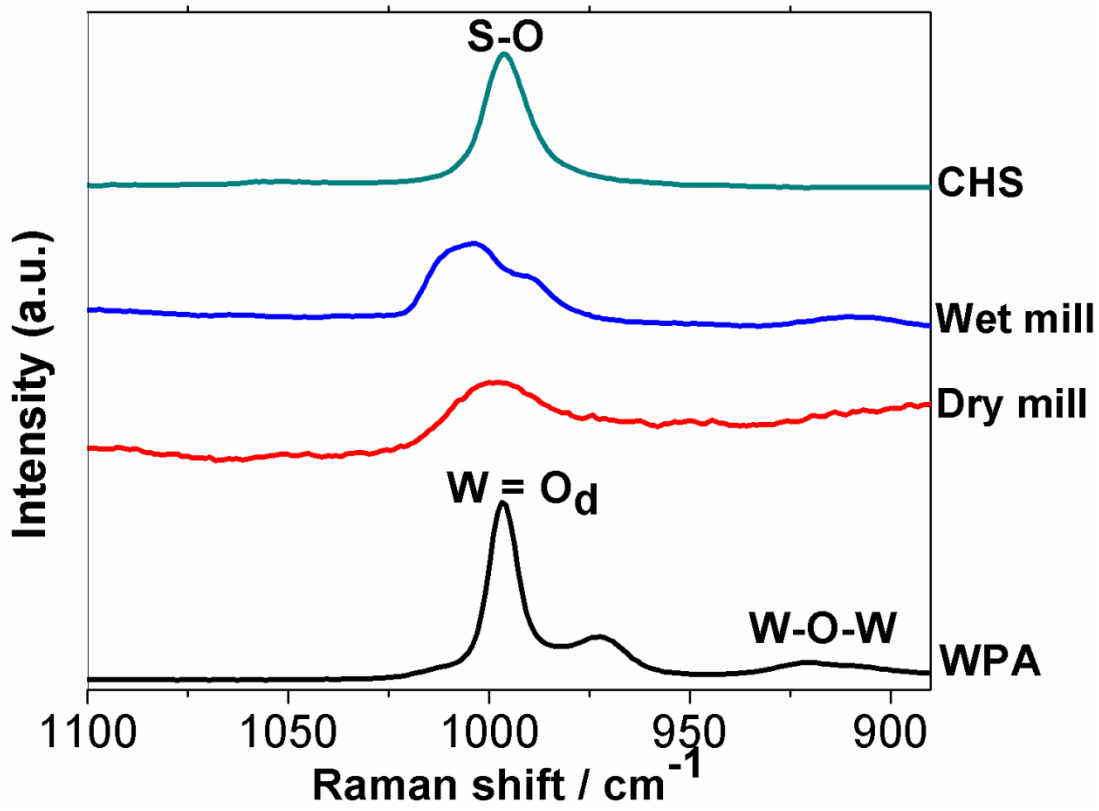

Fig. 5.6. FT-Raman spectra of precursor WPA, CHS, and prepared CHS-WPA composite materials fabricated by mechanochemical dry milling and wet milling.

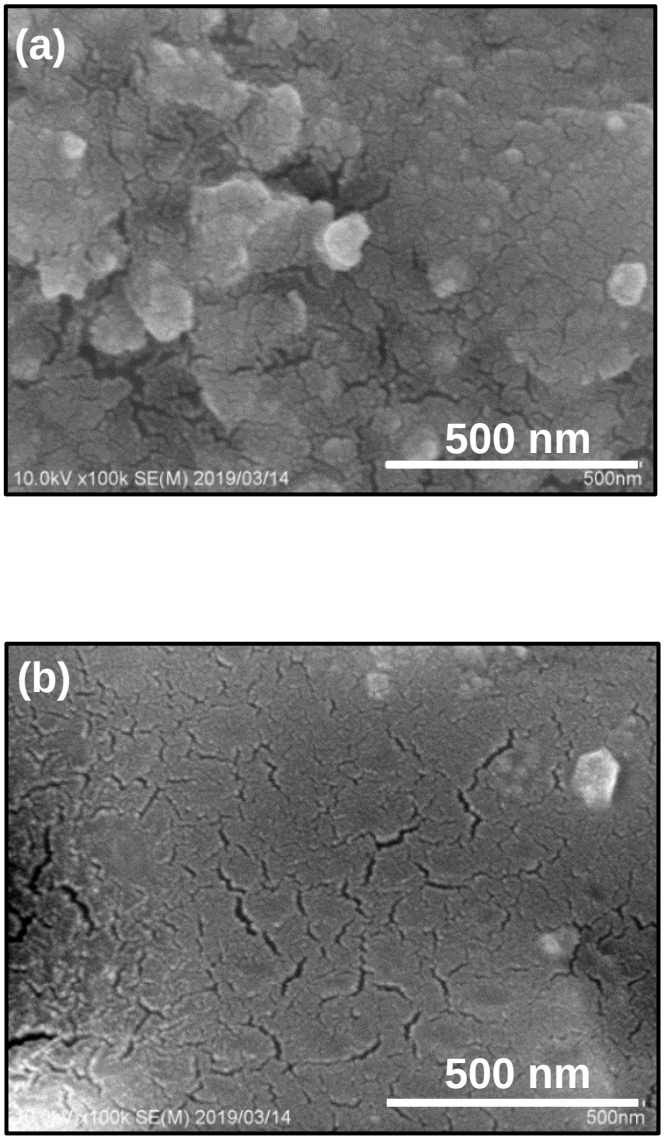

Fig. 5.7. FESEM images of CHS-WPA composite materials (x = 0.5) produced by (a) dry milling and (b) wet milling.

5.3.3 Proton conductivity measurement of CHS-WPA composite materials

As expected from the results of TG-DTA, XRD, FT-Raman measurements, and ^{1}H-MAS-NMR, the CHS-WPA composite materials fabricated via wet milling showed high proton conductivities in a wide temperature from 170 to 50 ^{o}C, while the proton conductivity of pure $CsHSO_4$ dropped abruptly at around 141 ^{o}C due to the phase transition from tetragonal (phase I) to monoclinic (phase II) (shown in Fig. 5.8). Cs-substituted with WPA composite materials were found to improve effectively non-humidified proton conductivity. The anhydrous proton conductivity of fabricated CHS-WPA composite materials with x = 0.5 via dry milling was comparable with the pure WPA system in a wide temperature range under dry nitrogen condition. Although CHS-WPA composite was fabricated via dry milling, the conductivity was not different from dry milling as low molar concentration of CHS. On the other hand, the proton conductivities of the CHS-WPA composite materials fabricated by wet milling were also measured on cooling temperature using pelletized composites with the temperature range of 170 to 50 ^{o}C. These composite materials showed very high proton conductivities in comparing with precursor materials and composite materials with dry milling because DMAc solvent completely promotes new chemical interaction between precursor materials. The proton conductivities of CHS-WPA fabricated via dry milling and wet milling showed from 1.55×10^{-8} to 2.72×10^{-6} S cm^{-1} and from 2.32×10^{-5} to 2.59×10^{-4} S cm^{-1}. CHS-WPA composites fabricated via wet milling with the help of DMAc solvent showed conductivities higher than the precursor samples and CHS-WPA (dry milling). These results proved that the effect of DMAc directly influenced on CHS-WPA composite materials showed the good dispersion, substitution and homogeneously distribution of Cs^{+} ion in CHS into H^{+} ions in WPA. These results imply that the mechanisms on the protonic conduction are quite different between precursor materials and composite materials. This would be related to the hydrogen bond between $CsHSO_4$ and WPA.

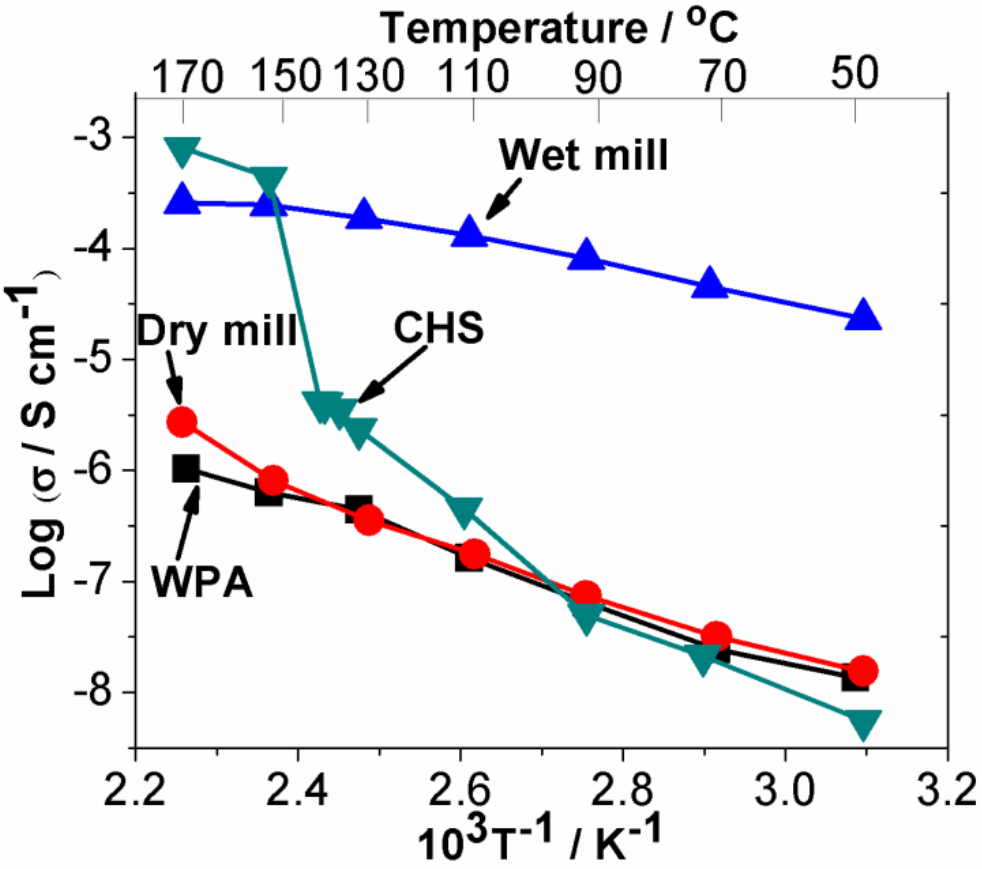

Fig. 5.8. Temperature dependence of anhydrous proton conductivities of precursor WPA, CHS, and prepared CHS-WPA composite materials fabricated by dry milling and wet milling.

5.3.4 ^{1}H-MAS-NMR measurement of precursor samples and prepared composite materials

The chemical interaction and dynamics of protons in the CHS-WPA composite materials via mechanochemical dry milling and wet milling were determined by the solid-state ^{1}H-MAS-NMR measurement. One signal (7.64 ppm) was detected in the spectrum of WPA, and was attributed to the proton in WPA (in Fig. 5.9). CHS also showed one signal at 10.50 ppm, which was also ascribed to the proton peak in CHS. After mechanochemical dry milling, the chemical shift of the CHS-WPA composite signal was clearly observed at around 12.45 ppm shifted to low magnetic field (high chemical shift) from precursor WPA that these proton peaks corresponded to WPA. These result indicated that a high chemical interaction occurred in these composites after mechanochemical dry milling. On the other hand, CHS-WPA composite materials fabricated via wet milling also showed high chemical shift at around 12.30 ppm according to TMS position. Besides, according to the effect of DMAc solvent to make good dispersion and high chemical reaction, the new proton peaks was appeared at around 12.83 ppm via high chemical interaction between CHS and WPA. The proton peaks at low magnetic fields corresponded to a high interfacial proton-concentrated region, and are highly mobile and dynamic to enhance proton conductivity under an anhydrous condition. It was shown that a new chemical interaction occurred via hydrogen bonding developed between HSO_4^- and partially Cs-substituted WPA. Thus, the chemical shift of the composite signals exhibited that a new proton percolation region occurred in these composite materials for enhancing the proton conductivity.

For hydrogen bonding calculation, the hydrogen bonding distance (L in pm) between CHS and WPA can be estimated using the equation,

$$L = 100 \times (79.05 - \delta_{iso})/ 25.5 \quad (5.2)$$

Where, δ_{iso} is the ^{1}H chemical shift which expressed in ppm with respect to the TMS signal [24]. Fig. 5.10 shows the correlation for CHS-WPA composite materials fabricated via dry

milling and wet milling between hydrogen bonding distance and anhydrous proton conductivity at 110 ^{o}C. For the mechnochemically synthesized CHS-WPA composite materials, the reduction of the hydrogen bonding distance significantly affects the fast superprotonic diffusion, and increases the high anhydrous proton conductivity of the composite materials in a wide temperature range, especially under ambient pressure. Thus, the new proton conduction path percolated via ion-exchange and hydrogen bonds between HSO_4^- and partially Cs-substituted WPA in the composite materials. The proton percolation region was formed from interfacial phase in composite samples, hence, anhydrous proton conductivity markedly enhanced [1, 21]. A well-correlated-relation (eq. (5.2)) is known between the OH···O distance, d measured in Å units and the ^{1}H –isotropic chemical shift δ_{iso} (expressed by ppm unit with respect to TMS position). Proton conductivity cannot determine only from the hydrogen bonding distance, and factors such as carrier (proton) concentration and proton mobility should also be considered. ^{1}H-MAS-NMR revealed that a new hydrogen bonding was developed between CHS and WPA. It is quite apparent that a new chemical interaction via hydrogen bond was developed between CHS and WPA. Thus, the shortening of the hydrogen bond distance promotes the high proton conductivity of the CHS-WPA composite materials.

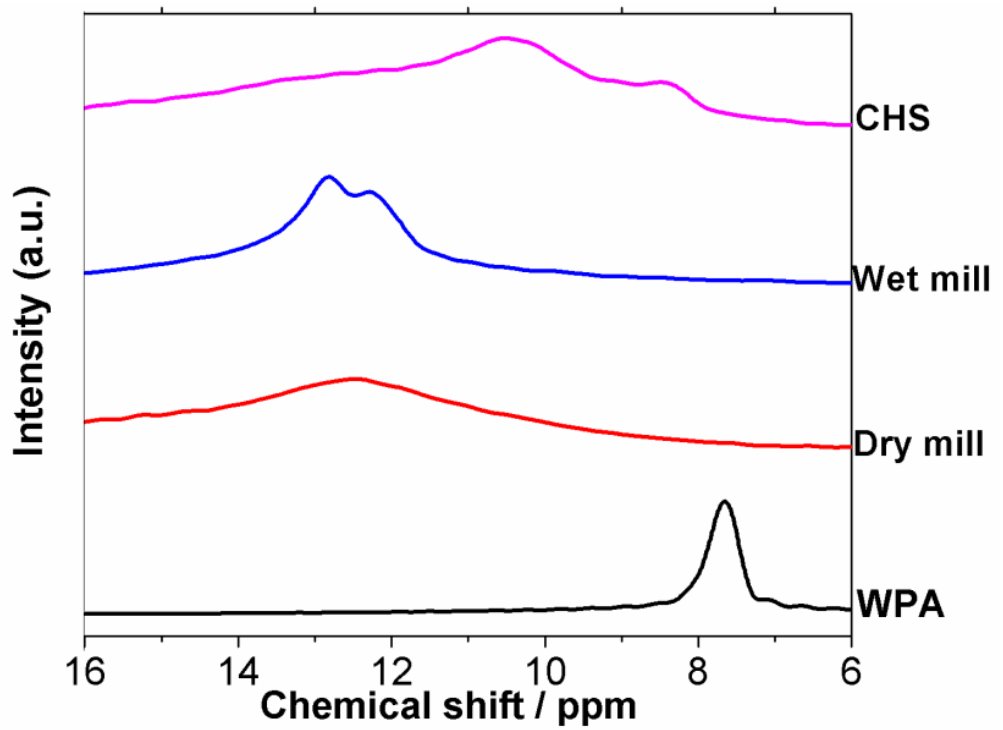

Fig. 5.9. Solid-state ^{1}H-MAS-NMR spectra for precursor WPA, CHS, *x*CHS- (1-*x*)WPA composite materials with $x = 0.5$ produced by (a) mechanochemical dry milling and (b) wet milling.

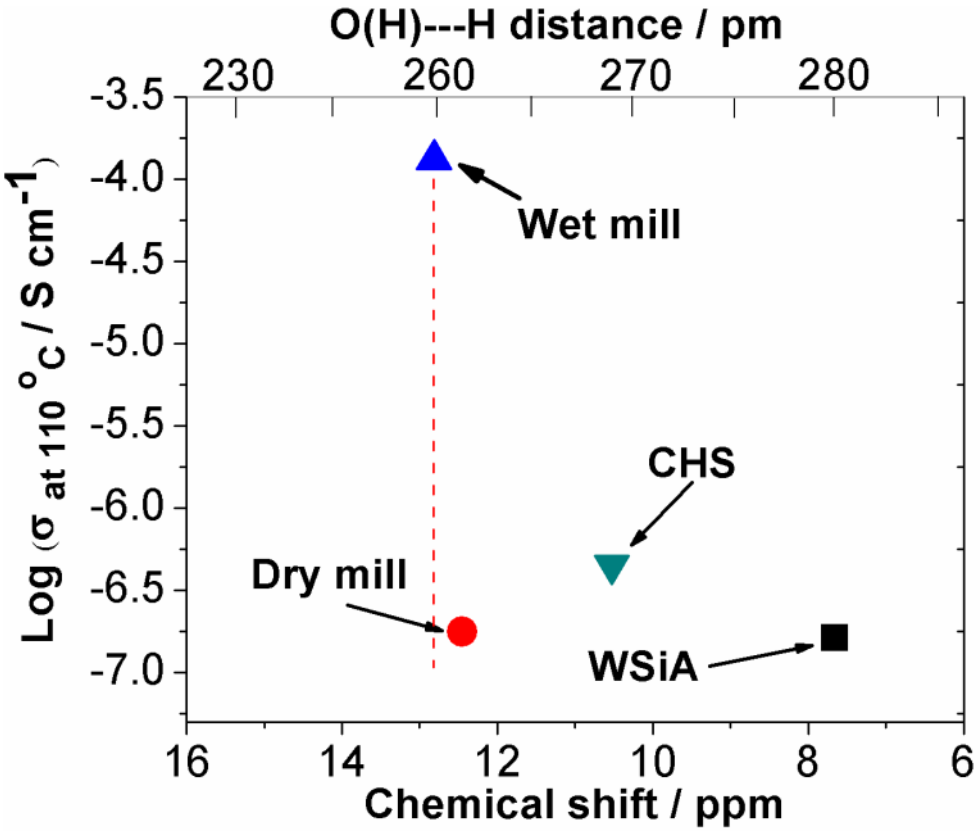

Fig. 5.10. Correlation between hydrogen bond distance (L) and anhydrous proton conductivity at 110 ^{o}C under ambient pressure for precursor WPA, CHS, and CHS-WPA composite materials produced by mechanochemical dry milling and wet milling.

5.3.5 Thermal stability of composite doped-PBI and pristine PBI electrolyte membranes

The thermal stabilities of pristine PBI and CHS-WPA doped-PBI composite membranes were evaluated as shown in Fig. 5.11. In the TGA, the pristine PBI and CHS-WPA doped-PBI membranes showed first weight loss trend at around 120 ^{o}C, attributed to water molecules, and second at around 495-560 ^{o}C, associated with decomposition of the main chain of PBI. Furthermore, the weight loss attributed to the thermal decomposition or evaporation of DMAc in the temperature range from 120 to 180 ^{o}C was not found which means boiling point of DMAc (165 ^{o}C). These results indicate that the incorporated Cs-HPAs composites are stable in their composite electrolytes. Pristine PBI and CHS-WPA doped-PBI doped composite membranes were thermally stable below 500 ^{o}C, which fulfilled the thermal requirement for medium temperature fuel cells.

The SEM images of CHS-WPA/PBI membranes are shown in Fig 5.12 (a and b). The dispersion of CHS-WPA wet milling composite materials showed more homogeneous distribution in the PBI matrix and less agglomeration compared with the dispersion of CHS-WPA dry composite materials. These observations suggested that CHS-WPA wet composite materials showed the new formation of strong chemical reaction and well-distribution into PBI matrix than CHS-WPA dry composite materials because DMAc behaves as a good dispersion medium will either weaken or completely break the precursor material bonds by partial or complete between CHS and WPA to make new bond formation. From cross-section images of the CHS-WPA(wet)/PBI showed highly additive dispersion composite materials into PBI matrix while the CHS-WPA(dry)/PBI showed composite agglomeration in PBI matrix.

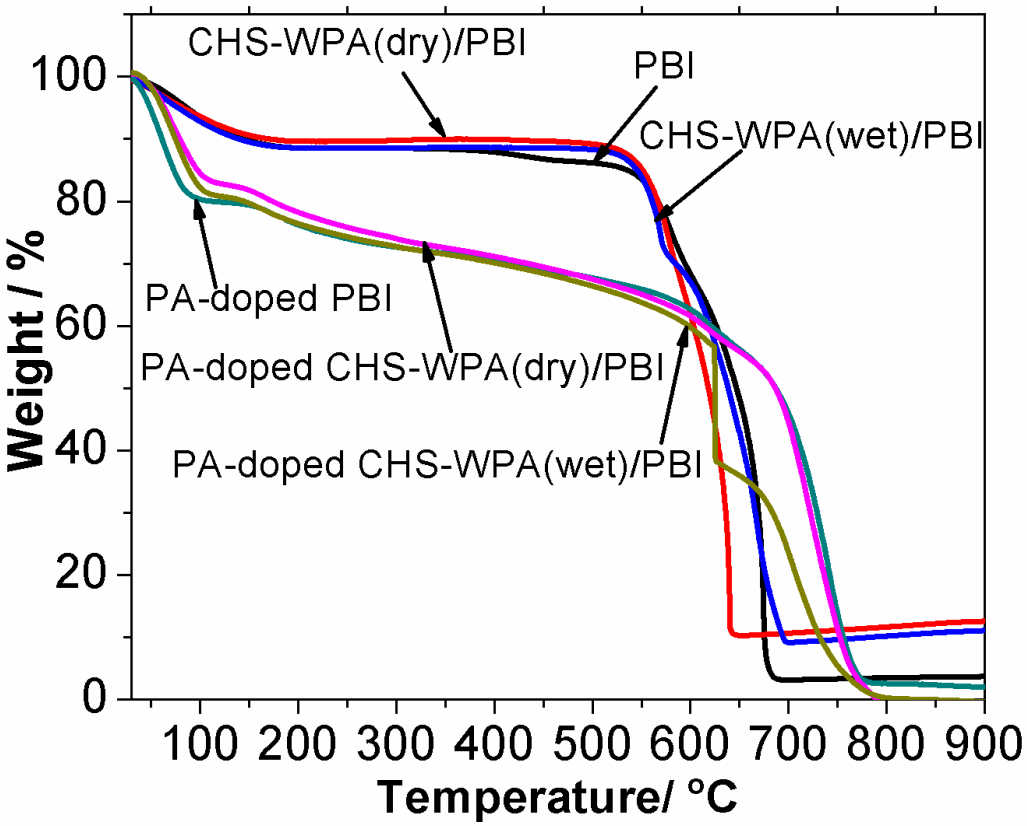

Fig. 5.11. TGA curves of pristine PBI, CHS-WPA(dry)/PBI, and CHS-WPA (wet)/PBI electrolyte membranes.

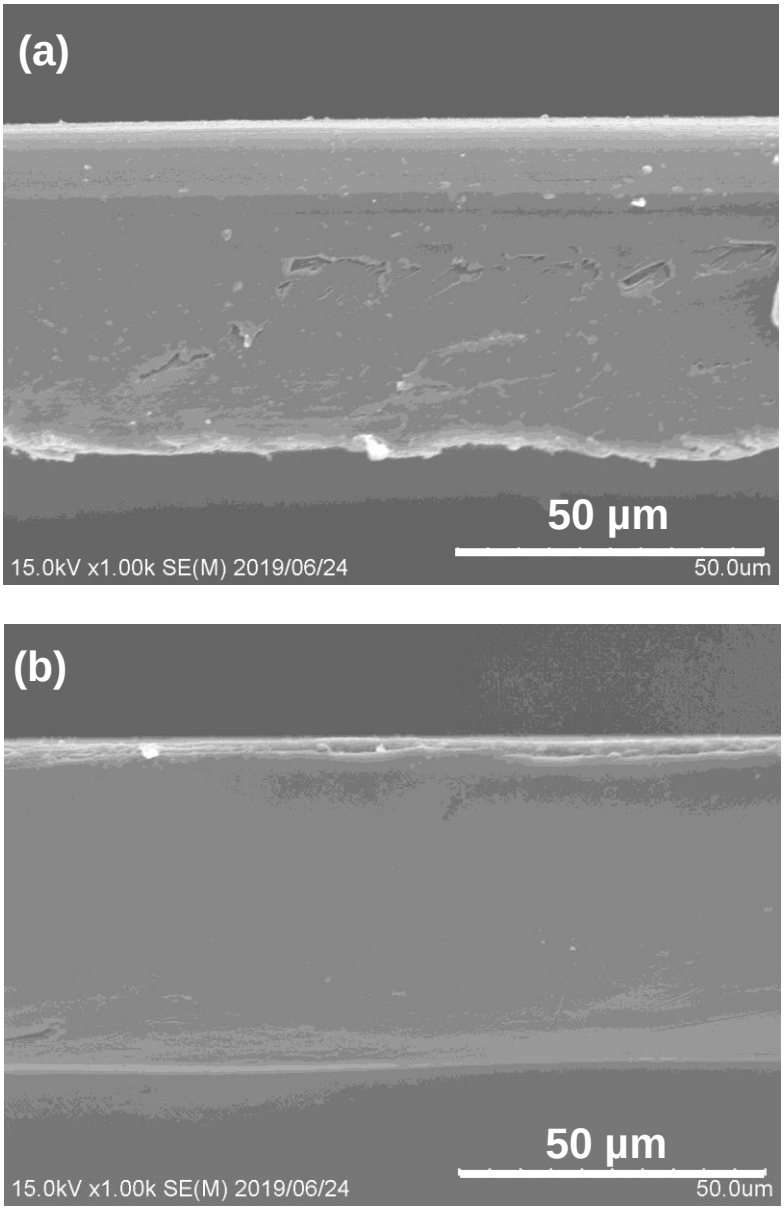

Fig.5.12. FESEM images of CHS-WPA composite materials produced by (a) CHS-WPA(dry)/PBI, and (b) CHS-WPA(wet)/PBI membranes

5.3.6 Electrochemical characteristics of pristine PBI and CHS-WPA doped-PBI composite electrolyte membranes

Anhydrous proton conductivities of pristine PBI and CHS-WPA/PBI composite electrolyte membranes were measured along the temperature range 50-150 ^{o}C. Fig. 5.13 shows the temperature-dependent conductivity measurements of pristine PBI and composite PBI membranes with 8 mol of PADL. The conductivities' trends of all membranes were increasing with increasing the temperature in the range from 50 to 150 ^{o}C. However, the conductivities value of the CHS-WPA(dry)/PBI and CHS-WPA(wet)/PBI membrane were observed that they showed higher than that of the pristine PBI. The proton conductivities of pristine PBI were ranged from 2.11×10^{-4} to 8.99×10^{-4} S cm^{-1} and the proton conductivities of CHS-WPA (dry)/PBI and CHS-WPA(wet)/PBI showed 3.11×10^{-4} to 9.12×10^{-4} S cm^{-1} and 3.99×10^{-4} to 1.11×10^{-3} S cm^{-1} respectively. CHS-WPA(wet)/PBI membrane showed highest conductivity compared with CHS-WPA(dry)/PBI membrane and pristine PBI. In addition, it was observed that at higher CHS-WPA concentrations, > 10 wt%, the CHS-WPA settled at the bottom part of the composite membrane, resulting in non-homogenous membranes, which could also be a contributory factor to the poor performance of composite membranes with higher CHS-WPA content. These observations suggest that CHS-WPA composite membranes with nano-scale composites maintain acid and water retention properties comparing with pristine PBI membrane for enhancing the proton conductivity after adsorbing PA.

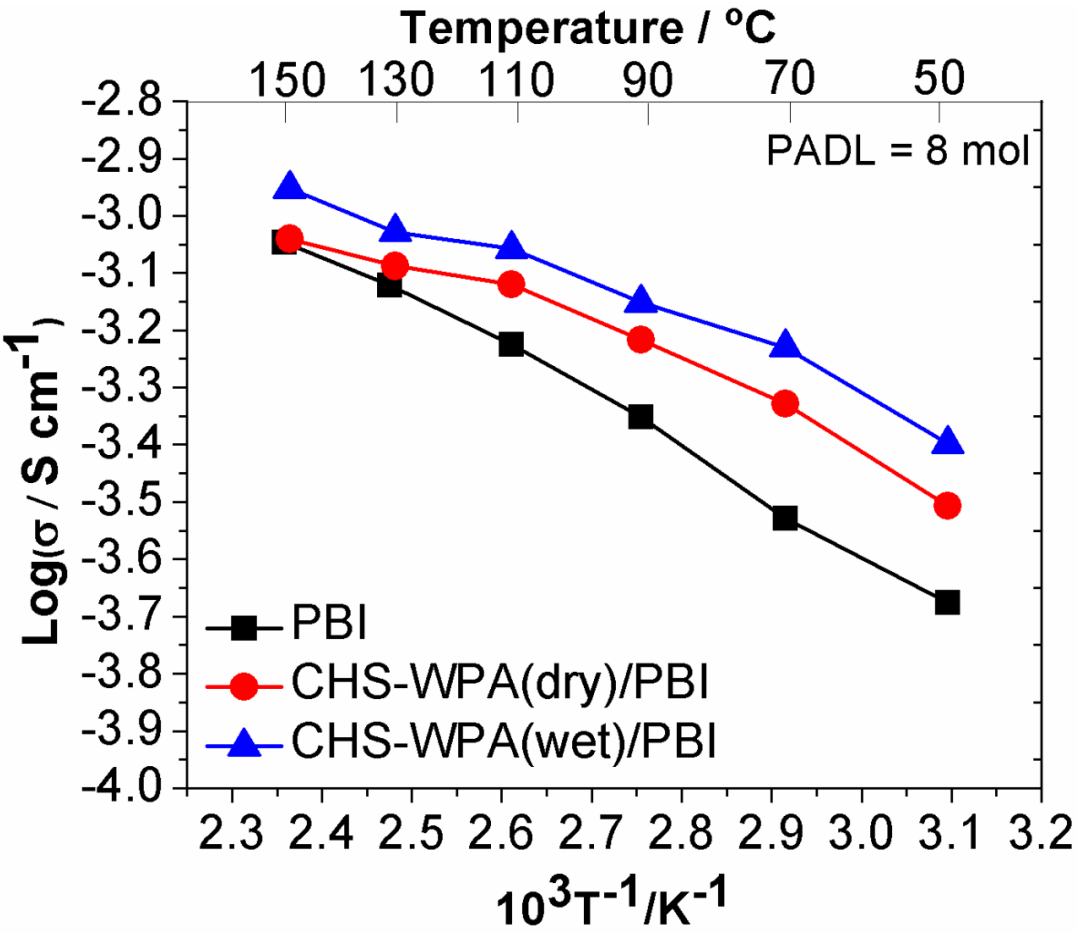

Fig. 5.13. Temperature dependence of conductivity of pristine PBI membrane, 0.5CHS-0.5WPA (dry)/PBI and 0.5CHS-0.5WPA(wet) /PBI composite membranes under anhydrous condition.

The fuel cell evaluation of electrolyte membranes was performed according to their results under anhydrous condition (shown in Fig. 5.14); with power density values of 268, 332, and 402 mW cm^{-2} for pristine PBI, CHS-WPA(dry)/PBI and CHS-WPA(wet)/PBI for 150 ^{o}C measurement. While CHS-WPA/PBI membranes showed the open circuit voltages (> 0.86 V) for low gas permeability, pristine PBI showed the open circuit voltage less than 0.8 V for high gas permeability. After increasing the FC evaluating temperature from 150 to 160 ^{o}C, the power density of CHS-WPA(wet)/PBI was increased from 402 to 425 mW cm^{-2} because of faster kinetics of the electrochemical reaction and the easier water management. To make the comparison between CHS-WPA/PBI membranes and pristine PBI in Fig. 4.14, it can be seen that all the CHS-WPA/PBI membrane fuel cells showed high performance compared with pristine PBI. Thus, the CHS-WPA components in the PBI matrix emphatically adsorbed and retained the PA acid groups in their CHS-WPA/PBI composite membranes to enhance proton conduction mechanism and prevent acid leaching problem.

The current stability tests of CHS-WPA(wet)/PBI membrane and pristine PBI were measured to make confirmation of the acid retention and thermal stability of the CHS-WPA/PBI and pristine (Fig. 5.15). The stability test of composite membranes and pristine PBI was performed as fixed current measurements (0.2 A/cm^{-2}, 24 h). While CHS-WPA(wet)/PBI membrane showed constant potential condition (~0.614 V), the pristine PBI was observed for the degradation of potential (< 0.6V) after 8 h measurement under the operating temperature 150 ^{o}C. These observations of cell performance suggested that inorganic composite additives partly supported to the PA acid retention of the adsorbed PA ligands via to new proton conduction of CHS-WPA/PBI matrix. Thus, the grain nanostructures of the CHS-WPA composites with nano-scaled particles by wet milling in the PBI matrix supported to be homogeneously dispersed in the membrane matrix and also created new proton conduction path after adsorption of PA [26].

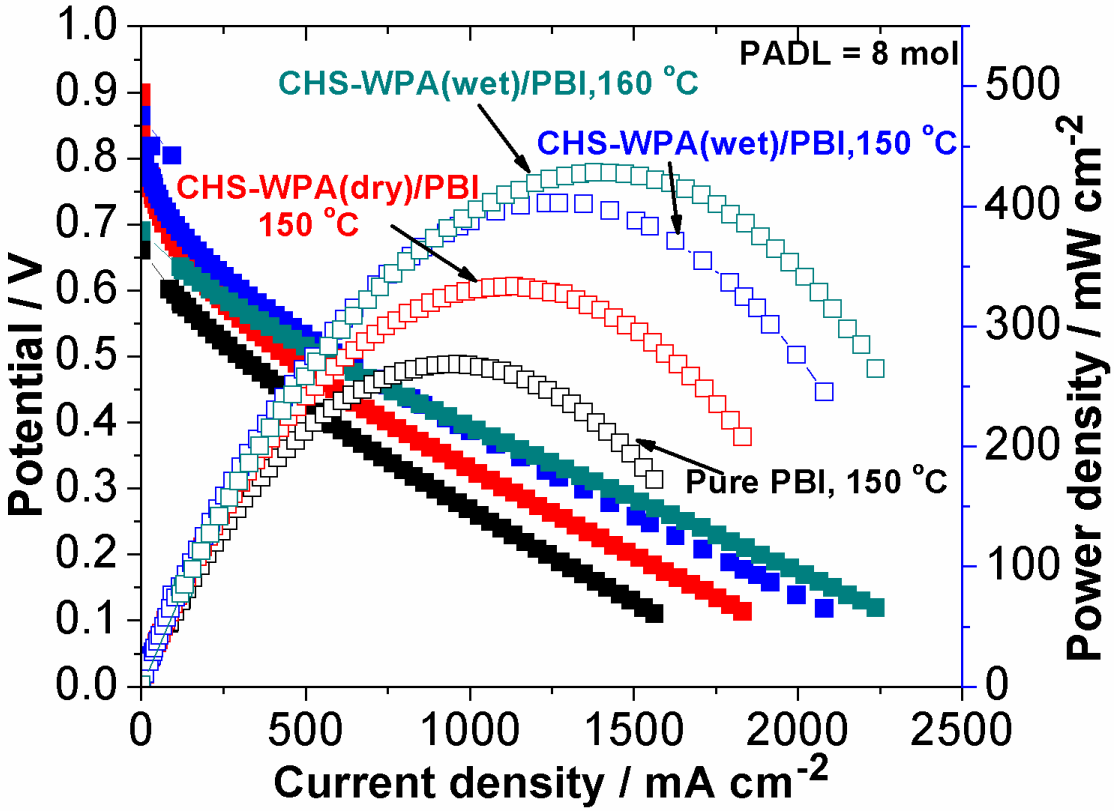

Fig. 5.14. Fuel cell performance and polarization curve of pristine PBI membrane, 0.5CHS-0.5WPA (10wt%) /PBI at 150 ^{o}C and 0.5CHS-0.5WPA(10wt%) /PBI composite membranes at 160 ^{o}C under anhydrous condition.

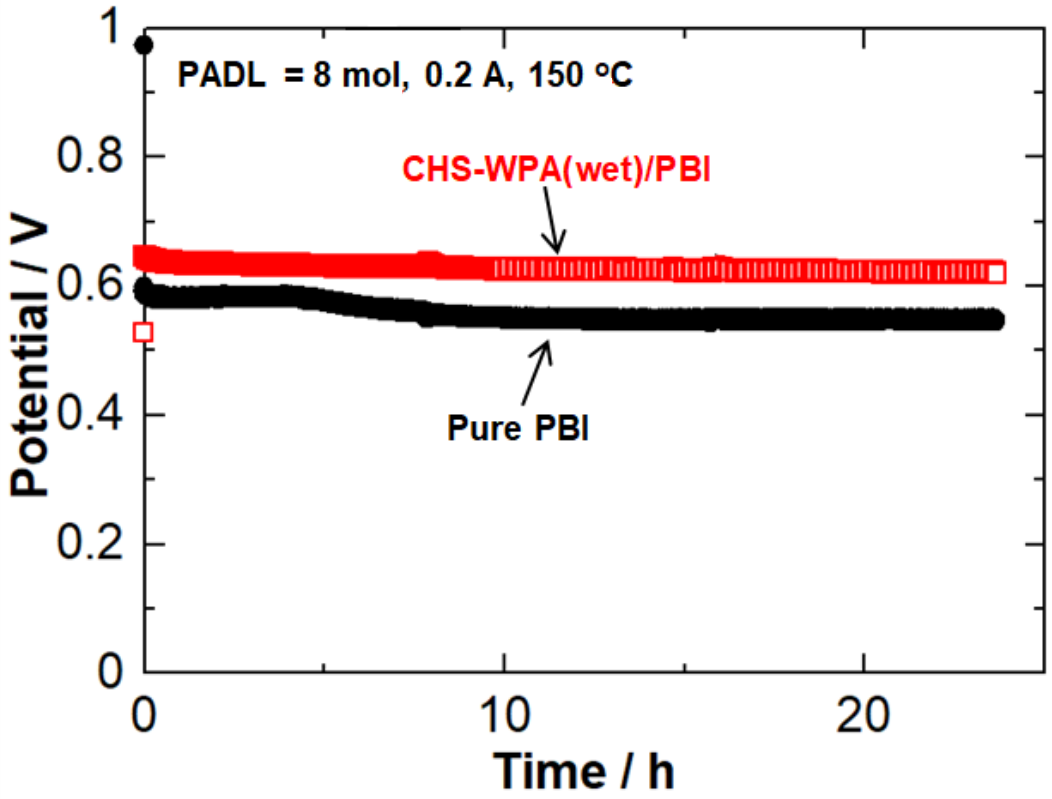

Fig. 5.15. Constant current density measurement of pristine PBI membrane and 0.5CHS-0.5WPA (wet) /PBI at 150 ^{o}C under anhydrous condition.

5.4 CONCLUSIONS

Inorganic solid acid 0.5CHS-0.5WPA (in mol) composite materials have been fabricated by mechanochemical dry milling and wet milling. ^{1}H-MAS-NMR, FT-Raman, and conductivity measurements suggested that the proton conduction at CHS-WPA composite materials via wet mechanochemical milling was observed faster than that of precursors CHS and WPA, and CHS-WPA composite fabricated by dry mechanochemical milling because these composite regions showed more proton percolation with the effect of using DMAc solvent to be high chemical interaction. After the fabrication of CHS-WPA composite materials, DMAc solvent exhibited a promising candidate for fabricated CHS-WPA composite materials via mechanochemical wet milling in comparing with CHS-WPA with mechanochemical dry milling according to the proton conductivity measurement, and ^{1}H-MAS-NMR measurement. From XRD, the main diffraction peaks of all composite materials shifted to large angles in their fabricated composites via ion-substitution reaction between H^{+} ions in WPA and Cs^{+} ion from CHS. From FE-SEM, fabricated CHS-WPA composite materials via wet mechanochemical milling revealed more distribution of nanoparticles than that of dry composite materials. According to proton conductivity results, the proton conductivities of CHS-WPA composite materials via mechanochemical wet milling was larger than the conductivity of dry milling composite at around 10^{-3} Scm^{-1} with regarding the ^{1}H-MAS-NMR measurements which showed a new proton conduction in their composites via ion-exchange reaction according to reduction of hydrogen bonding distance at low magnetic fields (higher chemical shifts). Thus, these observations proved that the new proton conduction mechanisms effected to enhance the proton conductivities of composite materials with the help of DMAc solvent during the fabrication process between CHS and WPA. Inorganic-organic CHS-WPA/PBI membranes were observed for enhanced adsorption and retention properties of PA under the operating temperature (150-160 ^{o}C) fuel cell

evaluation via new proton conduction path of CHS-WPA composite materials. CHS-WPA(wet)/PBI membranes at 150 ^{o}C showed higher performance with 402 mW cm^{-2} compared with CHS-WPA(dry)/PBI (332 mW cm^{-2}) and pristine PBI(268 mW cm^{-2}). CHS-WPA(wet)/PBI membrane at 160 ^{o}C showed highest performance with 425 mW cm^{-2} for fast kinematic reaction during FC evaluation. For constant current test, CHS-WPA(wet)/PBI composite membrane showed more stable potential over 24 h period while the potential of pristine PBI was decreased after 8 h. The effect of inorganic additive CHS-WPA composite materials enhanced the FC performance and potential durability for medium temperature fuel cells.

REFERENCES

[1] S-Y. Oh, T. Yoshida, G. Kawamura, H. Muto, A. Matsuda, Electrochim. Acta **56** (2011) 2364-2371.

[2] P. Staiti, Mater. Lett. **47** (2001) 241-246.

[3] M. Tatsumisago, T. Tezuka, A. Hayashi, K. Tadanaga, Solid State Ionics **176** (2005) 2909-2912.

[4] Y. Daiko, S. Hayashi, A. Matsuda, Chem. Mater. **22** (2010) 3418-3425.

[5] O. Savadogo, J. Power Sources **127** (2003) 135-161.

[6] Q. Li, R. He, J. O. Jensen, and N. J. Bjerrum, Fuel Cells **4** (2004) 147-159.

[7] R. Zeis, Beilstein, J. Nanotechnol. **6** (2015) 68–83.

[8] Q. Li, R. He, J. O. Jensen, and N. J. Bjerrum, Chem. Mater. **15** (2003) 4896-4915.

[9] T. Myles, L. Bonville, and R. Maric, Catalysts **7** (2017) 1-27.

[10] T. Okuhara, N. Mizuno, M. Misono, Appl. Catal. A-Gen. **222** (2001) 63-77.

[11] H-J. Eom, D-W. Lee, S. Kim, S-H. Chung, Y.G. Hur, K-Y. Lee, Fuel **126** (2014) 263-270.

[12] S-Y. Oh, T. Yoshida, G. Kawamura, H. Muto, M. Sakai, A. Matsuda, Mater. Sci. Eng. B **173** (2010) 260-266.

[13] D. Aili, Y. Gao, J. Han, Q. Li, Solid State Ionics **306** (2017) 13-19.

[14] S-Y. Oh, G. Kawamura, H. Muto, A. Matsuda, Electrochim. Acta **75** (2012) 11-19.

[15] S.M. Haile, D.A. Boysen, C.R.I. Chisholm, R.B. Merle, Nature **410** (2001) 910.

[16]S-Y. Oh, K. Kawai, G. Kawamura, A. Matsuda, Mater. Res. Bull. **47** (2012)2931-2935.

[17] M. Mizuno, S.Hayashi, Solid State Ionics **167**(2004) 317-323.

[18] S. Hayashi, M. Mizuno, Solid State Ionics **17**1(2004) 289-293.

[19] J. Baran, M. K. Marchewka, J. Mol. Struct. **614** (2002) 133-149.

[20] F. J. Berry, G. R. Derrick, M. Mortimer, Polyhedron **68** (2004) 17-22.

[21] A. Matsuda, V. H. Nguyen, Y. Daiko, H. Muto, M. Sakai, Solid State Ionics **181** (2010) 180-182.

[22]S. Sampurnam, T. Dhanasekaran, A. Padmanaban, S. Muthamizh, D. Latha, G.Gnanamoorthy, S. Munusamy, V. Narayanan, Mater. Today: Proc. **5** (2018) 8808-8811.

[23] U.B. Mioč, M. R. Todorović, M. Davidović, Ph. Colomban, I. H. Antunović, Solid State Ionics **176** (2005) 3005-3017.

[24] L. Pesaresi, D.R. Brown, A. F. Lee, J. M. Montero, H. Williams, K. Wilson, Appl. Catal. A-Gen. **360** (2009) 50-58.

[25] J. Mbah, B. Krakow, E. Stefanakos, J. Wolan, Electrochem. Solid St. **12** (2009) E12-E16.

[26] M.J. Janik, R.J. Davis, M. Neurock, J. Am. Chem. Soc. **127** (2005) 5238.

[27] A. Matsuda, S-Y. Oh, V.H. Nguyen, Y. Daiko, G. Kawamura, H. Muto, Electrochim. Acta **56** (2011) 9364-9369.

[28] A. Matsuda, T. Kikuchi, K. Katagiri, Y. Daiko, H. Muto, M. Sakai, Solid State Ionics **178** (2007) 723-727.

[29] A. Matsuda, V. H. Nguyen, Y. Daiko, H. Muto, M. Sakai, Solid State Ionics **181**(2010) 180-182.

[30] A. Srikanth, B. Viswanadham, V. P. Kumar, N.R. Anipindi, K. V. R. Chary, Appl. Petrochem. Res. **6** (2016) 145-153.

[31] Y. Daiko, H. Takagi, K. Katagiri, H. Muto, M. Sakai, A. Matsuda, Solid State Ionics **179** (2008) 1174-1177.

[32] C. Xu, X.Xu, X. Wang, M. Mamlouk, K. Scott, J. Mater. Chem. **21** (2011) 6014-6019.

CHAPTER 6

PERFORMANCE ENHANCEMENT WITH METAL OXIDE-DOPED POLYBENZIMIDAZOLE BASED COMPOSITE MEMBRANE IN MEDIUM TEMPERATURE FUEL CELL UNDER ANHYDROUS CONDITION

6.1 INTRODUCTION

Fuel cells for electrical power generation are a research area of high interest because they indicate high power conversion efficiency with low pollution levels. Fuel cells are electrochemical devices which uses external sources of fuel and oxidant for the energy conversion from chemical energy to electrical current. The external fuel sources can run continuously so long as the reactants are being fed into the fuel cell system. There are several types of fuel cell. Some of most commonly mentioned of these are the alkaline, direct methanol, and proton exchange membrane fuel cells. The electrolyte membrane is a main component for medium temperature fuel cell performance [1]. Recently, the commonly used polymer electrolyte fuel cell (PEFC) electrolyte is fluorine-based polymer membranes such as Nafion® with high electrochemical characteristics. However, Nafion® contains hazardous components such as fluorine which is detrimental to the environment during FC operation. Moreover, H_2O works as the proton conducting carriers in Nafion® under high humidification. So, the performance of the PEFC using Nafion® would reduce at ≥100 ^oC, the boiling point of water. One of the solutions to these deficiencies is the use of phosphoric acid (PA)-doped polybenzimidazole (PBI) membrane [2, 3]. PA pays the role of enhancing proton conductivity with a high boiling point, 158 ^oC, and thus, can be used in generating electric power in fuel cells in the medium temperature range (100-200 ^oC). Among different types of non-fluorinated ionomer (non-PFI) materials under active development, PBI is the best and

commonly used. It is a plastic and water insoluble polymer material. Pure PBI is not only a good electronic insulator but also an ionic insulator for the medium temperature polymer electrolyte fuel cells. However, high proton conductivity of PBI can be obtained in the acid-doped form. Generating electricity in the medium temperature range under anhydrous condition has merits, such as application in co-generation systems that effectively utilizes waste heat; and for compacting device since it eliminates the need for a humidifier [4-13].

When pristine PBI membranes are doped with PA, their mechanochemical strength reduces dramatically; and the higher the acid content, the lower the mechanochemical strength, ultimately reducing the stability of the membrane/fuel cell. So, metal oxides are added into PBI matrix to increase the acid uptake and yet maintain or enhance the stability of the membrane/fuel cell. Introducing metal oxide (e.g. TiO_2) into the PBI membrane can enhance its PA concentration because adsorption capability of the inorganic phase benefits in retaining the acid in the membrane at high temperatures and also achieves the by-product water produced. Recently, J. Lobato *et al.* reported that TiO_2 doped-PBI membranes exhibited high doping level of PA per repeat unit of PBI and also showed a higher water uptake compared to pristine PBI, under the similar condition [14]. F. Javier Pinar *et al.* also described metal oxide doped-PBI membranes absorbed large amount of PA within a short period compared with pure PBI [15].

In this research work, in order to improve the proton conductivity (by way of increase PA doping) and fuel cell performance of the PBI electrolyte membrane, TiO_2 was added into PBI to form a composite electrolyte membrane. The observations showed that the leaching of phosphoric acid was suppressed by the addition of TiO_2, which enhanced the phosphate holding power of the composite PBI electrolyte membrane. The large thickness membrane is mainly responsible for the large ohmic polarization and poor power performance of high temperature membrane electrode assembly (HT-MEA). The mechanochemical property of

the doped PBI membrane can be improved by reducing H_3PO_4 (PA) doping level; however, it accompanies a decrease of proton conductivity.

6.2 EXPERIMENTAL PROCEDURE

6.2.1 Starting materials

Reagent grade Titanium (IV) oxide (TiO_2) (21 nm primary particle (TEM), 35-65 m^2g^{-1}(BET), 99.5% Sigma-Aldrich Co. Ltd, Japan) was purchased to fabricate TiO_2 based composite electrolyte membranes. Commercially available *N*,*N*-dimethylacetamide (DMAc, 99.0 vol%, WAKO Pure Chemical Industries, Japan) was also purchased to use as a casting solvent for TiO_2 doped-PBI electrolyte membrane fabrication. Commercial polybenzimidazole (PBI) (Sato Light Industry; MRS0810H, 10wt% in DMAc) was used as received without any further purification.

6.2.2 Fabrication of electrolyte membranes

N,*N*-dimethylacetamide (DMAc) (Wako; 99 %) and PBI (Sato Light Industry; MRS0810H, 10 wt % in DMAc) solution were used to fabricate the pristine PBI electrolyte membrane. 4.8 g of PBI solution was added to 43.23g of DMAc solvent to obtain 1 wt % of PBI solution. The solution was stirred with a magnetic bar at 500 rpm for 1 h to achieve a homogeneous PBI solution. It was then sonicated for 30 min and transferred into a petri dish (φ = 9.7 cm) for membrane casting. Consequently, the solution was heated in an oven between 60-120 ^oC for 24 h. The PBI solution set to give a film thickness of 50-60 μm after the casting. The electrolyte membrane was peeled off from the petri dish and hot-water treated at 90 ^oC for 5 h, as a water durability test and to eliminate residual materials. Subsequently, the electrolyte membrane was washed with water and dried in an oven at 60 ^oC overnight.

The TiO_2/PBI membranes were similarly prepared by the addition of TiO_2 nanoparticles powder (Aldrich; 99.5 wt %, ~21 nm) to the PBI solution, at different weight percents (2 wt %, 10 wt % and 20wt %), before casting. Finally, membranes were immersed in PA (Wako; 85%) at 60 ^{o}C for different time periods to accomplish different desired PA doping levels (PADLs).

6.2.3 General characterization

The morphologies of the PBI membrane and TiO_2-doped PBI membranes were observed by field emission scanning electron microscopy (FE-SEM; S-4800, Hitachi) and optical laser microscope (OLS 4100).

PA retention ability of pristine PBI and TiO_2-doped PBI membranes were estimated using hot water vapor acid leaching setup. 2 × 2 cm^2 membranes were doped to complete 6 mol of PADL. The pristine PBI and TiO_2-doped PBI membranes were suspended over hot water vapor induced from boiling water at 100 °C for 5 h. Then, these membranes are collected every 1 h and wiped thoroughly with tissue paper to eliminate condensed water droplets before weight to measure the PA loss from membranes [16, 17].

Temperature dependence of anhydrous proton conductivities of the membranes was measured by AC impedance spectroscopy over a frequency range of 10^7-1 Hz (Solartron; SI 1260) in a dry nitrogen atmosphere. For the proton conductivity measurement, electrolyte membrane sizes of 2×2 cm^2 were applied. The measuring temperature range was set between 150-50 ^{o}C in a cooling regime. Carbon papers were placed on each side of the membranes as electrodes for the conductivity measurement. The fuel cell performance test for the membranes was carried out in the form of membrane electrode assemblies (MEAs) at 150 ^{o}C operation temperature with commercial Pt-loaded carbon paper sheets (Electro Chem, EC-10-05-7; Pt content = 0.5 mg cm^{-2}, EC-10-05-7). Dry H_2 and O_2 were used, obtained by passing

them through a bubbler. The fuel cell performance greatly depends on the makeup of the cell as well as on the operation conditions of temperature and humidity, so that the assembly processes of the cells and the operation conditions were optimized for each electrolyte by trial and error.

6.2.4 Membrane electrode assembly (MEA) and fuel cell tests

The commercial Pt/C sheets were applied for both anode (1 × 1 cm^2) and cathode (1.5 × 1.5 cm^2). The Pt catalysts sandwiched the PA-doped electrolyte membranes to form the MEAs. The MEA was placed between two high-density graphite blocks with parallel gas flow channels. An electric thermocouple was mounted at the rear of one of the graphite blocks to monitor the desired temperature. Gold-plated steel bolts were screwed on to the graphite blocks as electrical leads [18]. H_2 and O_2 gases were fed to the anode and cathode sides of the cell, respectively, at flow rates of 100 mL min^{-1}.

6.3 RESULTS AND DISCUSSION

6.3.1 PA doping

The PADLs of the membranes were calculated as shown in equation (6.1),

$$\text{PADL} = ((W - W_0) / M_{PA})/(W / M_{PBI}) \quad (6.1)$$

Where, W_0 = membrane weight before doping with phosphoric acid, W = membrane weight after phosphoric acid doping, M_{PA}= Molecular weight of phosphoric acid (98 g mol^{-1}), M_{PBI} = 1 repeat molecular weight of PBI (308 g mol^{-1}).

Fig. 6.1 shows a comparison between the time dependent PADL of TiO_2/PBI electrolyte membrane and pure PBI. As a reference, 6 mol PADL threshold for PBI (pure) and TiO_2/PBI electrolytes was used. The TiO_2/PBI film is doped with 3 mol PA within 20 min, and reaches 6 mol within 35 min, and finally saturates at 9 mol in a total of about 70 min. The pure PBI on the other hand rises to 3 mol PADL within 8 min and levels of until

after 50 min when it begins to rise again to reach a PADL of 6 mol after 80 min, and then to 8 after 90 min. The difference in these PADL rates is ascribed to the fact that phosphoric acid exists between polymer chains of PBI up to a PADL of 3 mol. TiO_2, being hygroscopic, as a result of surface hydroxyl groups, is thought to adsorb and retain a large amount of PA after the initial PADL of 3 mol.

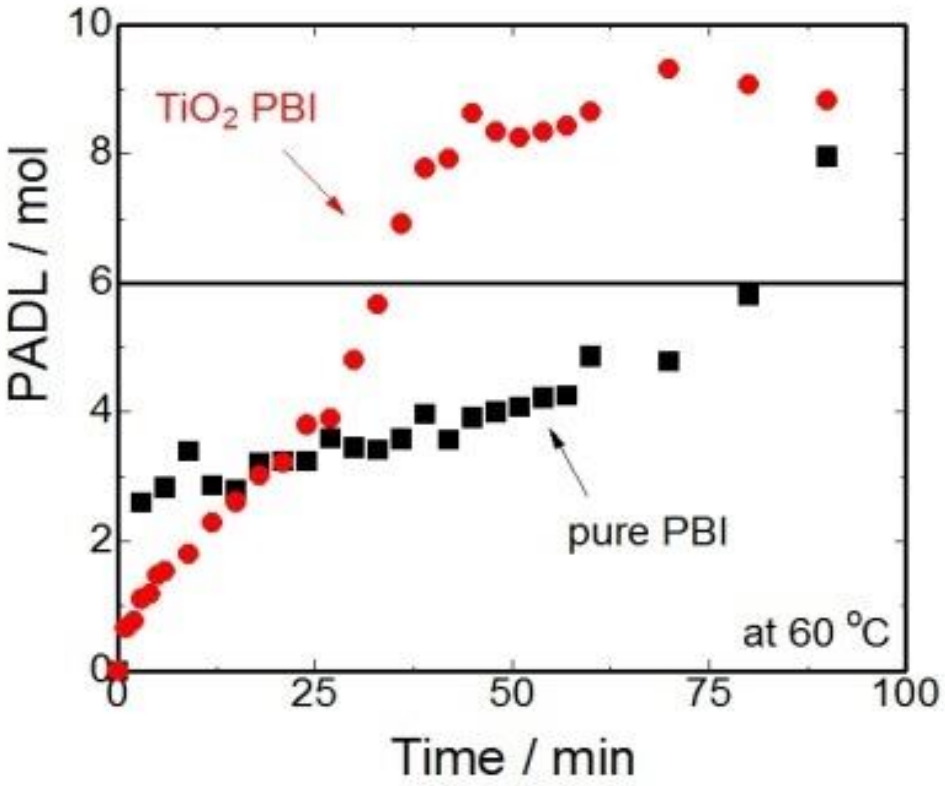

Fig. 6.1. Time-dependent PADL of PBI (pure) and TiO_2/PBI at 60 ^{o}C.

6.3.2 Optical microscope and SEM measurements

The photographs of typical membrane electrolytes are shown in Fig. 6.2 (a and b), showing they are transparent; and their surface textures under optical microscope are shown in Fig. 6.3(a and b), showing homogenous surfaces. Fig. 6.4 (a and b) shows SEM images of cross-sections of the membranes, showing the typical 50-60 μm thickness of the membranes and that the homogeneity extends throughout the membrane and not only the surface. The morphological properties of the TiO_2/PBI membranes depend on the degree of compatibility and dispersibility between the PBI and TiO_2. If it is not proper dispersion between the polymer and inorganic additives, filler agglomerations tend to act as defect sites that limit the mechanochemical strength of the hybrid membranes. From Fig. 6.5(a, b), pristine PBI is uniform and smooth, then TiO_2(2wt%)/PBI exhibits that is uniformly distributed within hybrid membrane as a result of the interaction of hydrogen bonding between the polymer and TiO_2. From Fig. 6.5(c), TiO_2(10wt%)/PBI shows large filler agglomerations in the PBI matrix.

6.3.3 PA retention measurement

PA leaching is approved as one of the major degradation features of membranes for the medium temperature fuel cells operation. From PA leaching tests, PA retention ability of TiO_2/PBI was improved noticeably with addition of metal oxide TiO_2 compared with pristine PBI as shown in Fig. 6.6. For the first hour, great loss of PA (40–50 %) was observed for both pristine PBI and TiO_2/PBI membranes, which can be related with excess (unbounded) PA in PA-doped PBI and PA-doped-TiO_2-PBI polymer matrix. Acid leaching rate was then slowed down and eventually keep on constant after 3 h, which supposed to be related with the bonded PA in the polymer matrix. In comparison within pristine PBI and TiO_2/PBI membranes under the similar experiment condition, relatively, pristine TiO_2/PBI has higher acid retention ability as compared with pristine PBI. Addition of TiO_2 into PBI matrix contributed to better acid retention ability.

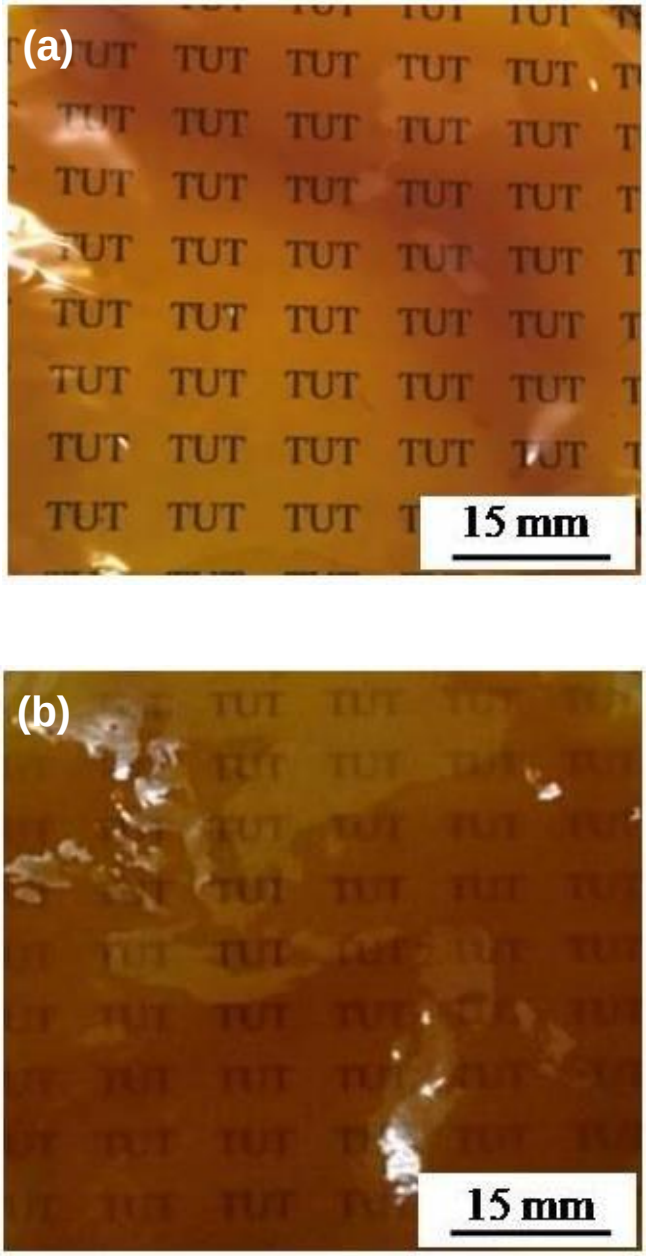

Fig. 6.2. Photographs of membranes: (a) Pure PBI; and (b) 2 wt % TiO_2-PBI.

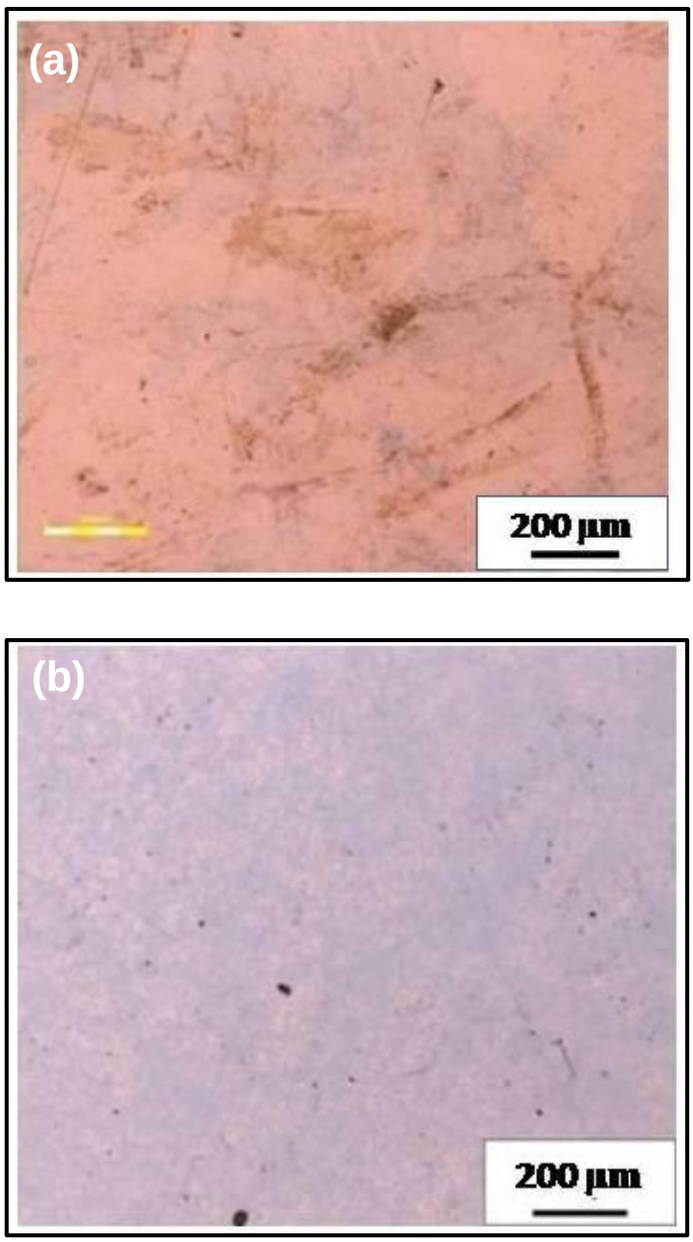

Fig. 6.3. Optical microscope surface observation of: (a) Pure PBI; and (b) 2 wt % TiO_2-PBI membranes.

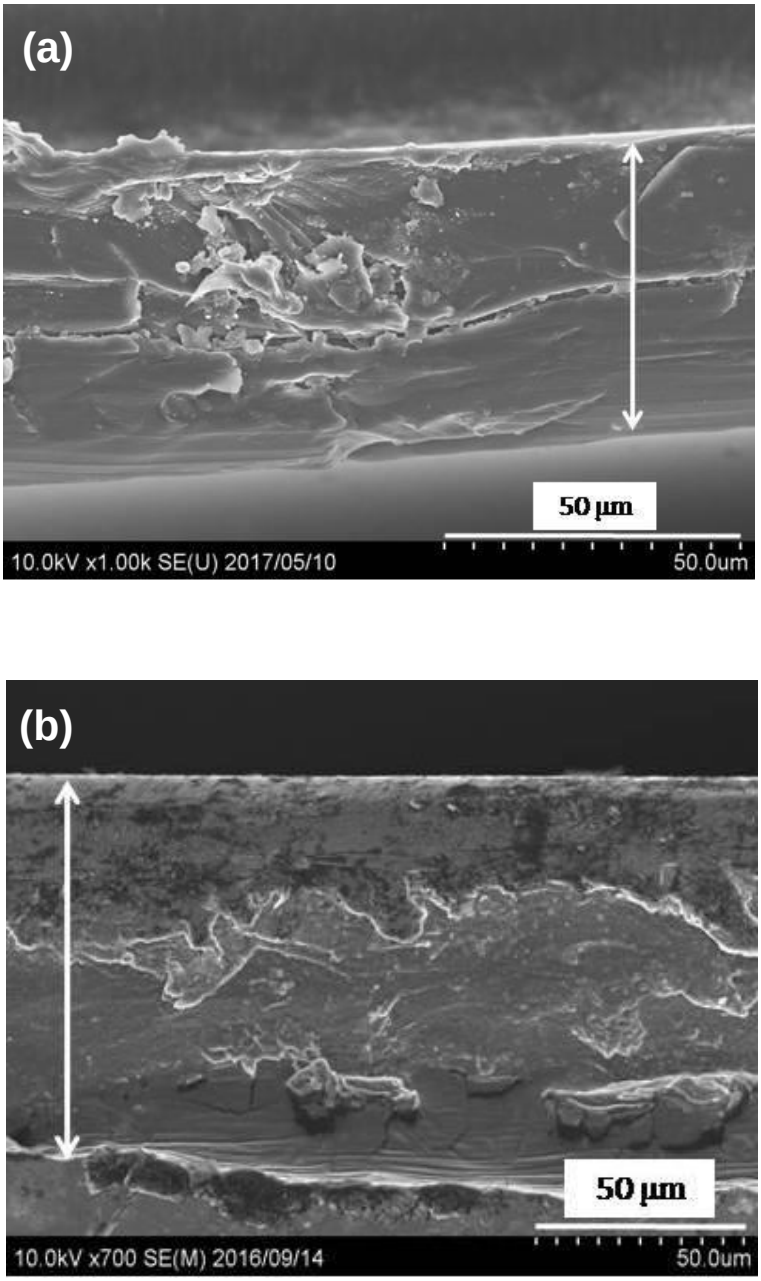

Fig. 6.4. Cross-sectional SEM images of membranes:(a) Pure PBI ;and (b) 2 wt % TiO_2-PBI.

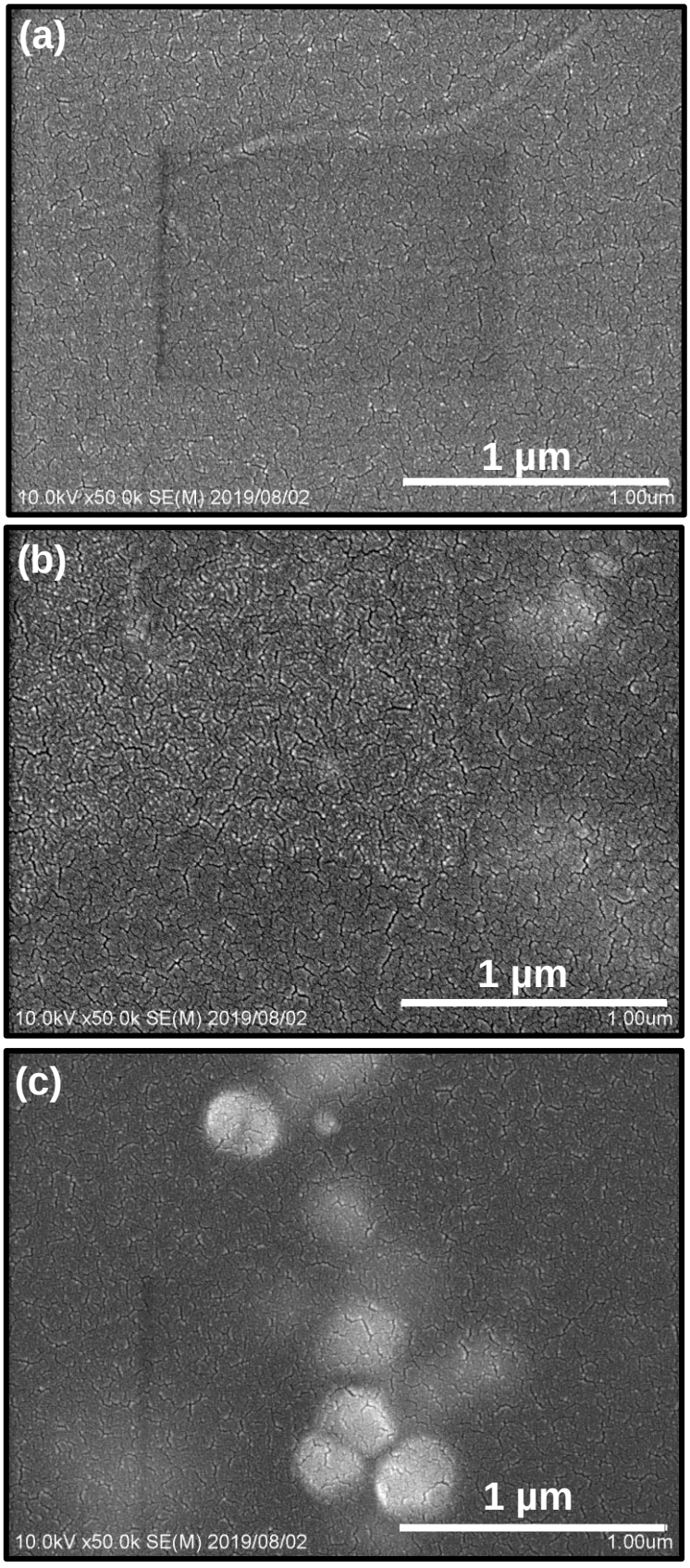

Fig. 6.5. Surface morphological SEM images of membranes:(a) Pure PBI ;and (b) 2 wt % TiO_2-PBI (c) 10 wt% TiO_2-PBI electrolyte membranes.

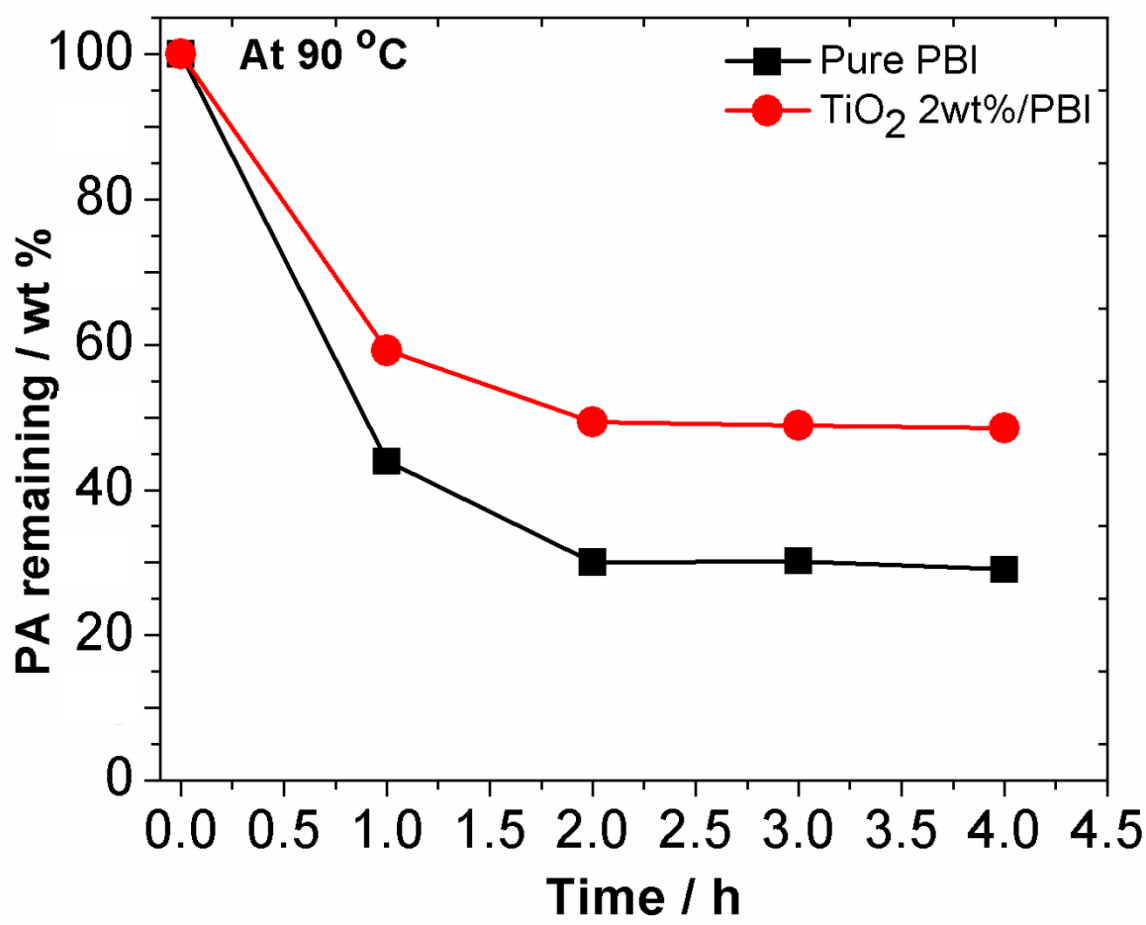

Fig. 6.6. Acid remaining of (a) Pure PBI ; and (b) 2 wt % TiO_2-PBI over 4 h of hot water vapor acid leaching test.

6.3.4 Proton conductivity measurement of membranes and fuel cell power generation test

Fig. 6.7 shows the temperature dependence of conductivity pristine PBI and TiO_2/PBI electrolyte membranes with 6 mol of PADL. The conductivities of both membranes exhibited a trend of increasing conductivity with increasing temperature (from 50 to 150 ^oC). However, the conductivity of the TiO_2/PBI was found to be lower than that of the pure PBI. We think this is due to the more significant contribution of electron transport resistance to the total resistance of the cell than the contributory component due to ionic (proton) transport. The proton conductivity, δ, values were calculated from equation (6.2):

$$\sigma = d / (R \times A) \tag{6.2}$$

Where, d is the thickness of the membrane; R is the direct current resistance of the membrane via electrochemical impedance spectroscopy (EIS) technique; and A is the effective active surface area of the membrane.

For both membranes L and A were the same, indicating that the difference in conductivity values between the two membranes arose from their R values, which is a combined contributory effect of both electron and ionic (proton) transport resistances. Thus, the 2 wt % poor conductor TiO_2 added increased the electron transport component of the R value significantly enough to cause an overall lower conductivity in the TiO_2/PBI than the pure PBI of the same PADL value of 6 mol.

However, when it came to the complete fuel cell performance, their levels of performance reversed, as shown in their polarization and power density curves in Fig. 6.8, with maximum power densities of 195 and 434 mW cm^{-2} for pure PBI and TiO_2/PBI, respectively. The open circuit voltages of both membranes were more than 0.9 V, which indicate that the membranes have low gas permeability [19, 20].

Fig. 6.8 shows the polarization and power density curves of the different TiO_2/PBI composition membranes cell performances. Compared to those of pure PBI, in Fig. 6.8, it can be observed that all the TiO_2/PBI membrane fuel cells showed better performances than the pure PBI membrane fuel cell. This supports our explanation regards the effect of the TiO_2 component; whereas in the conductivity measurements of the membranes there is a dual component effect from electron transport and proton transport, in the fuel cell measurement it is exclusively proton conduction component with regards to the role of the membrane, which is the only variable factor among all the cells. Thus, the TiO_2 component effectively adsorbed and retained the PA acid groups, increasing proton transport as observed in the high power density values of the TiO_2/PBI composite membrane cells; and preventing leaching of the PA acid groups, as observed in the higher polarization curves of the TiO_2/PBI membrane cells.

However, among only TiO_2/PBI composite membranes results, it can be observed that at higher wt % amounts of TiO_2 cell performance reduces, in both cell polarization and power density (Fig. 6.9). These observations suggest that there is a synergistic effect of TiO_2 and PBI on the performance of the cell membrane. In addition it was observed that at higher TiO_2 concentrations, $\geq$ 10 wt%, the TiO_2 settled at the bottom part of the membrane, resulting in non-homogenous membranes, which could also be a contributory factor to the poor performance of composite membranes with higher TiO_2 content. Further, this settling of TiO_2 at one face of the membrane will cause absence of PA groups at the membrane/catalyst interface of that face, which is critical for reduced charge transfer resistance at the interface [12].

To confirm the PA group retention effect of the TiO_2 component the constant current stability curves of 2 wt % TiO_2/PBI membrane cell was compared to that of pure PBI as shown in Fig. 6.10. The measurement was carried out at a current density of 0.2 A cm^{-2} for about 40 h. It can be observed that the composite membrane of 2 wt % TiO_2/PBI had a

constant potential throughout the measuring period, while that of the pure PBI was observed to begin decreasing after the first 5 h, with a sharp and severe decrease (about 80 % of its original value) after 25 h. This observed superior performance by the composite membrane was mainly attributed to the retention of the adsorbed PA ligands due to the TiO_2, in addition to the capture of cell reaction radicals such as ·OH, ·OOH and H_2O, which are thought to attack the PBI membrane [21].

In addition, the nanostructure of the TiO_2 particles (~21 nm) was thought to aid in a homogenous distribution within the membrane and also afforded it large surface area for the adsorption of PA ligands and capture of radicals [22, 23].

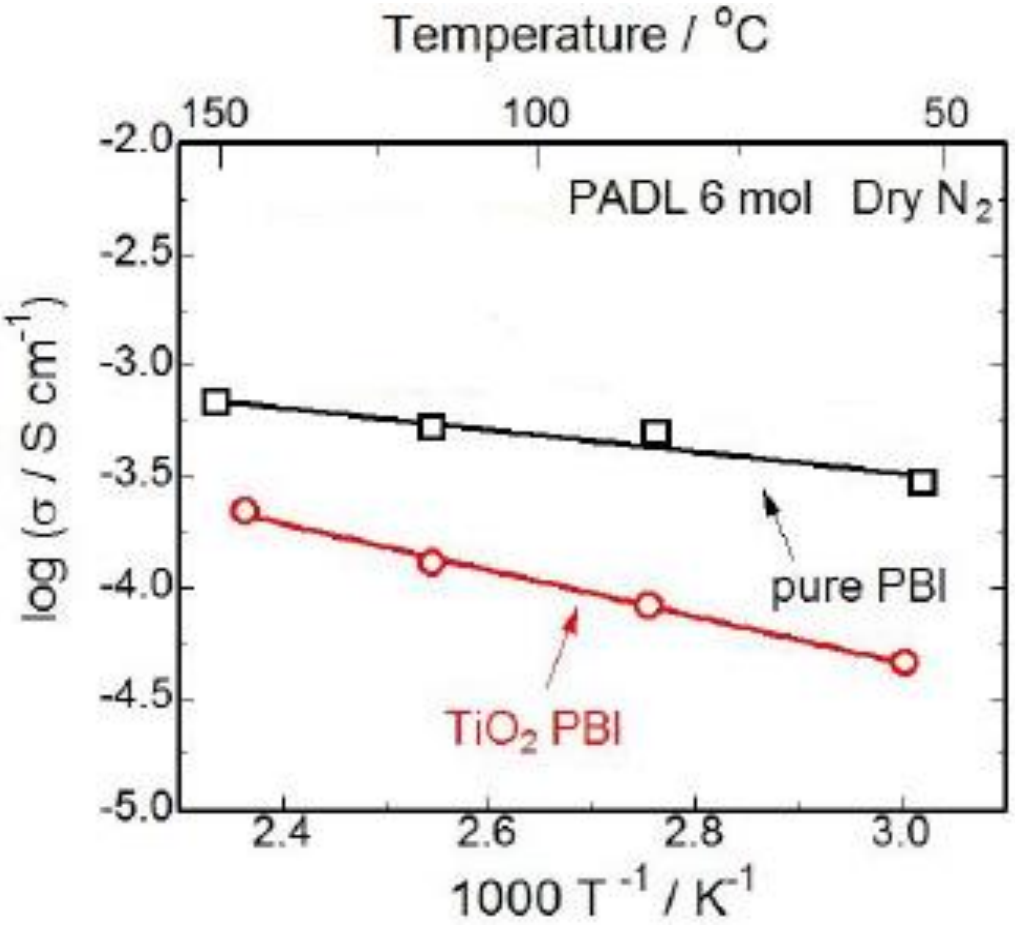

Fig. 6.7. Temperature dependence of conductivity of pure PBI and 2wt %TiO_2/PBI membranes of PADL of 6 mol under anhydrous condition.

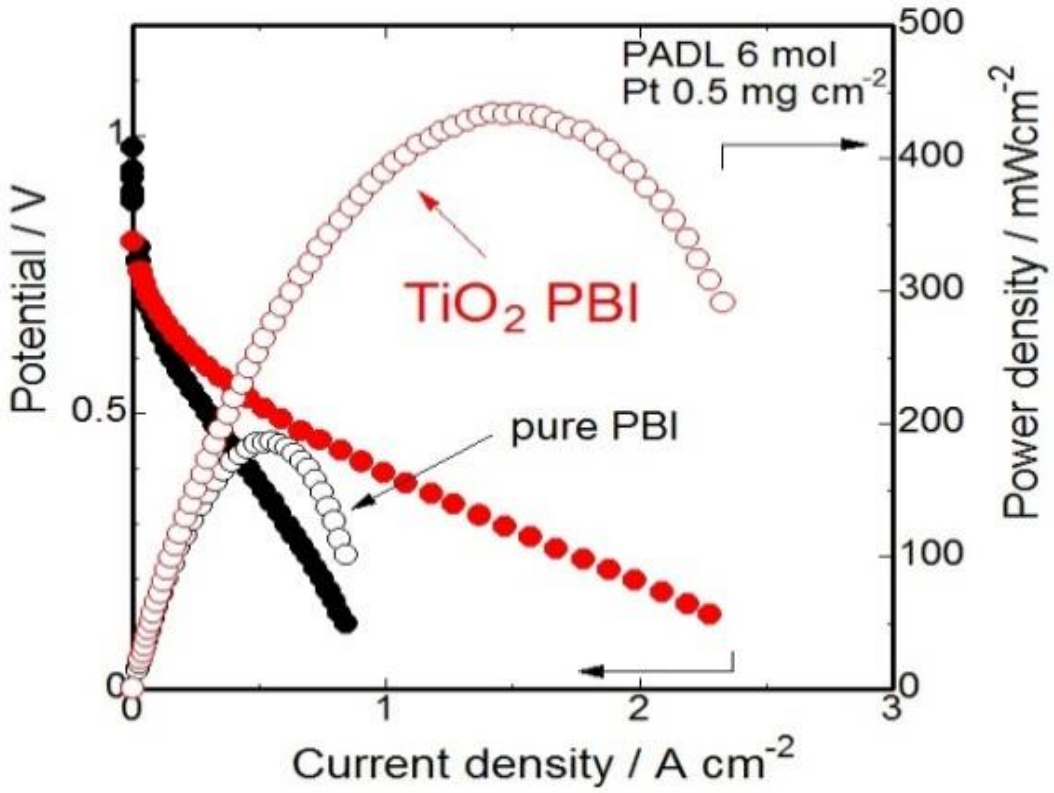

Fig. 6.8. The potential and power density curves of pure PBI and 2 wt % TiO_2/PBI membranes with PADLs of 6 mol.

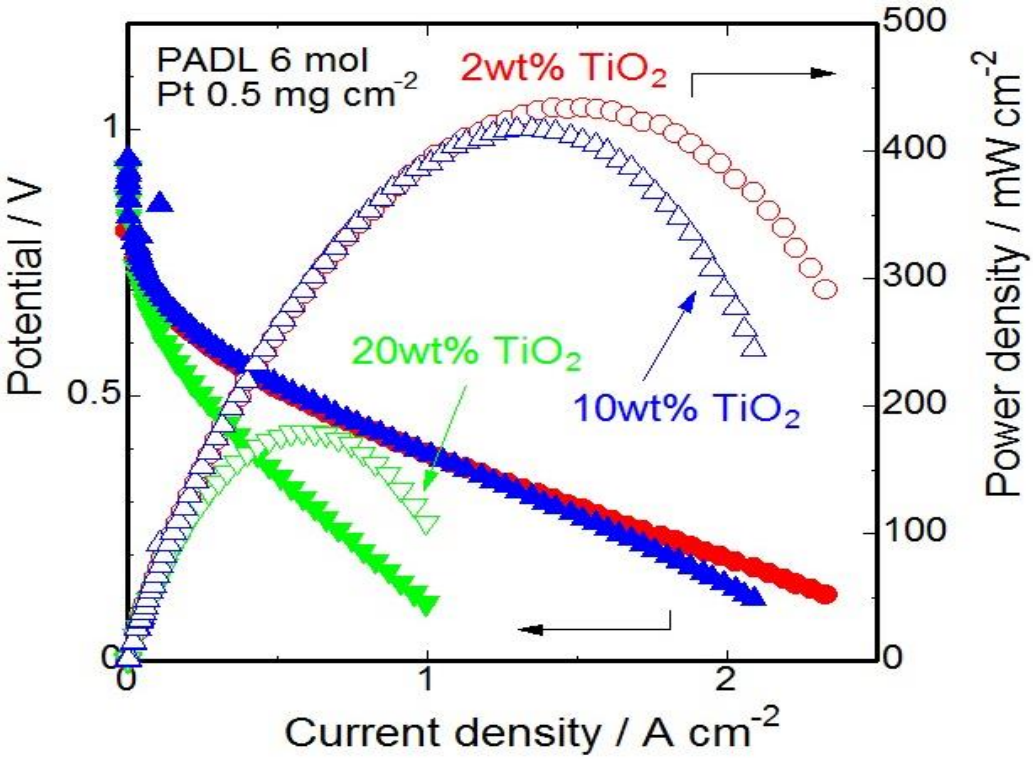

Fig. 6.9. The potential and power density curves of pure PBI and TiO_2 (2 wt %, 10 wt %, 20 wt %)/PBI membranes with PADLs of 6 mol.

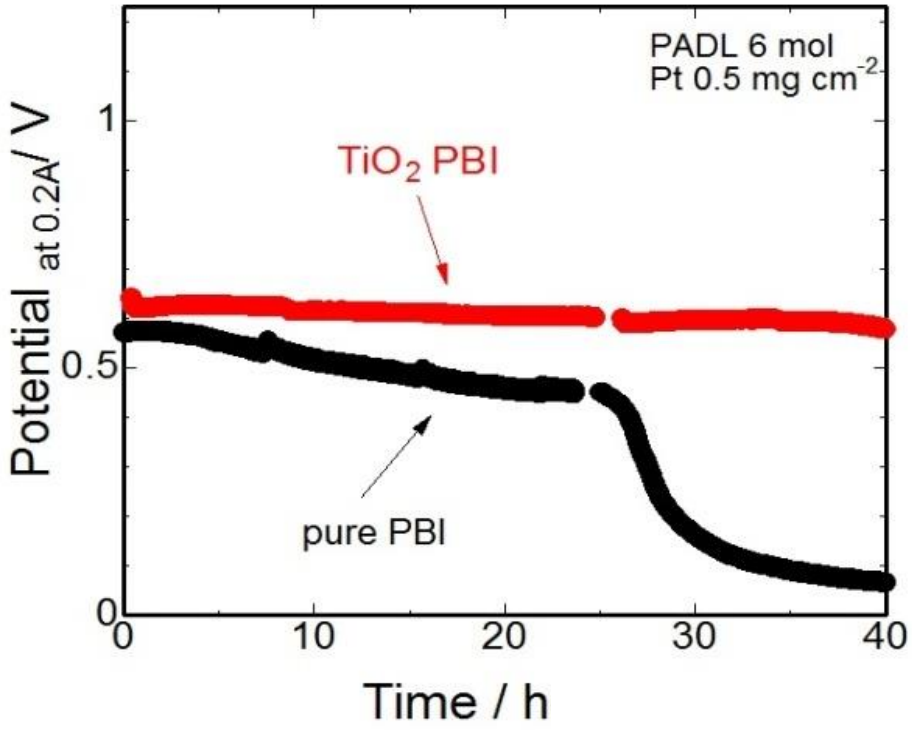

Fig. 6.10. Constant current density measurement for pure PBI and 2wt % TiO_2-PBI membranes.

6.4. CONCLUSIONS

In this study of metal oxide, TiO_2 was added to PBI at various weight compositions to form TiO_2/PBI composite membranes; with the target to enhance fuel cell performance in the medium temperature region (100-200 ^oC) via enhanced adsorption and retention of PA ligands. The results showed superior performance of the TiO_2/PBI membranes over the pure PBI membrane, with an optimal TiO_2 composition of 2 wt % giving a power density of 434 mW cm^{-2}, compared to 195 mW cm^{-2} of the pure PBI membrane. The composite membrane also showed a constant current potential over a 40 h period while that of the pure PBI begun decreasing after 5 h with about 80 % loss in potential after 25 h. These observed enhanced performance indicators in the TiO_2/PBI composite membranes were attributed to the enhancement effect, with some level of synergistic effect with PBI, of the TiO_2 component on PA adsorption and retention, and the capture of radical by-products from the fuel cell reactions that attack the PBI membrane. These results provide fundamental understanding and information of the enhancement effect of metal oxide TiO_2 on the cell performance of PBI based fuel cells and thus a good guide for fuel cell researchers and industry.

REFERENCES

[1] M. Mizuno, S. Hayashi, Solid State Ionics **167** (2004) 317-323.

[2] F. Mack, S. Heissler, R. Laukenmann, R. Zeis, J. Power Sources **270** (2014) 627-633.

[3] Y. Oono, A. Sounai, M. Hori, J. Power Sources **189** (2009) 943-949.

[4] J. S. Wainright, J-T. Wang, D. Weng, R. F. Savinell, M. Litt, J. Electrochem. Soc. **142** (1995) L121-L123.

[5] B. Xing, O. Savadogo, Electrochem. Commun. **2** (1999) 697-702.

[6] Y. –L. Ma, J. S. Wainright, M. H. Litt, R. F. Savinell, J. Electrochem. Soc. **151**(2004) A8-A16.

[7] L. Xiao, H. Zhang, E. Scanlon, L. S. Ramananthan, E.-W. Choe, D. Rogers, T. Apple, B.C Benicewicz, Chem. Mater. **17** (2005) 5238-5333.

[8] T. J. Schmidt, J. Baurmeister, J. Power Sources **176** (2008) 428-434.

[9] Z. Chang, H. Pu, D. Wan, L. Liu, J. Yuan, Z. Yang, Polym. Degrad. Stab. **94** (2009) 1206-1212.

[10] R. Wycisk, J. Chisholm, J. Lee, J. Lin, P. N. Pintauro, J. Power Sources **163** (2006) 9-17.

[11] N. H. Jalani, M. Ramani, K. Ohlsson, S. Buelte, G. Pacifico, R. Pollard, R. Satudt, R. Datta, J. Power Sources **160** (2006) 1096-1103.

[12] J. Lobato, P. Canizares, M. A. Rodrigo, J.J. Linares, J. A. Aguilar, J. Membr. Sci. **306** (2007) 47-55.

[13] J. Lobato, P. Canizares, M. A. Rodrigo, J.J. Linares, G. Manjavcas, J. Membr. Sci. **280** (2006) 351-362.

[14] J. Lobato, P. Canizares, M. A. Rodrigo, D. Ubeda, F. J. Pinar, J. Membr. Sci. **369** (2011) 105-111.

[15] F. J. Pinar, P. Cañizares, M. A. Rodrigo, D. Ubeda, J. Lobato, RSC Adv. **2** (2012) 1547-1556.

[16] H. Pu, L. Liu, Z.Chang, J. Yuan, Electochim. Acta **54** (2009) 7536-7541.

[17] Y. Devrim, H. Dervim, I. Erouglu, Int. J. Hydrogen Energ. **4**1 (2016) 10044-10052.

[18] C. Xu, X. Wu, X. Wang, M. Mamlouk, K. Scott, J. Mater. Chem. **21** (2011) 6014-6019.

[19] Q. Li, R. He, J. O. Jensen, N. J. Bjerrum, Fuel Cells **4** (2014) 147-159.

[20] S. Martin, Q. Li, T. Steenberg, J. O. Jensen, J. Power Sources **272** (2014) 559-566.

[21] H. Namzi, H. Ahmadi, J. Power Sources **19**6 (2011) 2573-2583.

[22] E.I. Santiago, R.A. Isidoro, M.A. Dresch, B.R. Matos, M. Linardi, F.C. Fonseca, Electrochim. Acta **54** (2009) 4111-4117.

[23] N. Abdullah, S. K. Kamarudin, J. Power Sources **278** (2015) 109-118.

CHAPTER 7

GENERAL CONCLUSION

This research work is to characterize not only the chemical and structural properties of synthesized inorganic composite materials but also physicochemical and electrochemical studies of pristine electrolyte membrane and inorganic composite doped-electrolyte membrane for the application of medium temperature fuel cells. According to mechanochemical dry milling, wet milling and liquid-phase shaking, high proton conductive composite materials were successfully fabricated and studied their structures and superprotonic conduction mechanism. Then, these composite materials were further applied as inorganic fillers in the fabrication of inorganic composite doped-polymer electrolyte membranes to enhance physicochemical and electrochemical performance. Furthermore, high proton conductive inorganic composites CHS-WSiA system and CHS-WPA system were studied via mechanochemical dry milling, wet milling, and liquid-phase shaking. Especially, mechanochemical wet milling and liquid-phase shaking using DMAc solvent promoted to achieve new composites with enhanced proton conductivities. The critical point of these kinds of composites with high proton conductivities is to apply as potential inorganic filler in the fabrication of inorganic-organic electrolyte membrane and application of medium temperature fuel cells system.

The general conclusions of this thesis are as follows:

1. High proton conductive inorganic composites materials were successfully synthesized via the mechanochemical dry milling, wet milling, and liquid-phase shaking, respectively. Inorganic solid acids CHS, WSiA, and WPA were used as precursor materials to form highly proton conductive inorganic composite materials. New hydrogen bond formation between CHS and WSiA/WPA via mechanochemical and liquid-phase shaking was the important factor to enhance anhydrous proton conductivity of these composites that

compared with precursor CHS and WSiA/WPA. According to solid state ^{1}H-MAS-NMR results, their hydrogen bonding distance was correlated with the anhydrous proton conductivity that the reduction of hydrogen bonding distance in the CHS-WSiA and CHS-WPA composite materials was supported to increase proton conductivity. High anhydrous proton conductivity was observed by inducing proton conduction path in their composite system. Among mechanochemical dry milling, wet milling, and liquid-phase shaking, the important of proton conduction path was clearly observed in their composite systems comparing from the precursor materials and composite using dry milling. From these observed results, the mechanochemical wet milling and liquid-phase shaking methods using DMAc solvent are the promising methods to improve the proton conductivity of inorganic solid composite fabrication. These new observed composite materials showed highly advantage additive fillers on the electrochemical applications and polymer electrolyte fuel cells evaluation.

2. The effect of mixed alkali metals inorganic solid acids of KHS and CHS on the anhydrous proton conductivity in the form of a composite material with WPA was evidently observed by a mechanochemical milling method. These investigations were done with reference to the pristine precursor materials and the single metals MHS-WPA composites. Temperature-dependent anhydrous proton conductivities of these composite materials, in a reducing temperature regime (160 to 40 °C) showed that the mechanochemical milling induced a chemical change in the composite materials to irreversible superprotonic phases, with the mixed alkali metals composite exhibiting the highest conductivities from 4.9×10^{-2} to 1.4×10^{-3} S cm^{-1} of a temperature range of 160 to 40 °C. The results showed the enhanced conductivities in the composites resulted from the formation of a superprotonic nano-interface of a complex hydrogen bonding network between MHS and WPA, induced by the substitution reaction of the metal cations into the

Keggin structure ion. The high proton conductive inorganic composite materials obtained will serve as good material in the anhydrous proton conductor material application fields; with our interest in the application in organic-inorganic electrolyte fuel cell membranes.

3. Proton conductive CHS-WSiA and CHS-WPA composite materials were applied as inorganic fillers in the inorganic-organic composite electrolytes to improve physicochemical and electrochemical properties of hydrocarbon polymer electrolytes. In this case, high proton conductive CHS-WSiA and CHS-WPA composite materials fabricated via mechanochemical dry milling and wet milling was incorporated into polybenzimidazole (PBI) organic polymer. Finally, the obtained composite doped-PBI membranes showed the good flexibility, thermally, and chemically properties, and then their physicochemical and electrochemical performance were distinctly enhanced rather than pristine PBI after the inorganic composites into PBI matrix. The FC performance was remarkably improved for inorganic-organic composites electrolyte membranes during the single fuel cell testing in a wide temperature range under anhydrous condition. The synthesized CHS-WSiA and CHS-WPA composites doped-PBI membranes create new proton conduction sites in their polymer matrices, and show good hydrogen bonding correlation between the interfacial layer of CHS-WSiA/CHS-WPA and PBI polymer. Besides, the larger amount of CHS-WSiA and CHS-WPA doped into PBI matrix improves the fuel cell performances. From the results, these newly synthesized inorganic solid composite materials show as good promising additive fillers to improve the physicochemical and electrochemical properties of inorganic-organic composite electrolyte membranes.
4. Metal oxide (TiO_2) doped-PBI matix was a new achievement of cell performance to improve acid and water retention abilities during fuel evaluation. These results showed superior performance of TiO_2 doped-PBI membranes compared from pristine PBI with an

optimal TiO_2 composition of 2 wt % giving a power density of 434 mW cm^{-2}, compared to 195 mW cm^{-2} of the pure PBI membrane. These observed enhanced performance indicators in the TiO_2/PBI composite membranes were attributed to the enhancement effect, with some level of synergistic effect with PBI, of the TiO_2 component on PA adsorption and retention, and the capture of radical by-products from the fuel cell reactions that attack the PBI membrane. These results provide fundamental understanding and information of the enhancement effect of metal oxide TiO_2 on the cell performance of PBI based fuel cells and thus a good guide for fuel cell researchers and industry. These observations imply that metal oxide doped-PBI electrolyte membrane is a promising way to improve the proton conductivity and cell performance durability in the medium temperature fuel cell evaluation.

5. The observed good performance and possible proton conduction pathway in CHS-WSiA and CHS-WPA composite electrolytes have been completely discussed, and their advantages of inorganic-organic composite electrolytes were determined by approaching to desirable performances in single fuel cell systems. Based on all the studies in this thesis, it can be summarized that mechanochemical wet milling and liquid-phase shaking methods possessed excellent promising condition of improving the physicochemical and electrochemical performances of inorganic-organic polymer matrices.

ACKNOWLEDGEMENTS

Prior to taking this opportunity to thank, I would like to apologize for people, if there are missing a name of them from below. But anyway, I always sincerely appreciate your valuable help, and therefore I hope you will not take any offense at my mistakes. First and foremost, I would like to thank my supervisor, Professor Atsunori Matsuda, for taking a chance on my study at Department of Electrical and Electronic Information Engineering, Toyohashi University of Technology (TUT), Japan. I am eternally grateful to him for his patient and tireless support throughout the course of my thesis work, without his care and guidance I might never have discovered my interesting and passion for research. I truly respect him as a mentor, advisor, teacher, scientist and father, who excels at all. Then I would like to acknowledge my advisor Professor Hiroyuki Muto, Associate Professor Go Kawamura, and Assistant Professor Wai Kian Tan. They become wonderful mentors for my works and studies. I sincerely appreciate the very valuable advice and guidance, which have been a great help in my research and this thesis. I sincerely appreciate the very valuable advice and guidance, which have been a great help in my research and this thesis, from Professor Takanori Mizushima and Associate Professor Toshiaki Hattori.

I am grateful to people-concerned about ASEAN University Network/Southeast Asia Engineering Education Development Network (Japan International Cooperation Agency) scholarship and the Japan Society for the Promotion of Science (JSPS) Grants-in-Aid for Scientific Research A (26249097 and 18H03841) for financial support and the opportunity to undertake this work.

I also thank Dr. Pascal, Dr. Wei, Mr. Maegawa, Mr. Ooi, Mr. Matsubara, Mr. Ashida and all members of Matsuda-Muto-Kawamura-Tan laboratory for their immense support and

making my studies fruitful. Without their technical support and guidance, I could not have possibly finished my study here easily.

I have to thank my parents, and their eternal companion, for their unconditional and constant love, support and encouragement. Finally, my sincere thanks must go to my family members, especially parents for their endless love and care during my entire life.

Kyaw Zay Ya

Department of Electrical and Electronic Information Engineering

Toyohashi University of Technology

Toyohashi, Japan

July 2019

LIST OF PUBLICATIONS

Original manuscript on the topic of this thesis:

1. **Kyaw Zay Ya**, Go Kawamura, Hiroyuki Muto, and Atsunori Matsuda, "Anhydrous proton conduction of $0.6CsHSO_4$-$0.4H_4SiW_{12}O_{40}$ (CHS-WSiA) composite materials fabricated by dry and wet mechanochemical ball milling," Materials Today: Proceedings, **16** (2019) 220-225.

(Chapter 2)

2. **Kyaw Zay Ya**, Pascal Nbelayim, Go Kawamura, Hiroyuki Muto, Atsunori Matsuda, "Anhydrous proton conductive xCHS-(1-x)WSiA composites prepared via liquid-phase shaking", Solid State Ionics, **337** (2019) 1-6.

(Chapter 2)

3. **Kyaw Zay Ya**, Pascal Nbelayim, Takuya Kikuchi, Keichiro Maegawa, Go Kawamura, Hiroyuki Muto, Atsunori Matsuda, "Mechanochemical milling preparation and characterization of mixed alkali metal ions of K-/Cs-hydrogen sulfate-phosphotungstic acid composite as inorganic solid proton conductors," Solid State Ionics, **340** (2019) 115022.

(Chapter 3)

4. **Kyaw Zay Ya**, Pascal Nbelayim, Wai Kian Tan, Go Kawamura, Hiroyuki Muto, and Atsunori Matsuda, "Effects of cesium-substituted silicotungstic acid doped with polybenzimidazole membrane for the application of medium temperature polymer

electrolyte fuel cells," E3S Web of Conferences, **83** (2019) 01008.

(Chapter 4)

5. **Kyaw Zay Ya**, Keisuke Kumazawa, Go Kawamura, Hiroyuki Muto, and Atsunori Matsuda, "Cell performance enhancement with titania-doped polybenzimidazole based composite membrane in intermediate temperature fuel cell under anhydrous condition," Journal of the Ceramic Society of Japan, **126** (2018) 789-793.

(Chapter 6)

6. Rajesh Kumar, Mohamed M. Abdel-Galeil, **Kyaw Zay Ya**, Kosuke Fujita, Wai Kian Tan, Atsunori Matsuda, "Facile and fast microwave-assisted formation of reduced graphene oxide-wrapped manganese cobaltite ternary hybrids as improved supercapacitor electrode material," Applied Surface Science, **481** (2019) 296-306.

7. Keiichiro Maegawa, **Kyaw Zay Ya**, Wai Kian Tan, Go Kawamura, Toshiaki Hattori, Hiroyuki Muto, Atsunori Matsuda, "Enhancement of interfacial property by novel solid ionomer $CsHSO_4$-$H_4SiW_{12}O_{40}$ for the three-phase interface of a medium-temperature anhydrous fuel cell," Materials Letters, **253** (2019) 201-204.

I have gained agreements with all of coauthors about using the above thesis to apply for Academic Degree.

Kyaw Zay Ya